
Supplementary information

Flatband λ - Ti_3O_5 towards extraordinary solar steam generation

In the format provided by the
authors and unedited

Flatband λ -Ti₃O₅ towards extraordinary solar steam generation

Supplementary Information

Bo Yang¹, Zhiming Zhang¹, Peitao Liu², Xiankai Fu¹, Jiantao Wang², Yu Cao², Ruolan Tang¹, Xiran Du¹, Wanqi Chen¹, Song Li¹, Haile Yan¹, Zongbin Li¹, Xiang Zhao¹, Gaowu Qin¹, Xing-Qiu Chen², Liang Zuo^{1,*}

¹ *Key Laboratory for Anisotropy and Texture of Materials (Ministry of Education), School of Materials Science and Engineering, Northeastern University, Shenyang 110819, China*

² *Shenyang National Laboratory for Materials Science, Institute of Metal Research, Chinese Academy of Sciences, Shenyang 110016, China*

Contents

Section 1. Structural features and optical properties of titanium suboxides (TSOs)	1
S1.1. Structural characterizations of TSOs.....	1
S1.2. Morphological characterization and hydrophilic feature of λ - Ti_3O_5 powders	2
S1.3. Structural optimization and calculated electronic densities of states of TSOs	3
S1.4. First-principles calculations of optical properties of TSOs	5
S1.5. Ti-Ti dimer introduced relatively flat bands in β - Ti_3O_5 and Ti_4O_7	7
S1.6. Contribution of flat bands to solar absorptivity	9
S1.7. Optical transitions in λ - Ti_3O_5	9
Section 2. Photothermal conversion performances of TSOs.....	13
S2.1. Experimental setup of photothermal conversion measurements	13
S2.2. Estimation of solar-to-heat efficiency with thermometric method	13
S2.3. Measured surface temperatures and calculated solar-to-heat efficiencies of TSOs.....	14
S2.4. Measured photoluminescence spectra of λ - Ti_3O_5 powders	16
S2.5 Photothermal conversion mechanism for λ - Ti_3O_5	17
Section 3. Solar evaporation performance and water vaporization enthalpy of two-dimensional (2D) evaporator system.....	20
S3.1. Experimental setup of 2D solar steam evaporator system.....	20
S3.2. Measured water evaporation rates of 2D-SSEs using different TSOs.....	20
S3.3. Estimation of water vaporization enthalpy and solar-to-steam efficiency with thermometric method	21
S3.4. Calculated water vaporization enthalpy and solar-to-steam efficiency for 2D λ - Ti_3O_5 evaporator	22
S3.5. Experimental vaporization enthalpy of water on the surfaces of λ - Ti_3O_5 powders	23
Section 4. Theoretical calculations of water adsorption and dissociation on λ-Ti_3O_5 surface.....	25
S4.1. First-principles calculations of surface energies of λ - Ti_3O_5	25
S4.2. First-principles calculations of preference sites for water adsorption on λ - Ti_3O_5 ($\bar{1}\bar{1}0$) surface	26
S4.3. Signals of Ti-O-H bending and stretching on λ - Ti_3O_5 surface	29
S4.4. AIMD simulations of water molecule distributions on λ - Ti_3O_5 ($\bar{1}\bar{1}0$) surface.....	32
S4.5. Transfer of H atom and formation of H_3O^* unit on λ - Ti_3O_5 ($\bar{1}\bar{1}0$) surface	34
S4.6. Calculated hydrogen bond lengths and binding energies for different water molecules clusters	38
S4.7. Evidence on the λ - Ti_3O_5 assisted water evaporation in the form of small clusters	39
Section 5. Performances of three-dimensional (3D) evaporator system	41
S5.1. Experimental setup of 3D solar steam evaporator system.....	41
S5.2. Optimizations of cylinder-shaped 3D-SSEs.....	41
S5.3. Estimation of solar-to-steam efficiency for 3D-SSE with a conical cavity	44
S5.4. Thermal stability and mechanical properties of 3D-SSEs with a conical cavity	47
S5.5. Indoor and outdoor clean water collections with 3D-SSEs	48
Section 6. Comparisons of 2D- and 3D-SSEs with known ones.....	52
References	55

Section 1. Structural features and optical properties of titanium suboxides (TSOs)

S1.1. Structural characterizations of TSOs

The raw materials used in this study, including titanium monoxide-TiO powders (100 mesh, 99.9% metals basis), rutile-TiO₂ nanoparticles (25 nm in diameter) and titanium (III) oxide-Ti₂O₃ powders (100 mesh, 99.9% metals basis), were purchased from Aladdin Chemistry Co. Ltd., China. Both the λ -Ti₃O₅ and Ti₄O₇ powders were synthesized in the laboratory by reduction of the rutile-TiO₂ nanoparticles at 1200 °C under a hydrogen atmosphere, whereas the β -Ti₃O₅ powders were prepared from the synthesized λ -Ti₃O₅ powders by applying a stress of 1500 MPa.

The crystal structures of all the considered TSOs were examined at room temperature by X-ray diffraction (XRD) with a Rigaku X-ray diffractometer using Cu- $K\alpha$ radiation (1.54056 Å in wavelength). These include both the commercial TiO and C-Ti₂O₃ powders and the as-prepared λ -Ti₃O₅, β -Ti₃O₅ and Ti₄O₇ powders. For the as-prepared TSO powders, we performed the full-profile Rietveld refinements on the recorded XRD patterns using the FULLPROF package¹. Results show that the as-prepared λ -Ti₃O₅ powder sample contains only a single λ -Ti₃O₅ phase (Fig. S1.1a), as compared to the reported one with 80.00 vol.% λ -Ti₃O₅ and 20.00 vol.% β -Ti₃O₅². The as-prepared β -Ti₃O₅ powder sample consists of 96.81 vol.% β -Ti₃O₅ and 3.19 vol.% λ -Ti₃O₅ (Fig. S1.1b). The as-prepared Ti₄O₇ powder sample consists of 99.23 vol.% Ti₄O₇ and 0.77 vol.% β -Ti₃O₅ (Fig. S1.1c). Table S1.1 presents the refined lattice constants and internal atomic parameters of the λ -Ti₃O₅, β -Ti₃O₅ and Ti₄O₇ phases. Note that our Rietveld refinement results are in nice agreement with the published data for the λ - and β -Ti₃O₅ phases² and the Ti₄O₇ phase³.

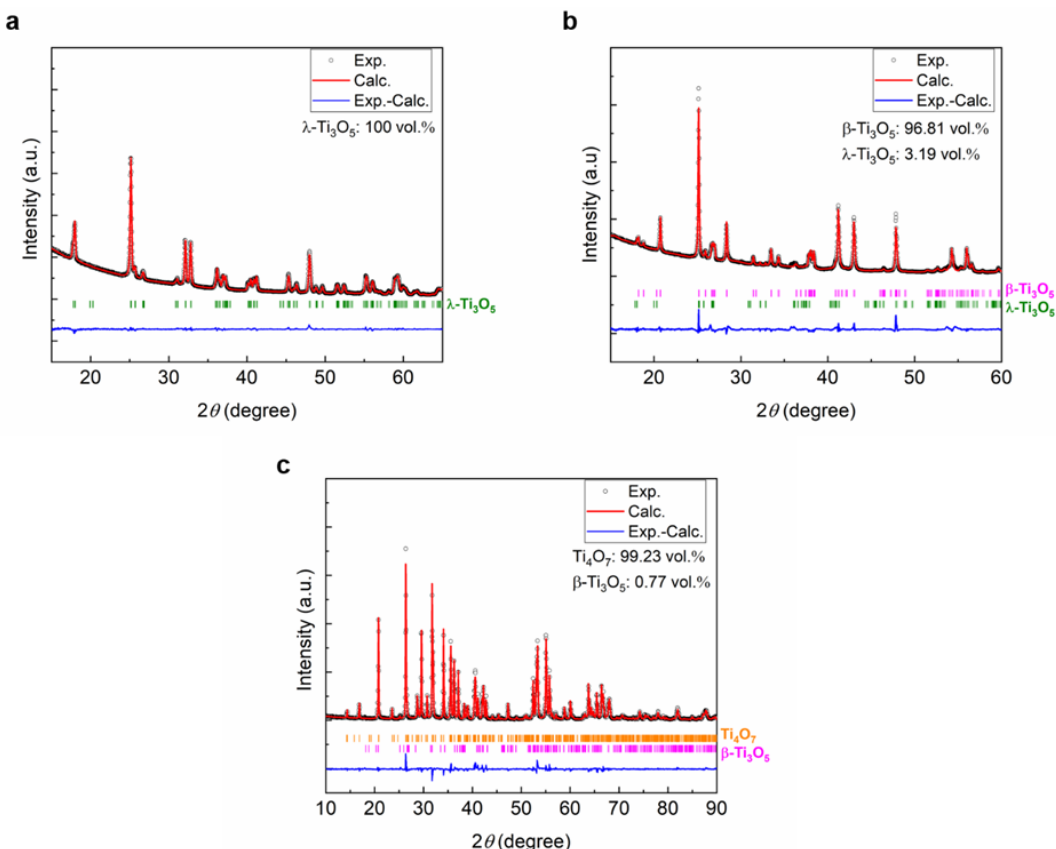


Figure S1.1, Rietveld refinements of the experimental XRD data. The vertical bars indicate the calculated 2θ-positions of the Bragg reflections. **a**, λ -Ti₃O₅. **b**, β -Ti₃O₅. **c**, Ti₄O₇.

Table S1.1. Experimental crystal structural parameters of the λ - Ti_3O_5 , β - Ti_3O_5 and Ti_4O_7 phases, refined with the FULLPROF package. For comparison, the published data in Ref. 2 and Ref. 3 are also compiled.

a Lattice parameters			Wyckoff positions					
Polymorph	This work λ - Ti_3O_5	Nat. Commun. 6, 7037 (2015) λ - Ti_3O_5	This work			Nat. Commun. 6, 7037 (2015)		
	x/a	y/b	z/c	x/a	y/b	z/c		
Crystal system	Monoclinic	Monoclinic	Ti(1)	0.6288(2)	0	0.0523(2)	0.6292(2)	0
Space group	C2/m (No.12)	C2/m (No.12)	Ti(2)	0.30773(17)	0	0.2455(2)	0.30586(14)	0
a (Å)	9.85575(51)	9.83119(19)	Ti(3)	0.6326(2)	0	0.4349(2)	0.6330(2)	0
b (Å)	3.79130(19)	3.78798(7)	O(1)	0.4546(7)	0	0.3842(6)	0.4561(6)	0
c (Å)	9.98731(50)	9.97039(19)	O(2)	0.1782(6)	0	0.0629(6)	0.1778(5)	0
β ($^\circ$)	91.2503(14)	91.2909(7)	O(3)	0.7417(6)	0	0.2509(6)	0.7321(5)	0
V(Å 3)	373.099(33)	371.207(20)	O(4)	0.5464 (7)	0	0.8708(6)	0.5421(5)	0
Z	4	4	O(5)	0.1900(1)	0	0.4284(6)	0.1908(5)	0

b Lattice parameters			Wyckoff positions					
Polymorph	This work β - Ti_3O_5	Nat. Commun. 6, 7037 (2015) β - Ti_3O_5	This work			Nat. Commun. 6, 7037 (2015)		
	x/a	y/b	z/c	x/a	y/b	z/c		
Crystal system	Monoclinic	Monoclinic	Ti(1)	0.1275(5)	0	0.0419(6)	0.1272(2)	0
Space group	C2/m (No.12)	C2/m (No.12)	Ti(2)	0.7803(4)	0	0.2680(4)	0.7795(2)	0
a (Å)	9.75304(62)	9.75252(18)	Ti(3)	0.0514(6)	0	0.3663(5)	0.0545(2)	0
b (Å)	3.79999(22)	3.80034(6)	O(1)	0.6773(22)	0	0.0586(22)	0.6717(8)	0
c (Å)	9.44369(58)	9.44413(19)	O(2)	0.2328(22)	0	0.2406(20)	0.2352(7)	0
β ($^\circ$)	91.5411(21)	91.5322(10)	O(3)	0.5972(15)	0	0.3446(18)	0.5930(6)	0
V(Å 3)	349.870(37)	349.902(11)	O(4)	0.9461(18)	0	0.1541 (21)	0.9516(7)	0
Z	4	4	O(5)	0.8573 (20)	0	0.4485 (21)	0.8726(6)	0

c Lattice parameters			Wyckoff positions					
Polymorph	This work Ti_4O_7	J. Solid State Chem. 29, 47 (1979) Ti_4O_7	This work			J. Solid State Chem. 29, 47 (1979)		
	x/a	y/b	z/c	x/a	y/b	z/c		
Crystal system	Monoclinic	Monoclinic	Ti(1)	0.221 (1)	0.153(1)	0.062 (1)	0.216	0.153
Space group	A $\bar{1}$ (No.2)	A $\bar{1}$ (No.2)	Ti(2)	0.216 (1)	0.652 (1)	0.067(1)	0.218	0.653
a (Å)	5.5957(2)	5.5942(6)	Ti(3)	0.679(1)	0.438 (1)	0.200	0.683	0.440
b (Å)	7.1252(2)	7.1216(8)	Ti(4)	0.692 (1)	0.944 (1)	0.203	0.688	0.924
c (Å)	12.4616(4)	12.4600(1)	O(1)	0.103 (3)	0.859 (2)	0.013(1)	0.108	0.863
α ($^\circ$)	95.05	95.05(1)	O(2)	0.589 (3)	0.787 (3)	0.055(1)	0.587	0.793
β ($^\circ$)	95.17	95.19(1)	O(3)	0.852 (3)	0.490(2)	0.081 (1)	0.856	0.496
V(Å 3)	464.91(3)	464.48	O(4)	0.318 (3)	0.425 (2)	0.133 (1)	0.328	0.438
Z	4	4	O(5)	0.519(3)	0.142 (2)	0.163 (1)	0.526	0.145
			O(6)	0.028 (3)	0.068(2)	0.198 (1)	0.038	0.071
			O(7)	0.294 (2)	0.784(2)	0.221(1)	0.295	0.224

S1.2. Morphological characterization and hydrophilic feature of λ - Ti_3O_5 powders

The morphology of the as-prepared λ - Ti_3O_5 powders was examined with a field-emission scanning electron microscope (SEM), showing a mean particle size of $\sim 1 \mu\text{m}$ (Fig. S1.2a). Further analyses by transmission electron microscope (TEM, Figs. S1.2b and S1.2c) and Raman spectrometer (Fig. S1.2d) confirmed that the powders are composed of the λ - Ti_3O_5 phase. According to the contact angle test (Fig. S1.2e), the as-prepared λ - Ti_3O_5 powders have a hydrophilic nature.

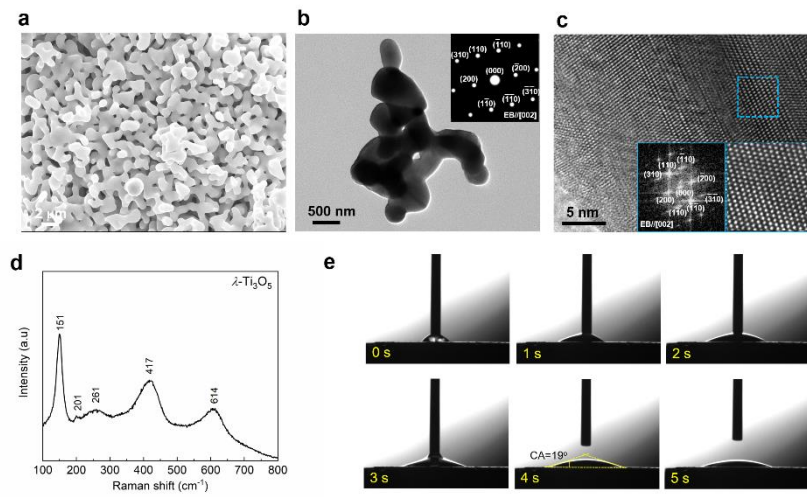


Figure S1.2. **a-d**, SEM image, TEM bright-field image, high-resolution TEM image and Raman spectrum of λ - Ti_3O_5 powders. The inset in **c** is the Fast-Fourier transformation (FFT) of the dotted blue area. **e**, Contact angle test of the as-prepared λ - Ti_3O_5 powders.

S1.3. Structural optimization and calculated electronic densities of states of TSOs

Our first-principles calculations were performed based on density functional theory (DFT) using the improved Perdew-Burke-Ernzerhof version designed specifically for solids (PBEsol)⁴. To properly account for the strong Coulomb interaction on the Ti-3d orbitals of all the considered TSOs, the effective onsite Hubbard U correction was made with the Dudarev formulation⁵. We adopted a U value of 2.5 eV for C-Ti₂O₃ and 4.3 eV for the others (*see* Table S1.2). These U values were chosen to match the experimental bandgaps of β -Ti₃O₅ and C-Ti₂O₃ semiconductors^{6,7}. A plane wave cutoff of 520 eV and a Γ -centered k -point grid with a spacing of 0.2 Å⁻¹ between k points were employed.

Table S1.2 presents the optimized structural parameters for both the commercial TiO and C-Ti₂O₃ powders and the as-prepared λ -Ti₃O₅, β -Ti₃O₅ and Ti₄O₇ powders. The calculated electronic densities of states (DOSs) of these TSOs are shown in Fig. S1.3. It can be seen from Fig. S1.3 that the TiO, λ -Ti₃O₅ and Ti₄O₇ compounds exhibit metallic properties, whereas the C-Ti₂O₃ and β -Ti₃O₅ compounds possess semiconducting properties with a respective bandgap of about 0.10 eV and 0.14 eV, in coincidence with the available experimental values^{6,7}.

Table S1.2, Parameters for density functional calculations and optimized lattice constants of TSOs.

TSOs	Space group	Lattice parameters	Metallic/Semiconducting	Magnetic state	U (eV)
TiO	$C2/m$ No. 12	$a=9.34$ Å $\alpha=90^\circ$			
		$b=4.14$ Å $\beta=107.5^\circ$	Metallic	Nonmagnetic	4.3
		$c=5.89$ Å $\gamma=90^\circ$			
C-Ti ₂ O ₃	$R\bar{3}C$ No. 167	$a=5.15$ Å $\alpha=90^\circ$			
		$b=5.15$ Å $\beta=90^\circ$	Semiconducting	Antiferromagnetic	2.5
		$c=13.61$ Å $\gamma=120^\circ$			
λ -Ti ₃ O ₅	$C2/m$ No. 12	$a=9.83$ Å $\alpha=90^\circ$			
		$b=3.79$ Å $\beta=91.29^\circ$	Metallic	Nonmagnetic	4.3
		$c=9.97$ Å $\gamma=90^\circ$			
β -Ti ₃ O ₅	$C2/m$ No. 12	$a=9.75$ Å $\alpha=90^\circ$			
		$b=3.79$ Å $\beta=91.53^\circ$	Semiconducting	Nonmagnetic	4.3
		$c=9.44$ Å $\gamma=90^\circ$			
Ti ₄ O ₇	$A\bar{1}$ No. 2	$a=5.59$ Å $\alpha=64.09^\circ$			
		$b=6.91$ Å $\beta=70.98^\circ$	Metallic	Nonmagnetic	4.3
		$c=7.13$ Å $\gamma=75.32^\circ$			

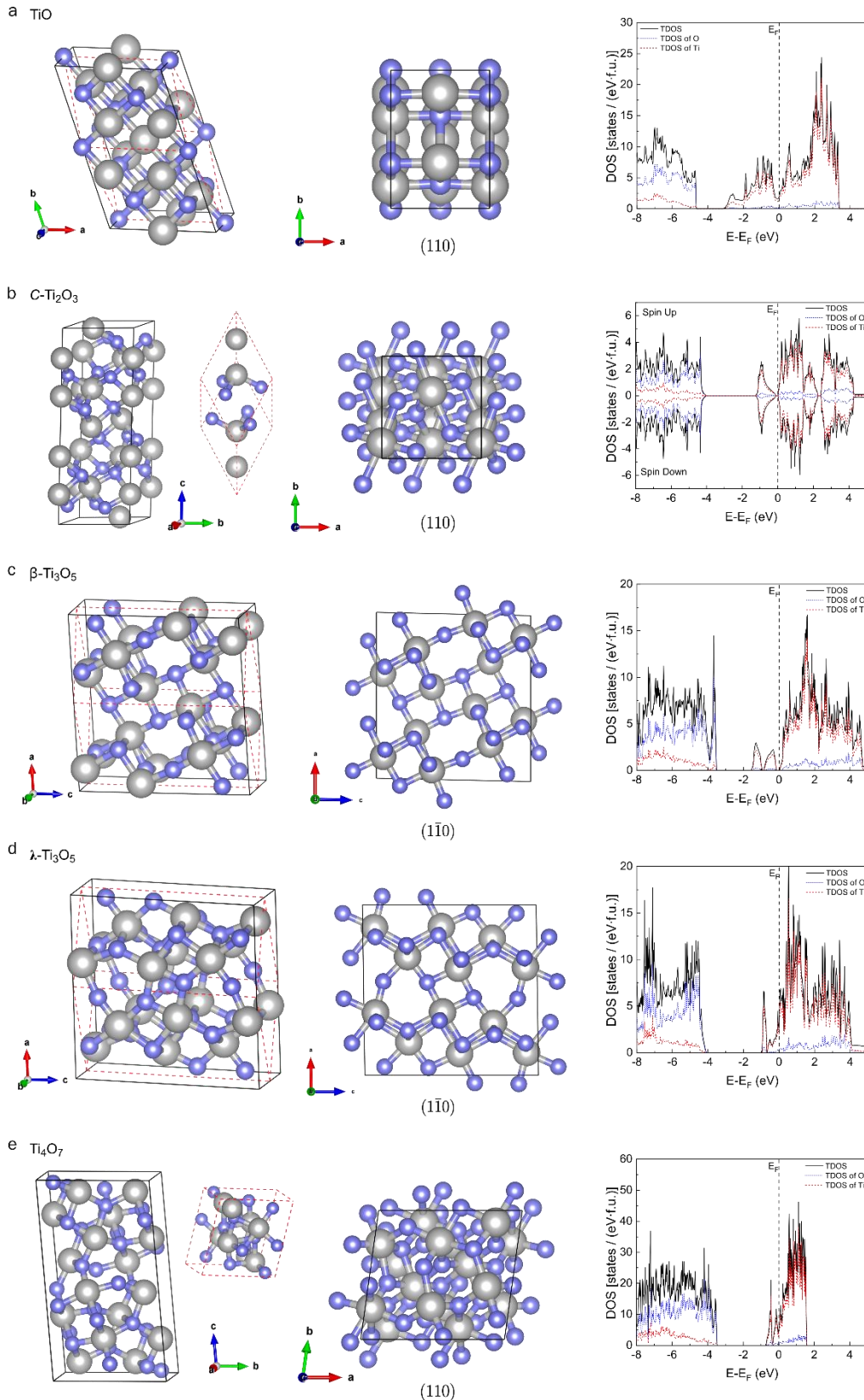


Figure S1.3. Optimized crystal structures (first column), specific crystallographic planes (second column) and calculated DOSs (third column) of TSOs. For each TSO, the unit cell is outlined by red dotted lines in the first column. **a**, TiO. **b**, C-Ti₂O₃. **c**, β-Ti₃O₅. **d**, λ-Ti₃O₅. **e**, Ti₄O₇.

S1.4. First-principles calculations of optical properties of TSOs

To calculate the optical properties of TSOs, we start with the frequency-dependent dielectric function $\varepsilon(\omega)$ ⁸,

$$\varepsilon(\omega) = \varepsilon_1(\omega) + i \varepsilon_2(\omega), \quad (1)$$

where $\varepsilon_1(\omega)$ and $\varepsilon_2(\omega)$ are the real and imaginary parts of $\varepsilon(\omega)$, respectively, and ω is the photon frequency.

For a semiconductor, if only the contribution of interband optical transitions to $\varepsilon(\omega)$ is considered, $\varepsilon_2(\omega)$ takes the form

$$\varepsilon_2(\omega) = \frac{2e^2\pi}{\Omega\varepsilon_0} \sum_{k,c,v} \langle \Psi_k^c | \mathbf{u} \cdot \mathbf{r} | \Psi_k^v \rangle^2 \delta(E_k^c - E_k^v - \hbar\omega), \quad (2)$$

where e is the electron charge, ε_0 is the permittivity of vacuum, Ω is the volume of the reciprocal unit cell, c and v denote respectively the conduction and valence bands, \mathbf{u} is the polarization of the incident light, \mathbf{r} is the position operator, and Ψ_k^c (Ψ_k^v) is the wave function of the conduction (valence) bands at the lattice momentum \mathbf{k} . The joint density of electronic states, defined as the number of states per unit volume per unit energy range, is directly related to the $\delta(E_k^c - E_k^v - \hbar\omega)$ function. With the Kramer-Kronig relation, $\varepsilon_1(\omega)$ can be derived from $\varepsilon_2(\omega)$ by

$$\varepsilon_1(\omega) = 1 + \frac{2}{\pi} P \int_0^\infty \frac{\omega' \varepsilon_2(\omega')}{\omega'^2 - \omega^2} d\omega', \quad (3)$$

where P in the front of the integral means the principal value.

The above expression for $\varepsilon_2(\omega)$ is given within the independent-particle approximation. To include the effects of electron-hole interactions, we solved the Bethe-Salpeter equation using a static model dielectric function⁹,

$$\varepsilon_{\mathbf{q},\mathbf{G}}^{-1}(\mathbf{q}) = \varepsilon_\infty^{-1} + (1 - \varepsilon_\infty^{-1})[1 - \exp(-\frac{|\mathbf{q}+\mathbf{G}|^2}{4\lambda_{\text{screen}}^2})], \quad (4)$$

where ε_∞ is the static ion-clamped dielectric function in the long-wave limit, \mathbf{q} and \mathbf{G} are respectively the wave vector and lattice vector of the reciprocal cell, and λ_{screen} is the screening length parameter derived by fitting ε^{-1} at small wave vectors with respect to $|\mathbf{q} + \mathbf{G}|$. This approach, named the model-BSE (mBSE)⁵, allows for a more accurate calculation of the dielectric functions with a denser k -point mesh.

As for a metal, one should also consider the contribution of intraband optical transitions to the dielectric function. Here, we refer to the empirical Drude model as follows^{8,10,11},

$$\begin{aligned} \varepsilon_1^{\text{intra}} &= 1 - \frac{\omega_p^2}{\omega^2 + \Gamma^2}, \\ \varepsilon_2^{\text{intra}} &= \frac{\Gamma \omega_p^2}{\omega (\omega^2 + \Gamma^2)}, \end{aligned} \quad (5)$$

where ω_p is the plasma frequency tensor, which can be obtained by first-principles calculations. The parameter Γ is defined as $\Gamma = \hbar/\tau$ (τ denotes the mean free time between electron collisions; typically, it is estimated to be in the magnitude of 10^{-14} s in metals)⁸. Considering that the metallic TSOs are less electrically conductive than pure metals, *e.g.*, ~ 30 S cm⁻¹ for $\lambda\text{-Ti}_3\text{O}_5$ nano-crystals⁷, it is pertinent to suggest a smaller value on τ . In this work, Γ was set to 1.5 eV (*i.e.*, $\tau = 2.76 \times 10^{-15}$ s).

Furthermore, we consider a polycrystalline material with finite thickness d . Its mean dielectric function can be calculated by averaging those of single crystals with the orientation distribution function as the weight¹². The upper and lower bounds of the mean dielectric constant $\varepsilon_{\text{poly}}$ are often approximated by^{13,14}

$$\frac{3}{\lambda_1 + \lambda_2 + \lambda_3} < \varepsilon_{\text{poly}} < \frac{\lambda_1 + \lambda_2 + \lambda_3}{3}, \quad (6)$$

where λ_1 , λ_2 and λ_3 are the eigenvalues of the single crystal dielectric tensor. Here, we estimated $\varepsilon_{\text{poly}}$ using the simple average in the form of $\varepsilon_{\text{poly}} = (\lambda_1 + \lambda_2 + \lambda_3)/3$. The frequency-dependent optical properties, e.g., refractive index $n(\omega)$, extinction coefficient $k(\omega)$, absorption coefficient $\alpha(\omega)$, reflectivity $R(\omega)$ and absorptivity $A(\omega)$, can then be derived from $\varepsilon_{1,\text{poly}}(\omega)$ and $\varepsilon_{2,\text{poly}}(\omega)$ as follows¹⁵,

$$n(\omega) = \frac{1}{\sqrt{2}} \left[\sqrt{[\varepsilon_{1,\text{poly}}(\omega)]^2 + [\varepsilon_{2,\text{poly}}(\omega)]^2} + \varepsilon_{1,\text{poly}}(\omega) \right]^{\frac{1}{2}}, \quad (7)$$

$$k(\omega) = \frac{1}{\sqrt{2}} \left[\sqrt{[\varepsilon_{1,\text{poly}}(\omega)]^2 + [\varepsilon_{2,\text{poly}}(\omega)]^2} - \varepsilon_{1,\text{poly}}(\omega) \right]^{\frac{1}{2}}, \quad (8)$$

$$\alpha(\omega) = \frac{2\omega}{c} k(\omega), \quad (9)$$

$$R(\omega) = \frac{[n(\omega)-1]^2 + [k(\omega)]^2}{[n(\omega)+1]^2 + [k(\omega)]^2}, \quad (10)$$

$$A(\omega) = 1 - R(\omega) - [1 - R(\omega)]^2 \exp[-\alpha(\omega) d], \quad (11)$$

where c is the velocity of light. Furthermore, the average absorptivity \bar{A} over the full solar spectrum from 200 nm to 2500 nm (in wavelength) is calculated by^{16,17 18}

$$\bar{A} = \frac{\int_{200}^{2500} A(\omega) E_{\omega,\text{solar}}(\omega) d\omega}{\int_{200}^{2500} E_{\omega,\text{solar}}(\omega) d\omega}, \quad (12)$$

where $E_{\omega,\text{solar}}$ is the AM1.5G spectrum from the sun¹⁸.

Based on the above methodology, the optical spectra of five TSOs were predicted *via* first-principles calculations, as displayed in Fig. S1.4. The absorption coefficients of metallic TiO, λ -Ti₃O₅ and Ti₄O₇ were calculated taking into account of the contributions of both interband and intraband optical transitions. The optical absorptivities of all the considered TSOs were calculated with an assumed sample thickness ($d = 4 \mu\text{m}$). In order to check the computational accuracies, we performed a test on C-Ti₂O₃. The predicted reflectivity spectrum agrees well with the measured one on a single crystal¹⁹, except for a 0.5 eV blue shift. In addition, the calculated absorption coefficients are consistent with those measured on a thin film²⁰. These results demonstrate the reliability of our computational methodology for optical properties. Note that the calculated solar absorption spectra are similar for both nonmagnetic and antiferromagnetic states of λ -Ti₃O₅. Hence, we adopted the results of the nonmagnetic state of λ -Ti₃O₅ in this work.

In comparison with the experimentally measured reflective spectra of TSOs (Fig. 1b in the main text), the calculated ones show some deviations, which might originate from two aspects. First, we employed an empirical Drude model to account for the contribution of intraband optical transitions for metallic TSOs. Second, we performed the reflectivity measurements on polycrystalline powder samples, whereas the theoretical reflectivities were calculated for single crystals without considering the size effects of TSO particles.

It is worth mentioning that λ -Ti₃O₅, β -Ti₃O₅ and Ti₄O₇ possess overall low optical reflectivities, whereas TiO and C-Ti₂O₃ have superior optical absorption coefficients (Fig. S1.4). Generally speaking, the factors of both optical absorption coefficient and optical reflectivity are equally important to improve the optical

absorptivity of a light-absorbing material with finite thickness. Although the optical absorption coefficients of $\lambda\text{-Ti}_3\text{O}_5$, $\beta\text{-Ti}_3\text{O}_5$ and Ti_4O_7 are lower than those of TiO and $\text{C-Ti}_2\text{O}_3$, they are still at a sufficiently high level (*i.e.*, 10^4 cm^{-1}) over the full solar spectrum region (Fig. S1.4c). In consequence, both $\lambda\text{-Ti}_3\text{O}_5$ and $\beta\text{-Ti}_3\text{O}_5$ exhibit relatively high optical absorptivities (mainly due to their ultralow optical reflectivities), as further verified by the diffuse reflectance measurements on the powder samples with a typical thickness of $\sim 100 \mu\text{m}$.

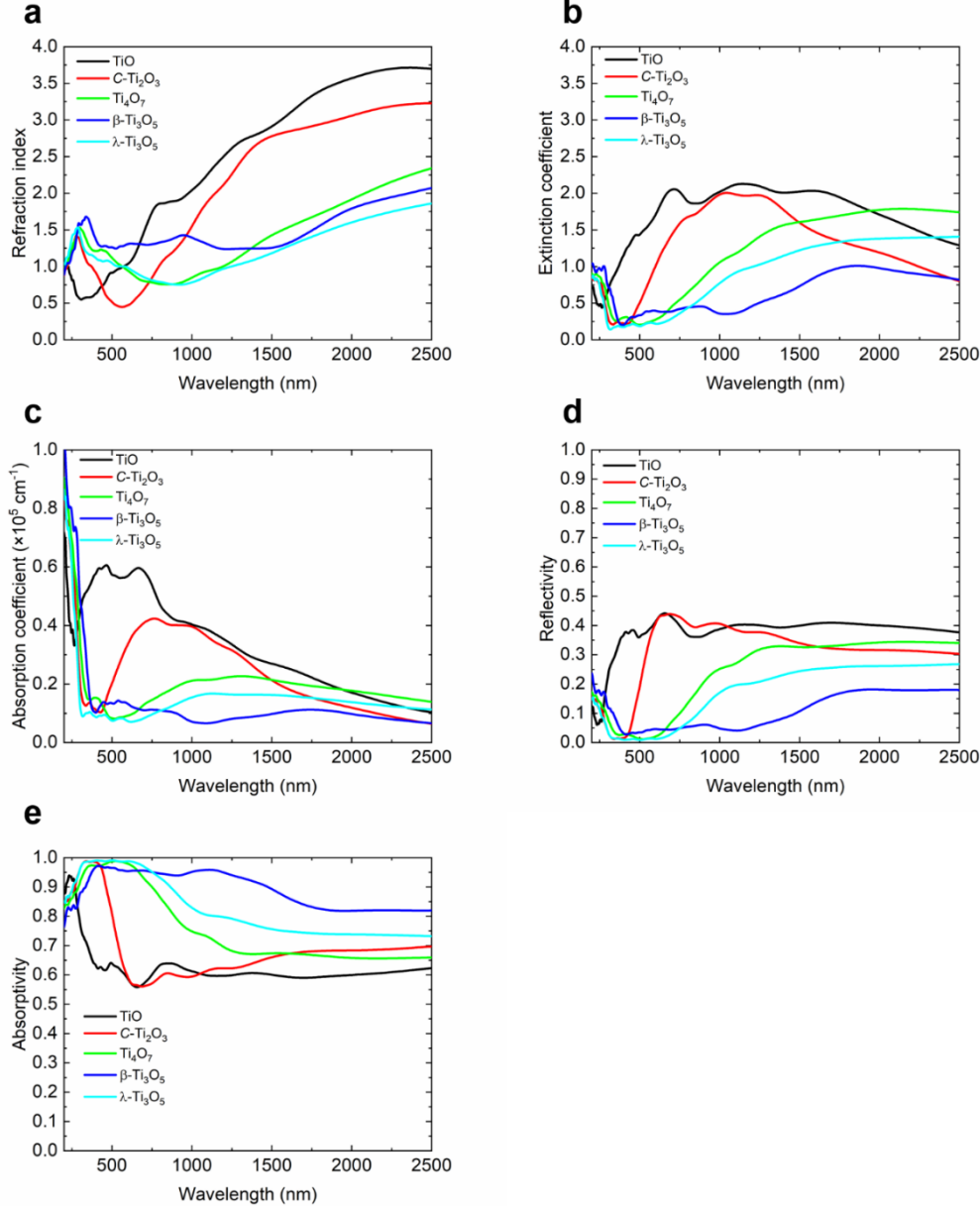


Figure S1.4. Calculated optical properties of TSOs in the wavelength range from 200 nm to 2500 nm. **a**, Refraction index $n(\omega)$. **b**, Extinction coefficient $k(\omega)$. **c**, Absorption coefficient $\alpha(\omega)$. **d**, Reflectivity $R(\omega)$. **e**, Absorptivity $A(\omega)$ ($d = 4 \mu\text{m}$).

S1.5. Ti-Ti dimer introduced relatively flat bands in $\beta\text{-Ti}_3\text{O}_5$ and Ti_4O_7

Among the considered five TSOs (except for TiO), they share a common structural feature of the so-called Ti-Ti dimers from two nearest-neighbor Ti atoms, as discussed in the main text. The existences of these Ti-Ti dimers create the crucial Ti 3d-like orbitals around the Fermi level. Following the discussion in

the main text on λ - Ti_3O_5 and C - Ti_2O_3 , we provide detailed information on the electronic structures of β - Ti_3O_5 and Ti_4O_7 in Figs. S1.5 and S1.6, respectively. For β - Ti_3O_5 , there exist two relatively flat bands (red and green solid lines) below the Fermi level, mostly contributed by the d_{xy} orbital hybridizations of the Ti_2 - Ti_2 , Ti_1 - Ti_3 and Ti_3 - Ti_3 dimers. As for Ti_4O_7 , there are also two relatively flat bands (red and green solid lines) below the Fermi level, mostly contributed by the d_{xy} orbital hybridizations of the Ti_1 - Ti_3 , Ti_3 - Ti_4 and Ti_4 - Ti_2 dimers.

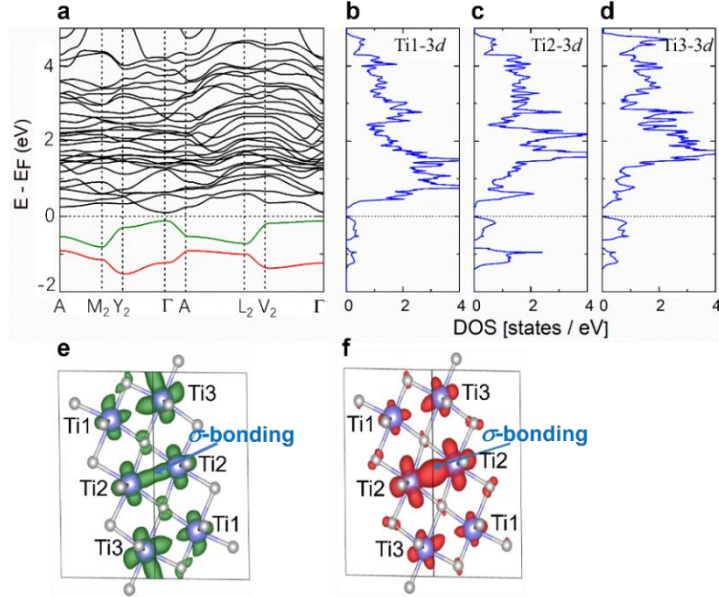


Figure S1.5. Electronic structure of β - Ti_3O_5 . **a**, Band structure. **b**, **c** and **d**, DOSs for Ti_1 - $3d$, Ti_2 - $3d$ and Ti_3 - $3d$ orbitals, respectively. **e** and **f**, Partial charge densities corresponding to the two relatively flat bands (green and red solid lines in **a**).

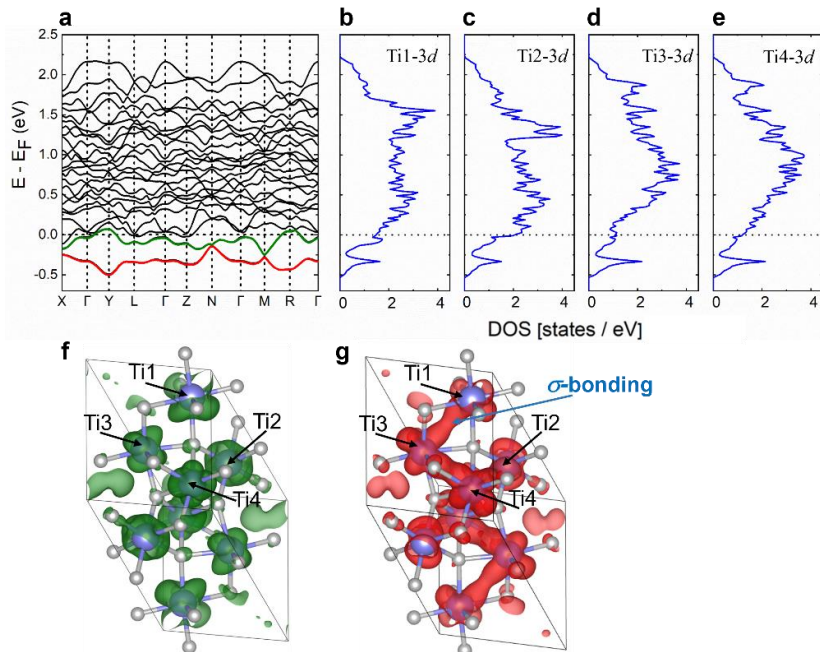


Figure S1.6. Electronic structure of Ti_4O_7 . **a**, Band structure. **b**, **c**, **d** and **e**, DOSs for Ti_1 - $3d$, Ti_2 - $3d$, Ti_3 - $3d$ and Ti_4 - $3d$ orbitals, respectively. **f** and **g**, Partial charge densities corresponding to the two relatively flat bands (green and red solid lines in **a**).

S1.6. Contribution of flat bands to solar absorptivity

To evaluate the contributions of the flat bands to the solar absorption, we have performed computational tests on the optical absorption coefficients of TSOs, using a procedure in analogy to that on the optical conductivity²¹. For the sake of brevity but without loss of generality, the computational tests were conducted with the independent-particle approximation and only the contribution of interband optical transitions to the dielectric function was taken into account. In principle, the imaginary part $\varepsilon_2(\omega)$ of the dielectric function can be divided into two terms $\varepsilon_2^{\text{flat}}(\omega)$ and $\varepsilon_2^{\text{non-flat}}(\omega)$ depicting the contributions from the low-lying flat valence bands and the other non-flat valence bands, respectively. When the refractive index $n(\omega)$ is fixed at given frequency ω , the contributions of the low-lying flat and non-flat valence bands to the extinction coefficient $k(\omega)$ take the explicit form: $\varepsilon_2^{\text{flat}}(\omega) = 2n(\omega) k^{\text{flat}}(\omega)$ and $\varepsilon_2^{\text{non-flat}}(\omega) = 2n(\omega) k^{\text{non-flat}}(\omega)$. With the relation $\alpha(\omega) = 2\omega k(\omega)/c$, one can calculate the corresponding absorption coefficients $\alpha^{\text{flat}}(\omega)$ and $\alpha^{\text{non-flat}}(\omega)$. Furthermore, the contributions of the low-lying flat and non-flat valence bands to the optical absorptivity $A(\omega)$ are approached by

$$A(\omega) = 1 - R(\omega) - [1 - R(\omega)]^2 \exp[-\alpha^{\text{flat}}(\omega) d] \exp[-\alpha^{\text{non-flat}}(\omega) d]. \quad (13)$$

Here, we take the $\lambda\text{-Ti}_3\text{O}_5$ compound as an example. One can see that the low-lying flat band below the Fermi level (red solid line in Fig. S1.7a), introduced by the Ti-Ti dimers, makes a major contribution to the total optical absorption coefficients within the wavelength range from ~ 500 nm to ~ 1200 nm (Fig. S1.7b). This specific wavelength range coincides well with the solar spectrum region having high radiance (Fig. S1.7c). Basically, the existence of the relatively flat bands around the Fermi level provides high joint electronic densities of states for interband optical transitions, which is of essential importance to effective optical absorption over a broad range of the solar spectrum. It is the synergistic effect of the relatively flat band and the other non-flat bands that keeps the total optical absorption coefficients of $\lambda\text{-Ti}_3\text{O}_5$ at a sufficiently high level (Fig. S1.7b), while the overall optical reflectivities are maintained to be ultralow (Fig. S1.4d). Therefore, one would expect if the relatively flat band is removed, the resultant solar absorptivity of $\lambda\text{-Ti}_3\text{O}_5$ would be significantly reduced.

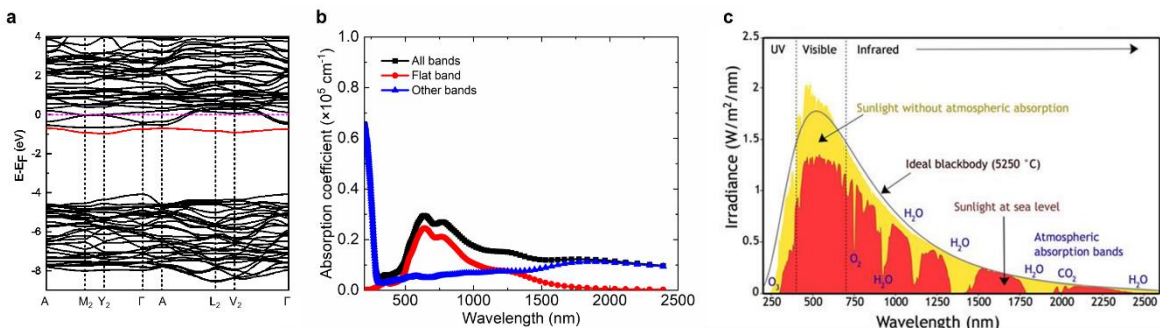


Figure S1.7. **a**, Band structure of $\lambda\text{-Ti}_3\text{O}_5$ with a relatively flat band highlighted in red solid line. **b**, Mean calculated optical absorption coefficients of $\lambda\text{-Ti}_3\text{O}_5$ within the independent-particle approximation. The red curve and the blue curve represent the contributions from the relative flat bands and the other bands, respectively. **c**, Spectrum of solar radiation (Earth).

S1.7. Optical transitions in $\lambda\text{-Ti}_3\text{O}_5$

To understand the optical transitions in TSOs, we had better know their specific octahedron crystal fields in the frame of crystal field theory (CFT). In a transition metal complex, a central metal ion exists in the

crystal field formed by negatively charged ligands, leading to the energy level splitting of the d orbitals of the central metal ion. It has been well established that within a regular ideal octahedral crystal field, the doubly-degenerate e_g orbitals ($d_{x^2-y^2}$, d_{z^2}) have a higher energy than the triply-degenerate t_{2g} orbitals (d_{xy} , d_{yz} , d_{xz}). When a distorted octahedron crystal field is involved, both the degenerate e_g and t_{2g} orbitals will be split under the action of the ligands' static electric field. The type of the energy level splitting for such degenerate d orbitals depends on the spatial configurations of the ligands.

For $\lambda\text{-Ti}_3\text{O}_5$, each Ti atom is surrounded by six nearest-neighbor O atoms to form a TiO_6 octahedron (Fig. S1.8a). However, the octahedron coordination environments around the three independent Ti sites (Ti1, Ti2 and Ti3) are different. More specifically, individual TiO_6 octahedrons are distorted in a non-symmetrical manner, and they are connected to each other by either corners, or edges, or faces (see Fig. S1.8a, left panel). As an example, the spatial configuration of two edge-shared distorted octahedrons surrounding a Ti2-Ti2 dimer is shown in Fig. S1.8b. This leads to a significant deviation from the regular ideal octahedral crystal field. According to our real-space charge density analysis of the electronic bands (Fig. S1.8c), there exist small energy level splittings of the t_{2g} -like (d_{xy} , d_{yz} , d_{xz}) states and the e_g -like ($d_{x^2-y^2}$, d_{z^2}) states, as sketched in Fig. S1.8d. Among them, the d_{xy} -like orbitals are the lowest-lying states and form the linear σ -type bonding, and they have lower energies than the d_{xz} -like and d_{yz} -like orbitals. The $d_{x^2-y^2}$ -like and d_{z^2} -like orbitals are non-degenerate any longer, and their energies are still higher than the d_{xy} -like, d_{yz} -like and d_{xz} -like orbitals.

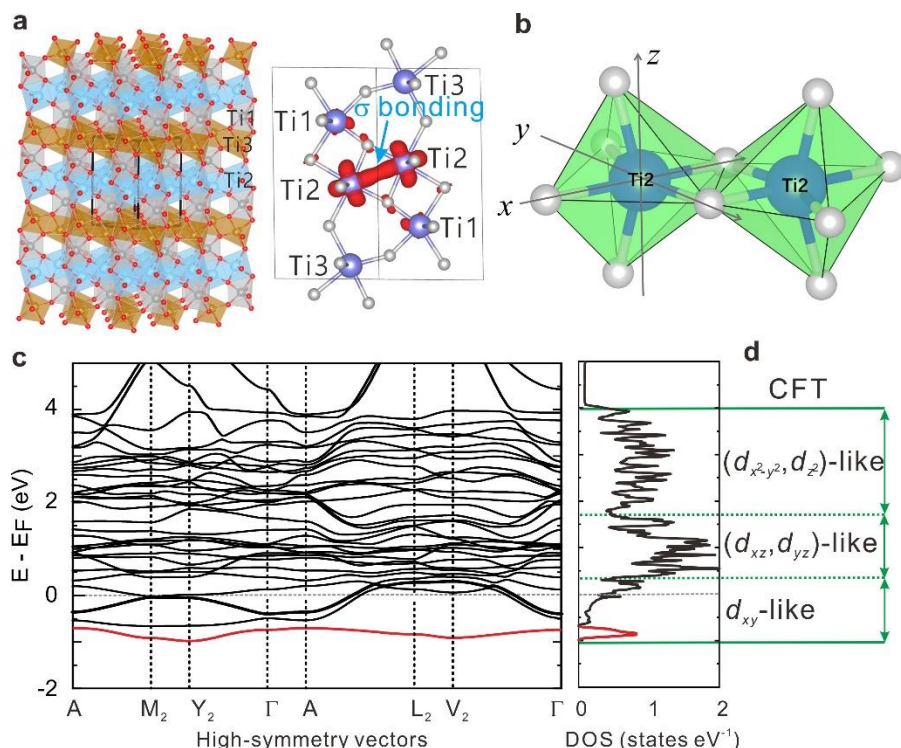


Figure S1.8. **a**, Crystal structure of $\lambda\text{-Ti}_3\text{O}_5$, highlighting the complex distorted octahedrons around three different types of Ti atoms (left panel) and the σ bonding formed by the d_{xy} -like orbitals of Ti2-Ti2 dimer (right panel). **b**, Spatial configuration of two edge-shared distorted octahedrons surrounding a Ti2-Ti2 dimer in $\lambda\text{-Ti}_3\text{O}_5$. Note that the two octahedrons are distorted in the x , y and z directions. **c**, Band structure of $\lambda\text{-Ti}_3\text{O}_5$. The low-lying flat band below the Fermi level is highlighted in red solid curve. **d**, Sketch of the crystal field splitting in $\lambda\text{-Ti}_3\text{O}_5$.

Across the entire solar spectrum range, the underlying mechanisms of optical transition in $\lambda\text{-Ti}_3\text{O}_5$ can be quite different, as illustrated in Fig. S1.9. The optical transitions in the near-infrared (NIR) region mainly arise from the intraband transitions within the partially-filled d orbitals (Fig. S1.9a). The optical transitions in the visible (Vis) and ultraviolet (UV) regions come with the interband transitions from the low-lying flat band to the (d_{xz}, d_{yz}) -like and $(d_{x^2-y^2}, d_{z^2})$ -like orbitals, respectively (Figs. S1.9b and S1.9c). Figure S1.10 and Figure S1.11 present the calculated transition dipole moments²² in the Vis and UV regions, respectively, where the optical transitions at the high-symmetry k -points with the largest transition dipole moments are identified. All the allowed optical transitions are within the Ti-3d orbitals, and they become more pronounced in the Vis region due to much larger transition dipole moments.

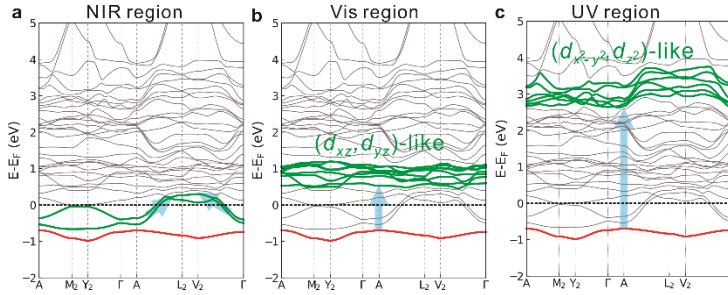


Figure S1.9, a-c, Schematic illustrations of optical transitions in $\lambda\text{-Ti}_3\text{O}_5$ in the NIR, Vis and UV regions, respectively. The optical transitions in **a** mainly arise from the intraband transitions within the partially-filled bands (solid green lines), while those in **b** and **c** come from the interband transitions between a valence band (solid red line) and one of the conduction bands (solid green lines). Note that only the allowed interband transitions with non-negligible transition dipole moments are shown. The arrows in **b** and **c** just illustrate the optical transitions at the A point.

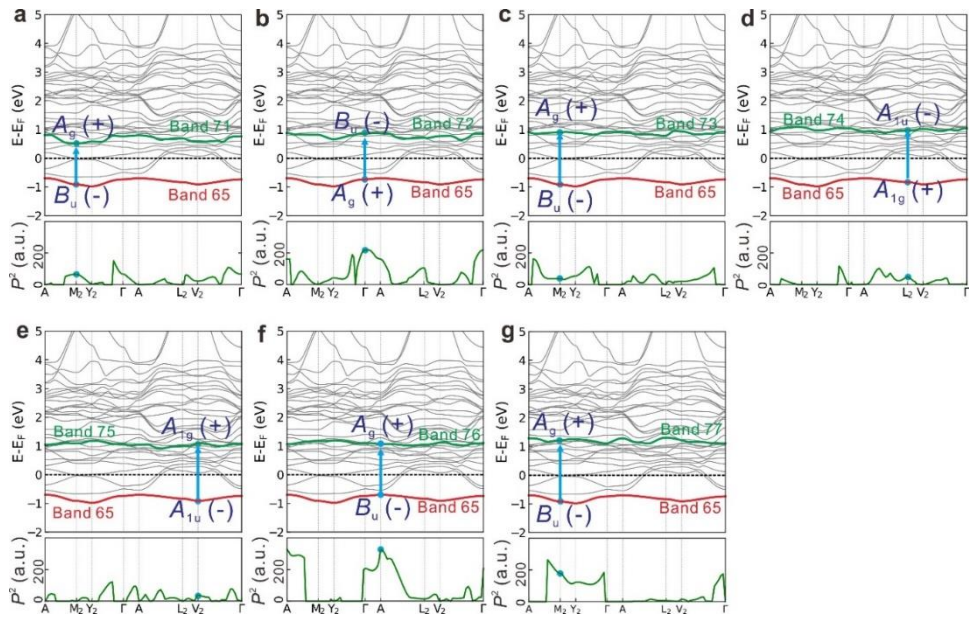


Figure S1.10, Calculated transition dipole moments of optical transitions in the Vis region. The involved occupied and unoccupied bands are indicated in red and green solid lines, respectively. The associated irreducible representations of bands at the high-symmetry k -points that contribute most to the transition dipole moments are also shown, with the parity explicitly given in brackets. Note that for the sake of brevity, the other possible optical transitions but with negligible transition dipole moments are omitted.

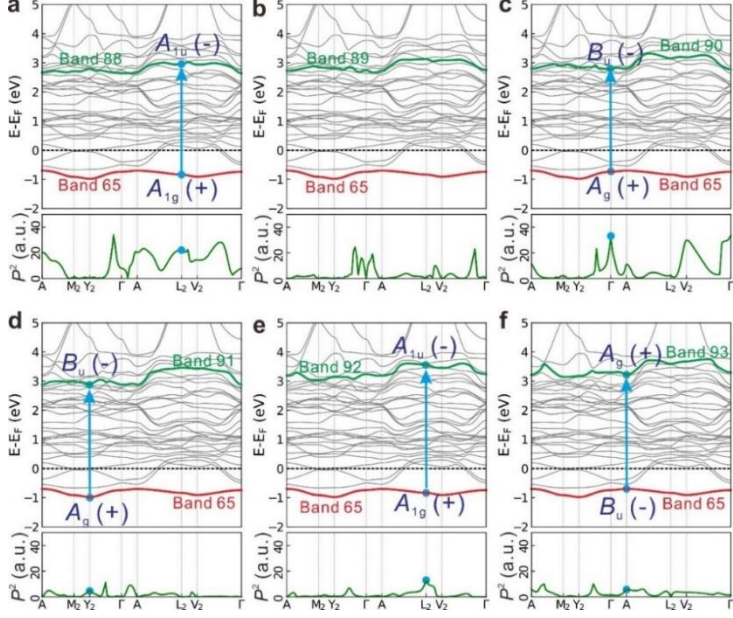


Figure S1.11. Calculated transition dipole moments of optical transitions in the UV region. The involved occupied and unoccupied bands are indicated in red and green solid lines, respectively. The associated irreducible representations of bands at the high-symmetry k -points that contribute most to the transition dipole moments are also shown, with the parity explicitly given in brackets. Note that for the sake of brevity, the other possible optical transitions but with negligible transition dipole moments are omitted.

No matter whether the solar light absorption proceeds *via* intraband optical transition or interband optical transition, photoexcited hot electrons and holes will relax back from the excited state to the ground state and release the photon energy they absorbed. In general, the relaxation dynamics in metallic systems are considered to be much faster than those in gapped systems. Also, non-radiative transitions are allowed in metallic systems during the relaxation of photoexcited hot carriers. Indeed, our photoluminescence experiment has confirmed that no photoluminescence effect was observed in the $\lambda\text{-Ti}_3\text{O}_5$ sample (see Subsection S2.4). This suggests that the absorbed photon energy can be effectively converted into heat without a loss by radiative transition, thereby triggering a high efficient thermalization. For more details on the photothermal conversion mechanism of $\lambda\text{-Ti}_3\text{O}_5$, please refer to Subsection S2.5.

Section 2. Photothermal conversion performances of TSOs

S2.1. Experimental setup of photothermal conversion measurements

The photothermal conversion performances of the different TSOs were examined under a simulated solar flux of 1 kW m^{-2} , as sketched in Fig. S2.1. Here, TSOs powders (TiO , $\text{C-Ti}_2\text{O}_3$, $\lambda\text{-Ti}_3\text{O}_5$, $\beta\text{-Ti}_3\text{O}_5$ and Ti_4O_7) were first compressed into round pills. Each pill was then put on the top of one low-density polyethylene (PE) foam (18 mm in height) with a low thermal conduction coefficient ($0.029 \text{ W m}^{-1} \text{ K}^{-1}$) to reduce the thermal loss to the surroundings. The thermal conductivity of the PE foam was determined with a thermal constants analyzer (Hotdisk 2500S, Sweden), using the transient plane source (TPS) method specified in the International Standard ISO 22007-2. The temperatures at the top and lateral surfaces of the pill during the light irradiation were detected by an infrared thermometer and an infrared thermal camera, respectively, while the temperature at the bottom of the PE foam was measured by one K-type thermocouple.

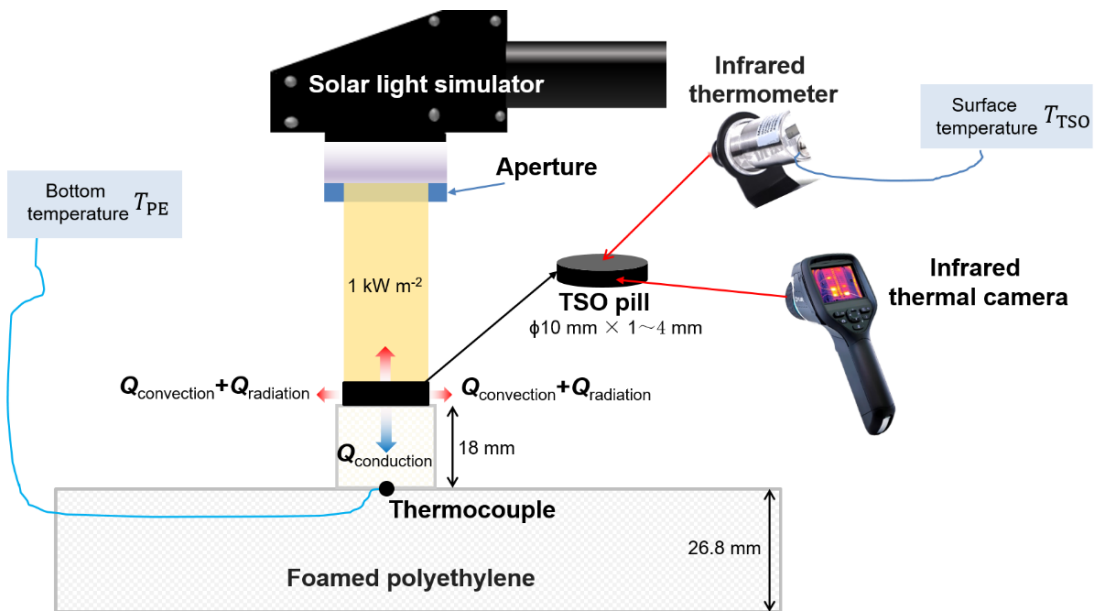


Figure S2.1. Diagrammatic sketch for measuring the photothermal conversion performances of TSO pills. An aperture is added to ensure that the solar light only covers the top surface of a tested TSO pill.

S2.2. Estimation of solar-to-heat efficiency with thermometric method

In the present experiment setup, the received solar energy is used to heat a TSO pill, along with the thermal losses through (i) conduction to the PE foam, and (ii) radiation and (iii) convection to the surroundings. In the steady condition, the quantity of heat in the TSO pill for a duration t is given by

$$Q_{\text{sample}} = C_P^{\text{TSO}} m_{\text{TSO}} (T_{\text{TSO}} - T_{\text{surr}}) t, \quad (14)$$

where C_P^{TSO} , m_{TSO} and T_{TSO} are respectively the specific heat capacity, the mass and the equilibrium temperature of the TSO pill, and T_{surr} is the temperature of the surroundings.

The thermal losses by convection, radiation and conduction are formulated as follows²³,

$$Q_{\text{convection}} = h (A_{\text{cross}}^{\text{TSO}} + A_{\text{lateral}}^{\text{TSO}}) (T_{\text{TSO}} - T_{\text{surr}}) t, \quad (15)$$

$$Q_{\text{radiation}} = \varepsilon_{\text{TSO}} \sigma (A_{\text{cross}}^{\text{TSO}} + A_{\text{lateral}}^{\text{TSO}}) (T_{\text{TSO}}^4 - T_{\text{surr}}^4) t, \quad (16)$$

$$Q_{\text{conduction}} = \lambda^{\text{PE}} A_{\text{cross}}^{\text{TSO}} \frac{dT}{dx} t. \quad (17)$$

Here, $A_{\text{cross}}^{\text{TSO}}$ and $A_{\text{lateral}}^{\text{TSO}}$ are respectively the cross-sectional area and the lateral area of the TSO pill, T_{TSO} and ε_{TSO} are respectively the surface temperature and the emissivity of the TSO pill, T_{surr} is the ambient temperature, σ is the Stefan-Boltzmann constant ($5.68 \times 10^{-8} \text{ W m}^{-2} \text{ K}^{-4}$), h is the convection coefficient ($5 \text{ W m}^{-1} \text{ K}^{-1}$), and λ^{PE} and $\frac{dT}{dx}$ are respectively the thermal conductivity and the temperature gradient of the PE foam. Accordingly, the total thermal loss reads^{23,24}

$$Q_{\text{loss}} = Q_{\text{radiation}} + Q_{\text{convection}} + Q_{\text{conduction}}. \quad (18)$$

The solar-to-heat efficiency of the TSO pill is calculated by^{23,24}

$$\eta_{\text{heat_conv}} = \frac{Q_{\text{sample}} + Q_{\text{loss}}}{Q_{\text{solar}} \bar{A}} \quad (19)$$

with

$$Q_{\text{solar}} = C_{\text{opt}} p_0 A_{\text{cross}}^{\text{TSO}} t, \quad (20)$$

where C_{opt} is the solar concentration, p_0 is the nominal direct solar irradiation (1 kW m^{-2}), and \bar{A} is the average solar absorptivity of the TSO pill defined by Eq. (12). By inserting the measured data and relevant parameters into the above expressions, one can derive the solar-to-heat efficiencies of various TSOs.

S2.3. Measured surface temperatures and calculated solar-to-heat efficiencies of TSOs

First, we took the commercial C-Ti₂O₃ powders as a model material to investigate the influences of pill thickness on the photothermal conversion under one sun irradiation. As shown in Table S2.1 and Fig. S2.2a, although the equilibrium temperature (T_{TSO}) increased significantly with the decreasing pill thickness from 4.0 mm to 1.1 mm, the calculated solar-to-heat efficiency changed slightly. This suggests that the solar-to-heat efficiency is not sensitive to the choice of pill thickness. Here, we selected a pill thickness of about 2 mm for all the considered TSOs, so as to make a direct comparison on their photothermal conversion performances. For achieving a better accuracy, the temperature measurements were conducted three times on each TSO pill, and the mean measured T_{TSO} was used to calculate the solar-to-heat efficiency.

Table S2.1. Calculated solar-to-heat efficiencies of C-Ti₂O₃ pills with different thicknesses under one sun irradiation. The specific heat capacity for C-Ti₂O₃ is taken as $0.662 \text{ J g}^{-1} \text{ }^{\circ}\text{C}^{-1}$.

Pill	Diameter (mm)	Thickness (mm)	m_{TSO} (g)	T_{TSO} ($^{\circ}\text{C}$)	T_{PE} ($^{\circ}\text{C}$)	T_{surr} ($^{\circ}\text{C}$)	Solar-to-heat efficiency (%)
1#	10	1.10	0.400	56.5 ± 0.1	29.9 ± 0.1	25.1 ± 0.1	88.1 ± 0.2
2#	10	2.05	0.510	51.5 ± 0.1	29.1 ± 0.1	25.0 ± 0.2	88.2 ± 0.2
3#	10	2.67	0.528	49.7 ± 0.1	29.3 ± 0.1	25.1 ± 0.1	89.8 ± 0.3
4#	10	4.00	1.750	44.1 ± 0.1	28.9 ± 0.1	25.0 ± 0.1	88.7 ± 0.2

The heat capacities of the different TSO compounds were characterized by means of differential scanning calorimetry (DSC, TA DSC-25)²⁵. First, the heat capacity calibration was made by running a standard sapphire ($\alpha\text{-Al}_2\text{O}_3$) over the temperature range from $-30 \text{ }^{\circ}\text{C}$ to $70 \text{ }^{\circ}\text{C}$ with a heating rate of $3 \text{ }^{\circ}\text{C}/\text{min}$ under a nitrogen flow of 50 mL/min . After the calibration, the effective temperature interval for the heat capacity measurements was set as $66.5 \text{ }^{\circ}\text{C}$, *i.e.*, from $-10 \text{ }^{\circ}\text{C}$ to $56.5 \text{ }^{\circ}\text{C}$. Then, the heat capacity measurements

of the different TSO compounds were performed under the same conditions. For each TSO compound, a set of three powder samples with a weight of ~10 mg were separately placed in an open Al crucible, and their heat flow signals were recorded at individual temperatures. Finally, the temperature-dependent heat capacities, calculated with the dataset from the three reduplicate experiments, were averaged to deliver a better reliability. Note that our mean measured heat capacities at 300 K are well consistent with the reported data for TiO , $C\text{-Ti}_2\text{O}_3$ and Ti_4O_7 ²⁶, as well as for $\lambda\text{-Ti}_3\text{O}_5$ and $\beta\text{-Ti}_3\text{O}_5$ ².

Figure S2.2b presents the measured surface temperatures of the TSO pills with the same diameter (10 mm) and similar thicknesses (~2 mm) under one sun irradiation for different time, in comparison with that of the blank PE foam. The surface temperatures of the TSO pills increased quickly at the initial stages and then approached their respective equilibrium states, whereas the surface temperature of the blank PE foam (without the layout of a TSO pill) only increased from 25.0 °C to 27.5 °C. In particular, the $\lambda\text{-Ti}_3\text{O}_5$ pill reached a surface temperature of as high as 55.7 °C within ~250 s. Such a rapid temperature increase with the solar irradiation is due to two aspects. First, the $\lambda\text{-Ti}_3\text{O}_5$ phase exhibits overall high optical absorptivities within the full solar spectrum region, which is a prerequisite for efficient solar-to-heat conversion. On the one hand, the existence of the relatively flat bands around the Fermi level makes an effective contribution to the optical absorption coefficients. On the other hand, the high joint densities of states induced by the flat bands provide more possibilities for optical excitations in a wide range of the solar spectrum. Those photoexcited hot carriers at the metastable states will finally relax back to the ground state without light emission, thereby resulting in an efficient photothermal conversion. Second, the $\lambda\text{-Ti}_3\text{O}_5$ phase exhibits a very low thermal conductivity ($\sim 0.20 \pm 0.02 \text{ W m}^{-1} \text{ K}^{-1}$)², allowing the solar-generated heat to be continually stored in the pill body until it reaches an equilibrium state.

Figure S2.2c plots the measured specific heat capacities of the TSOs as a function of temperature. At a given temperature, the specific heat capacity of the $\lambda\text{-Ti}_3\text{O}_5$ phase is generally higher than those of the other TSOs. Table S2.2 compiles the mean measured equilibrium temperatures of the TSO pills and the PE foam (for heat-insulation), as well as the calculated solar-to-heat efficiencies of the TSO pills. Among them, the $\lambda\text{-Ti}_3\text{O}_5$ pill exhibits the highest solar-to-heat efficiency with a value of ~92.4%.

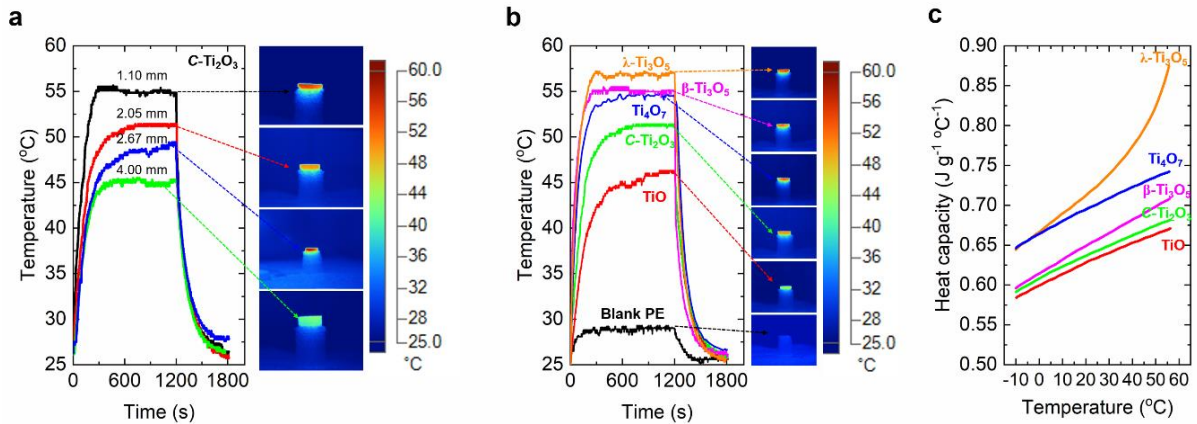


Figure S2.2. Surface temperatures and heat capacities of TSO pills. **a**, Time-dependent surface temperatures for $C\text{-Ti}_2\text{O}_3$ pills with different thicknesses under one sun irradiation (left panel) and infrared photographs taken at the irradiation time of 900 s (right panel). **b**, Time-dependent surface temperatures for various TSOs pills and blank PE foam under one sun irradiation (left panel) and infrared photographs taken at the irradiation time of 900 s (right panel). **c**, Specific heat capacities of TSOs at different temperatures.

Table S3.2, Measured equilibrium temperatures and calculated solar-to-heat efficiencies of TSO pills under one sun irradiation.

Pill	Diameter (mm)	Thickness (mm)	m_{TSO} (g)	C_p^{TSO} (J g ⁻¹ °C ⁻¹)	T_{TSO} (°C)	T_{PE} (°C)	T_{surr} (°C)	Solar-to-heat efficiency (%)
TiO	10	2.00	0.58	0.653±0.02	46.6±0.1	29.0±0.1	25.3±0.1	70.1±0.1
C-Ti ₂ O ₃	10	2.05	0.51	0.662±0.03	51.5±0.1	29.1±0.1	25.0±0.2	88.2±0.2
λ -Ti ₃ O ₅	10	2.05	0.61	0.773±0.03	55.7±0.1	29.0±0.1	25.0±0.1	92.4±0.2
β -Ti ₃ O ₅	10	2.10	0.56	0.682±0.01	55.0±0.1	29.0±0.1	25.0±0.1	90.7±0.1
Ti ₄ O ₇	10	2.10	0.71	0.723±0.02	54.2±0.1	29.0±0.2	25.2±0.2	90.4±0.3

S2.4. Measured photoluminescence spectra of λ -Ti₃O₅ powders

The photoluminescence (PL) spectra of the as-prepared λ -Ti₃O₅ powders were measured to show the absence of luminescence. To avoid the interference of diffuse reflections of the powder sample holder (quartz) on light detection, we first compressed the as-prepared λ -Ti₃O₅ powders into a round pill (10 mm in diameter and 3 mm in thickness) by room-temperature hydrostatic pressure of 200 MPa. It was then annealed at 250 °C for 10 min, allowing the pressure-induced β -Ti₃O₅ phase to transform back to the λ -Ti₃O₅ phase as verified by the XRD measurement. The PL spectra of the annealed λ -Ti₃O₅ pill sample were collected with the excitation light of 344 nm, using a photoluminescence spectrometer (FLS1000, Edinburgh Instruments Ltd). For revealing the full range PL characteristics, three detectors were adopted to record emission lights with different wavelengths, *i.e.*, PMT-900 detector (360-800 nm), PMT-1700 detector (800-1600 nm) and InGaSn detector (1200-2250 nm). During the measurements, narrow slits with a width of 2 nm were chosen for both excitation and emission lights, as to minimize the interference of diffuse reflections of the instrument. As a reference, the PL spectra of a TiO₂ pill sample (made of commercial rutile-TiO₂ powders) were also measured under the exact same test conditions.

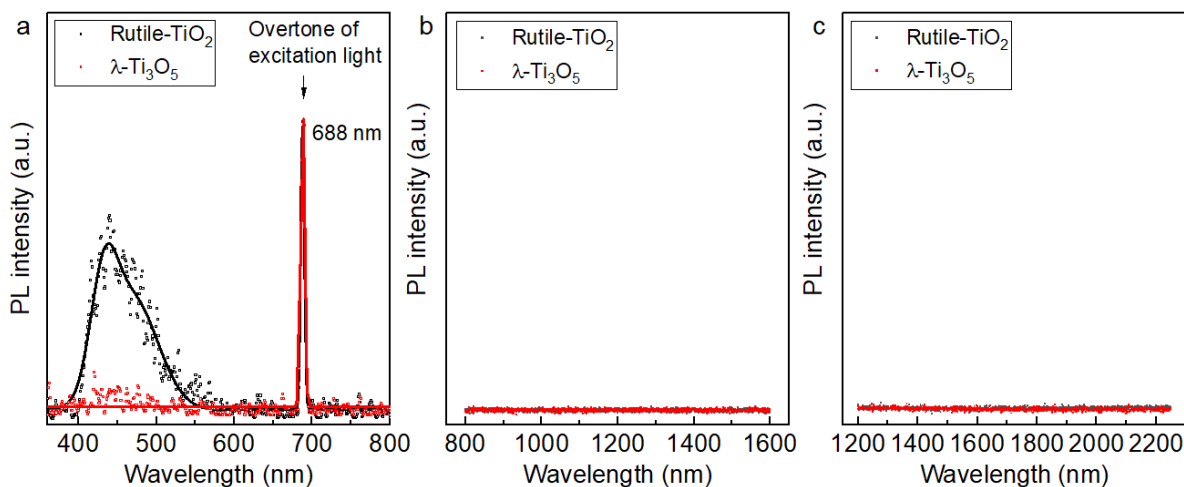


Figure S2.3, Experimental PL spectra of λ -Ti₃O₅ and rutile-TiO₂ with an excitation light of 344 nm, recorded at room temperature for emission lights with different wavelengths. **a**, 360-800 nm. **b**, 800-1600 nm. **c**, 1200-2250 nm. Note that the sharp peak in **a** (indicated by the arrow) with the wavelength of 688 nm comes from the overtone of the excitation light.

Figure S2.3 presents the PL spectra of the two-pill samples at the emission wavelengths of 360-800 nm, 800-1600 nm and 1200-2250 nm, respectively. It is seen that the rutile-TiO₂ with a bandgap of ~3.0 eV can emit luminescence with wavelengths ranging from 350 nm to 550 nm (Fig. S2.3a), which is in good agreement with the reported data²⁷. In contrast, no PL effect was detected for the λ -Ti₃O₅. It means that upon light irradiation, no PL is emitted from the λ -Ti₃O₅ during the relaxation from the excited states to the ground state. This result is reasonable as the λ -Ti₃O₅ phase is of metallic nature (see Fig. 1c in the main text).

S2.5 Photothermal conversion mechanism for λ -Ti₃O₅

Unlike most oxides, λ -Ti₃O₅ is of metallic nature rather than a semiconductor, since some of its Ti-3d electronic bands cross the Fermi level. The electrical conductivity and the carrier concentration of λ -Ti₃O₅ at room temperature were measured to be 30 S cm^{-1} ⁷ and $8.5 \times 10^{20} \text{ cm}^{-3}$ ²⁸, respectively. They are much lower than the values of $5.8 \times 10^5 \text{ S cm}^{-1}$ and $8.5 \times 10^{22} \text{ cm}^{-3}$ for the typical metal Cu^{29,30}, which suggests the poor electrical transport properties of λ -Ti₃O₅.

It is commonly known that photoexcited hot electrons can relax back from the excited state to the ground state through different channels, including radiative transition, electron-electron (*e-e*) scattering, electron-phonon (*e-ph*) interaction, and electron-hole (*e-h*) interaction, *etc.* For λ -Ti₃O₅, both *e-e* scattering and *e-ph* interaction should be considered to play key roles during the dynamical relaxation of photoexcited hot electrons, while the radiative transition and *e-h* interaction can be neglected. The main reasons are given as follows.

(1) Radiative transition does not exist in λ -Ti₃O₅. Radiative transition refers to the relaxation of hot electrons by emission of fluorescence or phosphorescence. A prerequisite of radiative transition is the existence of electronic band gap at the Fermi level, and thus this kind of transition mainly occurs in semiconductors. Nevertheless, λ -Ti₃O₅ is of metallic nature and has no electronic band gap at the Fermi level. Therefore, radiative transition should not occur in λ -Ti₃O₅, which has been evidenced experimentally in Subsection S2.4.

(2) Electron-hole interaction can be neglected in λ -Ti₃O₅. When an electron is photoexcited from valence band to conduction band, a hole will form simultaneously. Under Coulomb interaction, the hole can interact with the excited hot electron, thereby affecting the dynamic behaviors of both the hot electron and hole. In semiconductors, *e-h* interaction takes non-negligible effects on the dynamic relaxation of hot electrons. As for λ -Ti₃O₅, there exists metallic screening owing to the presence of free carries (with an electron concentration of $\sim 8.5 \times 10^{20} \text{ cm}^{-3}$ at 300 K)²⁸. As a result, the impact of *e-h* interaction on the relaxation of hot carriers can be ignored.

(3) Electron-electron scattering should exist in λ -Ti₃O₅. During the hot electron relaxation from the excited state to the ground state, hot electrons would interact with low-energy electrons under Coulomb interaction, namely *e-e* scattering. This process is thought to be the principal source of hot electron relaxation in metals, especially for hot electrons with energy of more than ~1 eV above the Fermi level³¹. Usually, the lifetime τ_{e-e} of hot electrons under *e-e* scattering is several tens of femtoseconds³². As for λ -Ti₃O₅, there are certain amount free electrons and thus the *e-e* scattering would occur during the relaxation of photoexcited hot electrons. In general, τ_{e-e} is inversely proportional to the square root of free electron concentration³³. Considering the fact that λ -Ti₃O₅ has a free electron concentration of about two orders smaller than that of Cu^{28,29}, its τ_{e-e} value might be about ten times that of Cu, *i.e.*, reaching a level of several hundred femtoseconds.

(4) Electron-phonon interaction should also exist in λ -Ti₃O₅. During the process of hot electron relaxation, hot electrons inevitably interact with lattice vibration, known as *e-ph* interaction. *e-ph* interaction

can widely exist in both metals and semiconductors. As compared to $e\text{-}e$ scattering, $e\text{-}ph$ interaction causes much smaller change in the average energy per excitation. More specifically, for a hot electron with an excitation energy $h\nu$, an $e\text{-}ph$ interaction will, on average, change the electron's energy by $\hbar\langle\omega\rangle$, whereas the most probable amount of energy exchanged in an $e\text{-}e$ scattering is as large as $h\nu^{34}$. Note that the average phonon energy $\hbar\langle\omega\rangle$ is typically 50~100 times smaller than the photon energy $h\nu^{35}$. Moreover, the lifetime $\tau_{e\text{-}p}$ of hot electrons under $e\text{-}ph$ interaction refers to several hundreds of femtoseconds³². As the magnitude of $\tau_{e\text{-}p}$ is comparable to that of $\tau_{e\text{-}e}$ in $\lambda\text{-Ti}_3\text{O}_5$, $e\text{-}ph$ interaction is of essential importance to the relaxation dynamics of photoexcited hot carriers.

For metals, nearly all $e\text{-}e$ scattering events relax high-energy excited states, whereas $e\text{-}ph$ interaction events govern relaxation dynamics near the Fermi level at low-energy excitation (*e.g.*, <1 eV)³⁵. As already addressed in Subsection S1.7, the photoexcitations in the NIR region are dominated by intraband optical transition (Fig. S2.5a), but those in the Vis and UV regions are governed by interband optical transition (Fig. S2.5b). In what follows, we aim to draw a picture of how the photoexcited hot carriers relax to the ground state and release the photon energy they absorbed, with a linkage to the two distinct light regions, *i.e.*, the NIR region and the UV-Vis region.

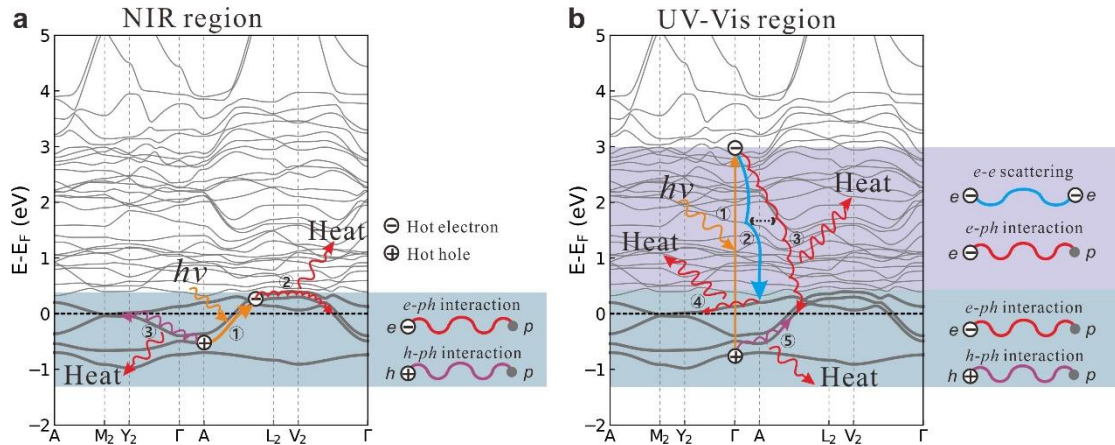


Figure S2.5. Schematic of the solar-to-heat conversion in $\lambda\text{-Ti}_3\text{O}_5$. **a**, Intraband optical transition and $e\text{-}ph/h\text{-}ph$ interactions in the NIR region. **b**, Interband optical transition, $e\text{-}e$ scattering and $e\text{-}ph/h\text{-}ph$ interactions in the UV-Vis region. Note that the $e\text{-}e$ scattering and $e\text{-}ph$ interactions in **b** may exchange during the relaxation of excited hot electrons, as indicated by dotted line with double arrows.

(1) Relaxation dynamics of hot electrons excited with NIR light is dominated by $e\text{-}ph$ interactions in $\lambda\text{-Ti}_3\text{O}_5$. With decreasing photoexcitation energy, the phase spaces of excited hot electrons are drastically narrowed in metals, leading to a significantly extended $\tau_{e\text{-}e}$ under $e\text{-}e$ scattering^{32,36}. Such behaviors can be approximately approached by the energy dependence of $\tau_{e\text{-}e} \propto (E - E_F)^2$, where E and E_F represent the excitation energy of hot electrons and the Fermi energy, respectively³⁷. The extended $\tau_{e\text{-}e}$ significantly weakens the contribution of $e\text{-}e$ scattering within the NIR region. This is the reason why $e\text{-}ph$ interactions usually dominate the relaxation process of low-energy hot electrons (<~1 eV)³⁵. As schematically shown in Fig. S2.5a, when a low-energy NIR photon is subjected to $\lambda\text{-Ti}_3\text{O}_5$, an electron can be excited *via* intraband optical transition (①) to form a hot electron and a hot hole. Both the hot electron (②) and hot hole (③) gradually relax back onto the Fermi surface through intraband relaxation. During this process, the thermalization of $\lambda\text{-Ti}_3\text{O}_5$ is realized by $e\text{-}ph$ and $h\text{-}ph$ interactions.

(2) Both *e-e* scattering and *e-ph* interaction play important roles in relaxation of hot electrons excited with UV-Vis lights. As schematically shown in Fig. S2.5b, when a high-energy UV-Vis photon is subjected to $\lambda\text{-Ti}_3\text{O}_5$, an electron can be excited *via* interband optical transition (①) to form a hot electron and a hot hole. There exist two channels for the hot electron relaxation, *i.e.*, *e-e* scattering (②) and *e-ph* interaction (③). i) In the route of *e-e* scattering (②), the hot electron inelastically collides with cold electron, where a large amount of energy is transferred from the hot electron to a cold one. However, no heat is released during this process. Once the high-energy hot electron is relaxed to a low-energy state close to the Fermi level, the contribution of *e-e* scattering weakens significantly. Instead, *e-ph* interactions (④) turn to dominate the hot electron relaxation with heat release. ii) In the route of *e-ph* interaction (③), the hot electron interacts with lattice vibration during the relaxation process, where the energy of the hot electron transfers to phonons with heat release to the lattice. It is should be noted that within the UV-Vis region, the relaxation channels of *e-e* scattering and *e-ph* interaction are not fully separated, and for a certain portion of hot electrons they can interchange to each other, as indicated by the dotted line with double arrows in Fig. S2.5b. In similarity to the hot electron, the excited hole also relaxes to the Fermi surface by *h-ph* interaction (⑤) with heat release.

In conclusion, for $\lambda\text{-Ti}_3\text{O}_5$ both *e-e* scattering and *e-ph* interaction play critical roles in the relaxation process of photoexcited hot electrons. The relaxation dynamics of hot electrons excited with the NIR light is dominated by *e-ph* interactions, while both *e-e* scattering and *e-ph* interaction are effective for the relaxation of hot electrons excited with the UV-Vis lights. As already addressed in Subsection 1.4, $\lambda\text{-Ti}_3\text{O}_5$ exhibits an effective optical absorption over the full solar spectrum due to the multiple flat band structure near the Fermi level. No matter whether the incident light is in the NIR region or in the UV-Vis region, the absorbed photon energy is converted into heat without radiative transition. It is worth noting that the multiple flat bands around E_F , consisting of strong localized Ti-3d states, result in high densities of electronic states. On the one hand, a high 3d electronic density near E_F leads to a faster relaxation rate and hence to a shorter inelastic lifetime of excited hot electrons³⁸. On the other hand, 3d electrons may also give rise to screening that tends to extend the lifetime of excited electrons. Nevertheless, the weak metallicity of $\lambda\text{-Ti}_3\text{O}_5$ renders itself a relatively small screening effect as compared with typical metals. Hence, it is believed that for $\lambda\text{-Ti}_3\text{O}_5$ the multiple flat bands of Ti-3d states around E_F facilitate the process of photoexcited carrier relaxation and heat release, in addition to solar light absorption.

Section 3. Solar evaporation performance and water vaporization enthalpy of two-dimensional (2D) evaporator system

S3.1. Experimental setup of 2D solar steam evaporator system

The experimental setup for the 2D solar steam evaporator (2D-SSE) system is schematically shown in Fig. S3.1. Individual 2D evaporators (30 mm in diameter and ~100 μm in height) were fabricated by dispersing the light-absorbing TSO powders onto a cellulose membrane through vacuum suction filtration. One low-density PE foam sheet with a punched hole in the center was employed as the supporting and thermal-insulation layer of the cellulose membrane, where the punched hole was embedded with a cotton core for water supply. The integrated 2D-SSE system was capable of floating on bulk water with reduced thermal losses, due to the light weight (0.01 g cm^{-3}), low thermal conductivity ($\sim 0.029 \text{ W m}^{-1} \text{ K}^{-1}$) and hydrophobic nature of the PE foam with closed cells. During the water evaporation measurements, an aperture was added to ensure that the solar light only covers the top surface of 2D-SSEs³⁹. For comparison, the direct evaporation from bulk water was also conducted by removal of 2D-SSE from the integrated 2D-SSE system.

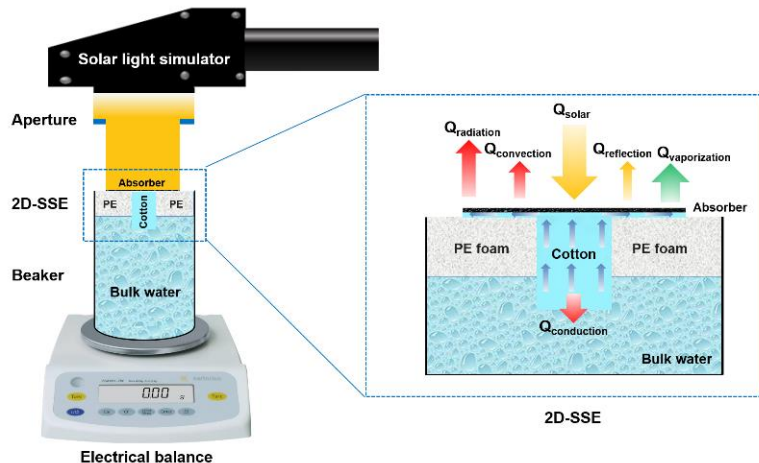


Figure S3.1. Diagrammatic sketch for measuring the solar evaporation performance of 2D-SSE in an open environment.

S3.2. Measured water evaporation rates of 2D-SSEs using different TSOs

The water evaporation performances of the 2D-SSEs were examined under one sun irradiation and dark condition, where the as-prepared $\lambda\text{-Ti}_3\text{O}_5$, $\beta\text{-Ti}_3\text{O}_5$ and Ti_4O_7 powders and the commercial TiO and $C\text{-Ti}_2\text{O}_3$ powders were used as light absorbers, respectively. As shown in Fig. S3.2, the water evaporation rates of the 2D-SSEs in a dark condition are almost the same ($0.20\text{--}0.22 \text{ kg m}^{-2} \text{ h}^{-1}$), which is more than two times that of bulk water ($0.09\pm0.008 \text{ kg m}^{-2} \text{ h}^{-1}$). Under one sun irradiation, the water evaporation rates for the 2D-SSEs using the light-absorbing TiO , $C\text{-Ti}_2\text{O}_3$, Ti_4O_7 , $\lambda\text{-Ti}_3\text{O}_5$ and $\beta\text{-Ti}_3\text{O}_5$ powders are respectively $1.01\pm0.01 \text{ kg m}^{-2} \text{ h}^{-1}$, $1.34\pm0.02 \text{ kg m}^{-2} \text{ h}^{-1}$, $1.37\pm0.02 \text{ kg m}^{-2} \text{ h}^{-1}$, $1.64\pm0.02 \text{ kg m}^{-2} \text{ h}^{-1}$ and $1.45\pm0.02 \text{ kg m}^{-2} \text{ h}^{-1}$, compared to the value of $0.39\pm0.02 \text{ kg m}^{-2} \text{ h}^{-1}$ for the direct evaporation from bulk water (*i.e.*, without 2D-SSE). Note that our mean measured evaporation rates of bulk water and the $C\text{-Ti}_2\text{O}_3$ 2D-SSE under one sun irradiation are in nice agreement with the reported values, *i.e.*, $0.4 \text{ kg m}^{-2} \text{ h}^{-1}$ for bulk water and $1.32 \text{ kg m}^{-2} \text{ h}^{-1}$ for the $C\text{-Ti}_2\text{O}_3$ evaporator⁶. Among all the considered TSOs, the 2D-SSE made with the as-prepared $\lambda\text{-Ti}_3\text{O}_5$ powders exhibits the largest water evaporation rate under one sun irradiation.

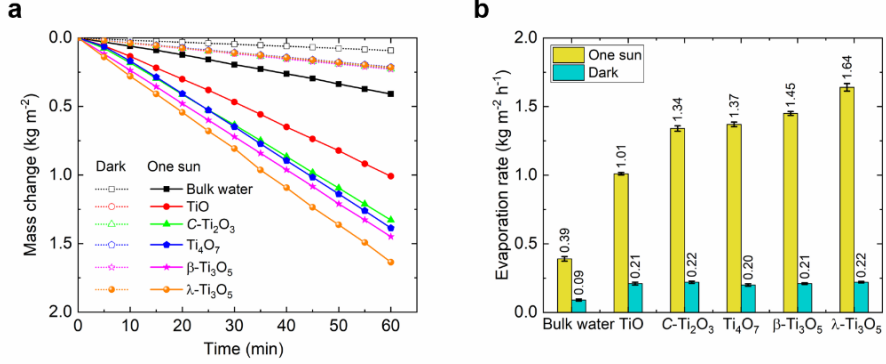


Figure S3.2. Water evaporation performances of the 2D-SSEs (30 mm in diameter and $\sim 100 \mu\text{m}$ in height) with various light-absorbing TSOs under dark and one sun irradiation, in comparison with the direct evaporation from bulk water. **a**, Water mass change *vs* time. **b**, Mean measured evaporation rates. The error bars are the standard deviations of the mean ($n = 3$, n is the number of evaporation rates for each sample used to derive statistics).

S3.3. Estimation of water vaporization enthalpy and solar-to-steam efficiency with thermometric method

Herein, both the water vaporization enthalpy and solar-to-steam efficiency of a 2D-SSE system are estimated with the thermometric method. The computation procedure is similar to that for calculating the solar-to-heat efficiencies of TSOs, as described below.

When a solar irradiation is subjected to the surfaces of light-absorbing TSO powders, the received energy (Q_{receive}) of the 2D-SSE within a duration t reads

$$Q_{\text{receive}} = Q_{\text{solar}} - Q_{\text{reflection}} \quad (21)$$

with

$$Q_{\text{solar}} = C_{\text{opt}} p_0 A_{\text{2D-SSE}} t \quad (22)$$

and

$$Q_{\text{reflection}} = (1 - \bar{A}) Q_{\text{solar}}, \quad (23)$$

where $A_{\text{2D-SSE}}$ is the projected area of the 2D-SSE, and \bar{A} is the average solar absorptivity of the TSO powders. The percentage of the reflected solar energy is given by $\eta_{\text{reflection}} = Q_{\text{reflection}}/Q_{\text{solar}} = 1 - \bar{A}$.

In a steady state, the received energy, Q_{receive} , is consumed by the heat applied for water vaporization ($Q_{\text{vaporization}}$), and the thermal losses *via* radiation into the surroundings ($Q_{\text{radiation}}$), convection into the surrounding air ($Q_{\text{convection}}$) and conduction into bulk water ($Q_{\text{conduction}}$). From the viewpoint of energy equilibrium, one has

$$Q_{\text{vaporization}} = Q_{\text{receive}} - Q_{\text{radiation}} - Q_{\text{convection}} - Q_{\text{conduction}}. \quad (24)$$

The radiative thermal loss, $Q_{\text{radiation}}$, is calculated according to the Stefan-Boltzmann equation^{24,40},

$$Q_{\text{radiation}} = A_{\text{2D-SSE}} \varepsilon_{\text{2D-SSE}} \sigma (T_{\text{2D-SSE}}^4 - T_{\text{envir}}^4) t, \quad (25)$$

where $\varepsilon_{\text{2D-SSE}}$ is the emissivity of the 2D-SSE, $T_{\text{2D-SSE}}$ is the average surface temperature of the 2D-SSE at the steady-state condition, and T_{envir} is the temperature of the surroundings. The percentage of the radiative thermal loss is given by $\eta_{\text{radiation}} = Q_{\text{radiation}}/Q_{\text{solar}}$.

The convective thermal loss, $Q_{\text{convection}}$, is calculated according to the Newton's law of the cooling^{24,40},

$$Q_{\text{convection}} = A_{\text{2D-SSE}} h (T_{\text{2D-SSE}} - T_{\text{envir}}) t, \quad (26)$$

where h is the heat transfer coefficient of air ($5 \text{ W m}^{-2} \text{ K}^{-1}$). The percentage of the convective thermal loss is given by $\eta_{\text{convection}} = Q_{\text{convection}}/Q_{\text{solar}}$.

The conductive thermal loss, $Q_{\text{conduction}}$, is defined by⁴⁰

$$Q_{\text{conduction}} = C_P^{\text{bulk water}} m_{\text{bulk water}} \Delta T_{\text{bulk water}}, \quad (27)$$

where $C_P^{\text{bulk water}}$ is the specific heat capacity of bulk water ($4.2 \text{ kJ kg}^{-1} \text{ K}^{-1}$), $m_{\text{bulk water}}$ is the mass of bulk water in the beaker, and $\Delta T_{\text{bulk water}}$ is the temperature rise of bulk water for the duration t . The percentage of the conductive thermal loss is given by $\eta_{\text{conduction}} = Q_{\text{conduction}}/Q_{\text{solar}}$.

The heat applied for water vaporization, $Q_{\text{vaporization}}$, is comprised of two terms as follows²³,

$$Q_{\text{vaporization}} = \dot{m} \Delta H_{\text{vap}} + \dot{m} C_P^{\text{bulk water}} (T_{\text{2D-SSE}} - T_{\text{bulk water}}), \quad (28)$$

where \dot{m} is the dark-excluded mass change of the generated vapor for the duration t , ΔH_{vap} is the phase change enthalpy from liquid water to vapor at the surface temperature of the 2D-SSE, and $T_{\text{bulk water}}$ is the temperature of bulk water in the beaker under the solar irradiation for the duration t . The first term in the right side of the above equation represents the phase change latent heat from liquid water to vapor, and the second term is the sensible heat associated with the temperature rising from $T_{\text{bulk water}}$ to $T_{\text{2D-SSE}}$. Here, \dot{m} is directly determined from the measured evaporation rates (r_{evap}) of the 2D-SSE under dark and solar irradiation, *i.e.*, $\dot{m} = (r_{\text{evap}}^{\text{solar}} - r_{\text{evap}}^{\text{dark}}) A_{\text{2D-SSE}} t$. With the calculated values for Q_{receive} , $Q_{\text{radiation}}$, $Q_{\text{convection}}$ and $Q_{\text{conduction}}$, one can derive $Q_{\text{vaporization}}$ according to Eq. (24) and ΔH_{vap} from Eq. (28). Moreover, the solar-to-steam efficiency is calculated by $\eta_{\text{solar_steam}} = Q_{\text{vaporization}}/Q_{\text{solar}}$.

S3.4. Calculated water vaporization enthalpy and solar-to-steam efficiency for 2D λ -Ti₃O₅ evaporator

With the integrated 2D-SSE system, we have investigated the solar-to-steam efficiency using various TSOs as light absorbers. For the 2D λ -Ti₃O₅ evaporator (30 mm in diameter and $\sim 100 \mu\text{m}$ in height), its surface temperature increased rapidly to the equilibrium state ($\sim 39.6^\circ\text{C}$) upon one sun illumination, but changed slightly in the dark condition (Fig. S3.3). The average hourly evaporation rates are $1.64 \text{ kg m}^{-2} \text{ h}^{-1}$ under one sun irradiation and $0.22 \text{ kg m}^{-2} \text{ h}^{-1}$ under dark, respectively. Table S3.1 lists various parameters used for the present calculations. According to Eqs. (23), (25), (26) and (27), the solar energy loss by reflection is 3.59%, while the thermal losses by radiation, convection and conduction are 8.85%, 7.04% and 12.22%, respectively. Thus, the solar-to-steam efficiency of the 2D λ -Ti₃O₅ evaporator is 68.30% under one sun irradiation. Interestingly, the vaporization enthalpy (ΔH_{vap}) of water adsorbed on the λ -Ti₃O₅ surface is reduced to 1696 kJ kg^{-1} at 39.6°C , as compared to a value of 2412 kJ kg^{-1} for bulk water at 40°C ^{23,41}.

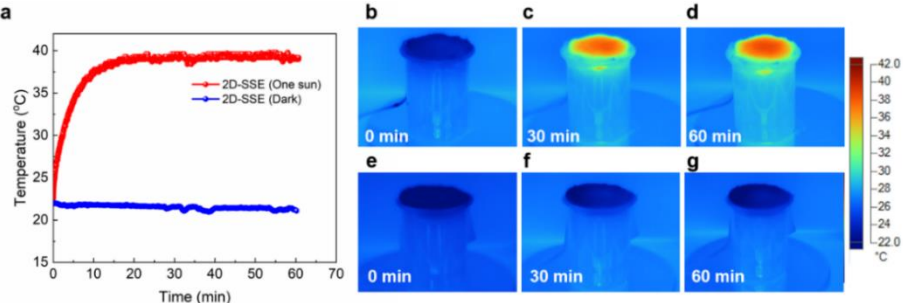


Figure S3.3. Surface temperature variations under dark and one sun irradiation for the 2D-SSE made of λ -Ti₃O₅ powders. **a**, Surface temperatures vs time. **b-d**, Infrared photographs at 0 min, 30 min, and 60 min under one sun irradiation. **e-g**, Infrared photographs at 0 min, 30 min, and 60 min under dark condition.

Table S3.1. Parameters for calculating the water vaporization enthalpy and solar-to-steam efficiency of 2D λ -Ti₃O₅ evaporator.

C_{opt}	1	$A_{\text{2D-SSE}}$	$7.06858 \times 10^{-4} \text{ m}^2$
p_0	1 kW m^{-2}	$m_{\text{bulk water}}$	25 g
t	1 h	$T_{\text{2D-SSE}}$	39.6 °C
$\varepsilon_{\text{2D-SSE}}$	0.97	T_{enivr}	25.5 °C
h	$5 \text{ W m}^{-2} \text{ K}^{-1}$	$\Delta T_{\text{bulk water}}$	2.96 °C
σ	$5.68 \times 10^{-8} \text{ W m}^{-2} \text{ K}^{-4}$	$T_{\text{bulk water}}$	31.14 °C
$C_P^{\text{bulk water}}$	$4.2 \times 10^3 \text{ J kg}^{-1} \text{ K}^{-1}$	$r_{\text{evap}}^{\text{solar}}$	$1.64 \text{ kg m}^{-2} \text{ h}^{-1}$
\bar{A}	0.9641	$r_{\text{evap}}^{\text{dark}}$	$0.22 \text{ kg m}^{-2} \text{ h}^{-1}$

S3.5. Experimental vaporization enthalpy of water on the surfaces of λ -Ti₃O₅ powders

In order to validate the estimated vaporization enthalpy of interfacial water on the λ -Ti₃O₅ surface, we have performed more intuitive thermodynamic measurements using the DSC method. Here, the DSC experiments were conducted on bulk water and interfacial water adsorbed to the λ -Ti₃O₅ surface, respectively. For the case of bulk water, 47.21 mg water was directly placed in an open Al crucible. As for the case of interfacial water, 21.79 mg λ -Ti₃O₅ powders were placed in an open Al crucible, and then 4.34 mg water was dropped on the surfaces of the λ -Ti₃O₅ powders *via* a pipette gun. Two heating schemes were adopted for the heat-flow measurements. One referred to the continuous heating from 10 °C to 160 °C with a heating rate of 5 K/min, as frequently used in the previous studies⁴²⁻⁴⁴. The other referred to the isothermal heating at a fixed temperature of 40 °C, being very close to the surface temperature (~39.6 °C) of the 2D λ -Ti₃O₅ evaporator upon one sun illumination. All the measurements were conducted under a nitrogen flow of 25 mL/min.

Figure S3.4a shows the change of heat flow signal as a function of temperature. In this case, the values of water vaporization enthalpy can be obtained *via* integrating the heat flow over the temperature interval and dividing it by the heating rate. The vaporization enthalpy for bulk water was determined to be 2437 kJ kg⁻¹, which is very close to the value of 2412 kJ kg⁻¹ calculated using the empirical formula ($40 \text{ }^\circ\text{C}$, $1.91846 \times 10^6 \times T_{\text{vapour}}^2 / (T_{\text{vapour}} - 33.91)^2$)^{23,41}. In contrast, the vaporization enthalpy of interfacial water on the λ -Ti₃O₅ surface was about 1748 kJ kg⁻¹, which is much lower than that of bulk water. It should be pointed out that the so-obtained water vaporization enthalpies are not the ones at a constant temperature, but averaged over a chosen temperature interval.

Figure S3.4b presents the change of heat flow signal as a function of heating time at 40 °C. Through integrating the heat flow over the time interval, one can obtain the water vaporization enthalpies accordingly. The measured values are 2444 kJ kg⁻¹ for bulk water and 1757 kJ kg⁻¹ for interfacial water on the λ -Ti₃O₅ surface, respectively. Note that the experimental vaporization enthalpy of interfacial water on the λ -Ti₃O₅ surface by the DSC measurements is very close to the one (1696 kJ kg⁻¹) estimated with the water evaporation experiments.

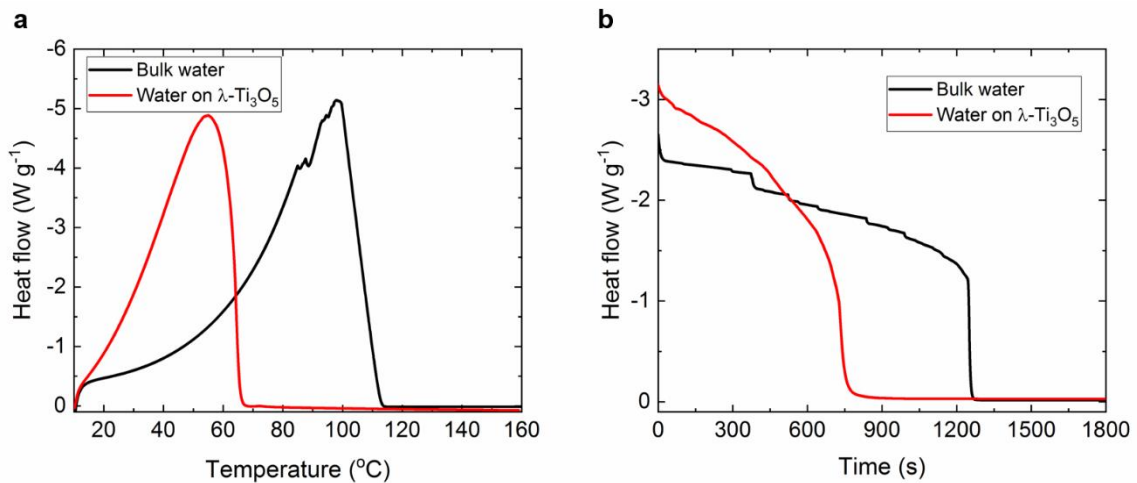


Figure S3.4. Thermograms of bulk water and interfacial water on the $\lambda\text{-Ti}_3\text{O}_5$ surface. **a**, Heat flow signal as a function of temperature from 10 °C to 160 °C. **b**, Heat flow signal as a function of heating time at 40 °C.

Section 4. Theoretical calculations of water adsorption and dissociation on λ -Ti₃O₅ surface

S4.1. First-principles calculations of surface energies of λ -Ti₃O₅

The surface energy of the λ -Ti₃O₅ phase, σ_{surf} , is calculated by

$$\sigma_{\text{surf}} = \frac{1}{2A} (E_{\text{slab}} - N_{\text{Ti}}\mu_{\text{Ti}} - N_{\text{O}}\mu_{\text{O}}), \quad (29)$$

where E_{slab} refers to the total energy of the relaxed slab model, μ_{Ti} (μ_{O}) is the chemical potential of Ti (O), N_{Ti} (N_{O}) is the number of Ti (O) atoms in the slab, and A is the area of the surface. The chemical potential of the λ -Ti₃O₅ phase, $\mu_{\text{Ti}_3\text{O}_5}^{\text{bulk}}$, is expressed as

$$\mu_{\text{Ti}_3\text{O}_5}^{\text{bulk}} = 3\mu_{\text{Ti}} + 5\mu_{\text{O}}. \quad (30)$$

Substituting Eq. (30) into Eq. (29), it yields

$$\sigma_{\text{surf}} = \frac{1}{2A} \left[E_{\text{slab}} - \frac{1}{3} N_{\text{Ti}} \mu_{\text{Ti}_3\text{O}_5}^{\text{bulk}} + N_{\text{O}} \left(\frac{5}{3} N_{\text{Ti}} - N_{\text{O}} \right) \mu_{\text{O}} \right]. \quad (31)$$

In addition, the chemical potential of each species on a stable surface should be less than that of its bulk phase, *i.e.*,

$$\mu_{\text{Ti}} \leq \mu_{\text{Ti}}^{\text{bulk}}, \quad \mu_{\text{O}} \leq \frac{1}{2} \mu_{\text{O}_2}^{\text{gas}}. \quad (32)$$

Thus, μ_{O} was limited in a range from -10.060 eV to -4.585 eV in this study.

Here, we built seven surface models with different terminations and miller indices for the λ -Ti₃O₅ phase. All slabs had two symmetric surfaces, and these surfaces were separated by a vacuum layer of 20 Å to eliminate interactions caused by periodic images. Details of these models are shown in Table S4.1. In our first-principles calculations, the energy cutoff was set to 520 eV, and the k -point spacing was 0.04 Å⁻¹. The calculated surface energies of the considered surfaces with different terminations are shown in Fig. S4.1. Clearly, the (1̄10) surface is the most energetically stable one within the allowed oxygen chemical potentials.

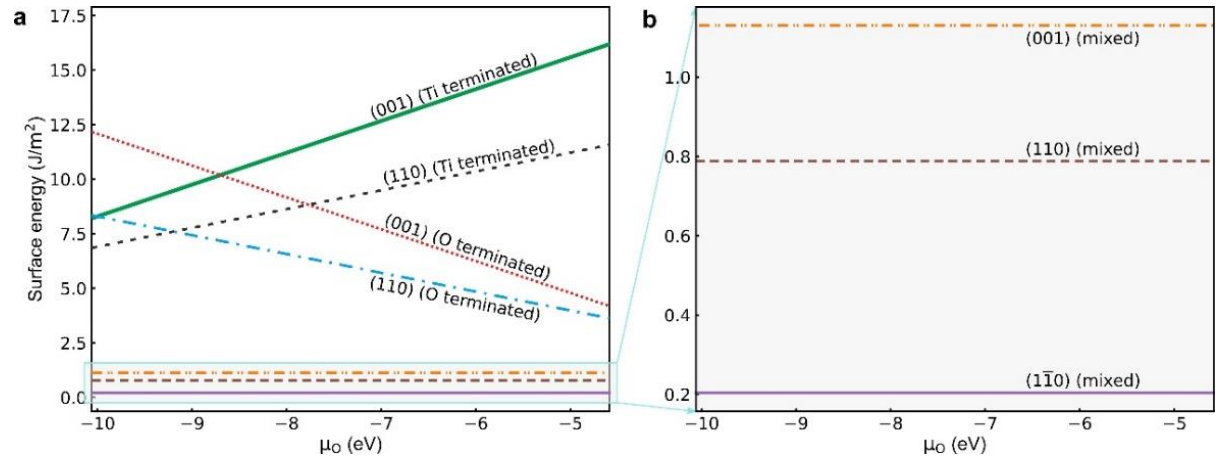


Figure S4.1. **a**, Calculated surface energies of considered three surfaces with different terminations for λ -Ti₃O₅. **b**, Zoom-in plot of **a**.

Table S4.1. Details of surface models for the λ - Ti_3O_5 phase used in the surface energy calculations.

Surface	Termination	Number of atoms		Thickness (Å)
		Ti	O	
(001)	Mixed Ti and O	12	20	18.4
	Ti terminated	14	20	20.7
	O terminated	13	25	23.3
(110)	Mixed Ti and O	24	40	18.6
	Ti terminated	24	36	17.0
	O terminated	24	44	20.3
(1̄10)	Mixed Ti and O	36	60	18.8

S4.2. First-principles calculations of preference sites for water adsorption on λ - Ti_3O_5 (1̄10) surface

In order to predict the preference sites for water adsorption on the surfaces of λ - Ti_3O_5 , we calculated the water molecule adsorption energies with or without the inclusion of van der Waals interaction (vdW). A six-layered slab model was employed for the λ - Ti_3O_5 (1̄10) surface, including 36 Ti atoms and 60 O atoms. The vacuum length was set to 20 Å. In each calculation, a $2 \times 2 \times 1$ Γ -centered k -point mesh was used. Each layer of the slab modeling contains 6 Ti atoms and 10 O atoms. The cut-off energy for the plane waves was set to 520 eV. The convergence criterion for the ionic relaxation and electronic iteration was set to -0.02 eV/Å and 10^{-5} eV, respectively. The vdW interaction was treated via the Grimme's D3 method⁴⁵. Although the calculated adsorption energies per H_2O molecule became more negative when the vdW interaction was included, the preference sites of the water adsorption and the general trends of the site-dependent adsorption energy remained almost unchanged. Unless otherwise mentioned below, the calculated adsorption energies refer to the values with the vdW interaction.

To examine possible sites for water adsorption on the λ - Ti_3O_5 (1̄10) surface, different coverages of water molecules on this specific surface should be considered. We found that the water adsorption is always favored on the exposed surface Ti atoms. In principle, the configuration space grows combinatorically with the increase of water molecules. Thus, it is extremely difficult to determine the most stable ground-state configuration for the adsorption of water molecules among all possibilities. Here, we restricted our calculations to some selected configurations, *e.g.*, 18 configurations for a single water molecule and 15 configurations for two water molecules. Under all the considered configurations, the calculated adsorption energies per water molecule vary from -0.14 eV to -1.15 eV for one single undissociated water molecule (Fig. S4.2) and from -0.84 eV to -1.13 eV for two undissociated water molecules (Fig. S4.3). Until all the surface Ti atoms have been chemisorbed by undissociated water molecules, the (1̄10) surface will no longer chemically adsorb other water molecules. Note that the calculated adsorption energies are all negative for the considered configurations, revealing the hydrophilic nature of the surface.

According to our calculations, the chemisorbed water molecules on the λ - Ti_3O_5 (1̄10) surface can readily dissociate into OH groups and H atoms. When one single water molecule is adsorbed, the decomposed OH group and H atom are respectively bonded with a surface Ti atom of Ti-Ti dimers and a surface oxygen (O_s) atom. In particular, we analyzed the water dissociation in detail by varying the number (N_{dis}) of the dissociated water molecules when the maximum 6 water molecules are chemisorbed on the λ - Ti_3O_5 (1̄10) surface. Among them, the most stable configuration is the one with $N_{\text{dis}}=3$, yielding the lowest adsorption energy of -0.948 eV per water molecule (Fig. S4.4). This corresponds to the largest total binding energy of

5.688 eV. In this configuration, three water molecules are dissociated, while the other three molecules keep undissociated. The dissociated three OH groups and three H atoms are, respectively, bonded to three surface Ti atoms and three surface O_s atoms to form six OH groups including three OH groups and three O_sH groups (see Fig. 3c in the main text). Note that this most stable configuration is consistent with the findings from our long-term (100 ps) *ab initio* molecular dynamics (AIMD) simulations.

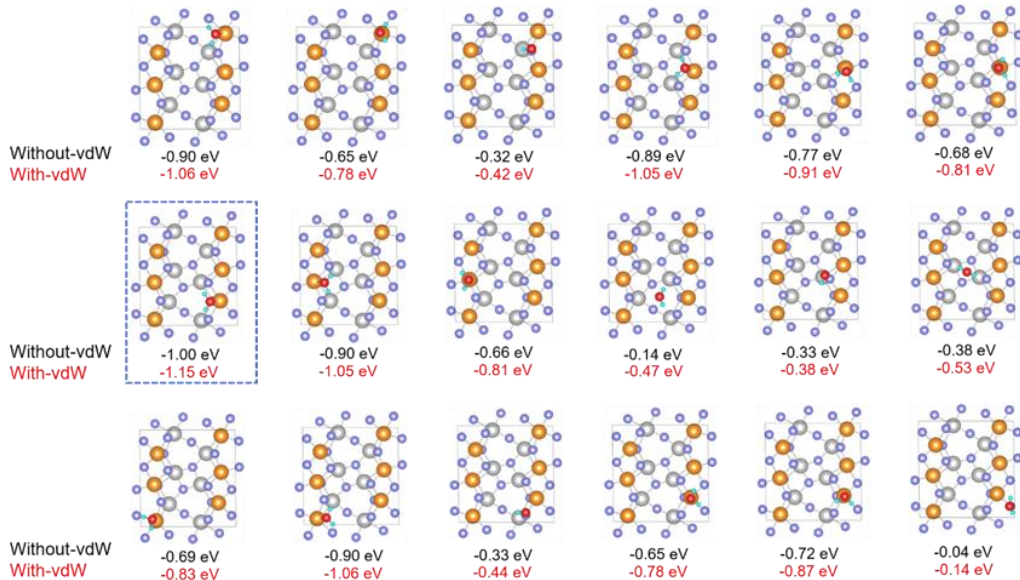


Figure S4.2. Calculated adsorption energies per H₂O molecule for one single water molecule adsorbing at different sites of the $\lambda\text{-Ti}_3\text{O}_5$ (1̄10) surface with and without taking into account the vdW interaction. The dashed blue rectangle outlines the most stable adsorption site among the considered configurations.

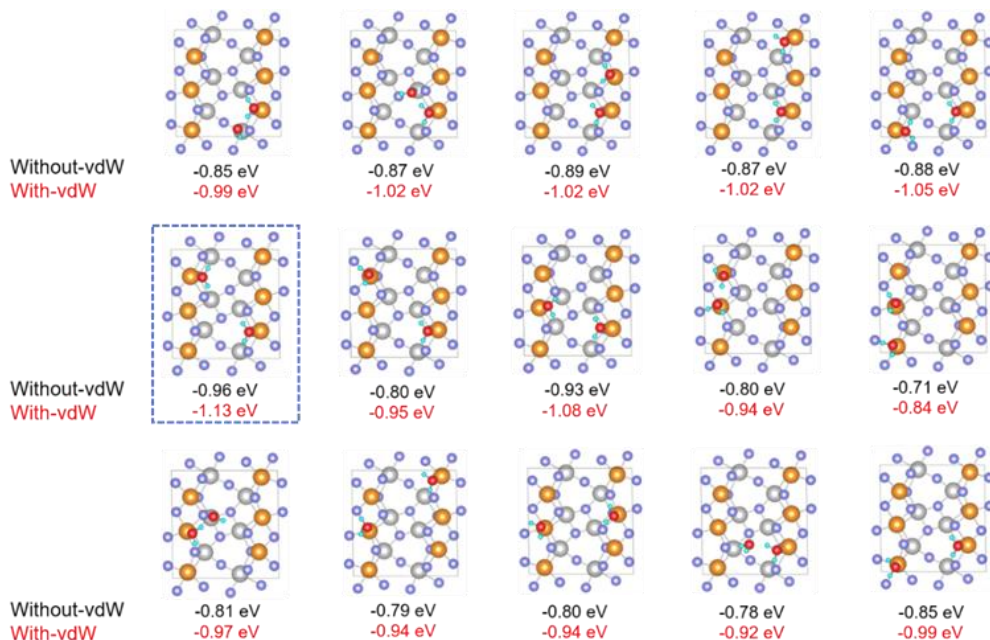


Figure S4.3. Calculated adsorption energies per H₂O molecule for two neighboring water molecules adsorbing at different sites of the $\lambda\text{-Ti}_3\text{O}_5$ (1̄10) surface with and without taking into account the vdW interaction. The dashed blue rectangle outlines the most stable adsorption site among the considered configurations.

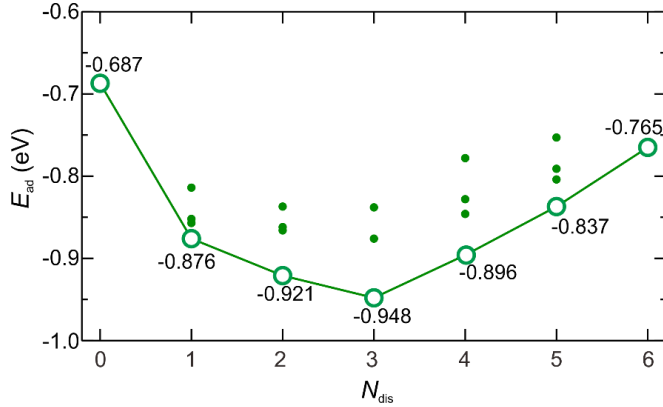


Figure S4.4. Calculated adsorption energy (E_{ad}) per H_2O molecule for six water molecules adsorbing on the $(1\bar{1}0)$ surface against the number (N_{dis}) of the dissociated water molecules. All these calculations included the vdW interaction.

Further calculations have revealed that the dissociation of water molecules adsorbed on the $\lambda\text{-Ti}_3\text{O}_5$ surface is accompanied with the charge transfer effect. For the computational details, the Bader charges associated with the water adsorption and dissociation were calculated using the VASP code. All computation settings (*e.g.*, the cutoff energy for the plane waves, the PBEsol exchange-correlation functional, the Grimme's D3 method for the van der Waals correction, *etc.*) were kept consistent with the other calculations in Subsections S1.3 and S4.1. In order to obtain the all-electron densities including the core density and the self-consistent valence density, the “LAECHG=.TRUE.” tag was set in the INCAR file of the VASP code. A two-times finer FFT mesh than the default was used for achieving a better accuracy. The results were processed using the Bader charge analysis tools developed by the Henkelman group⁴⁶.

Figures S4.5a-c show the initial, transitional and final states associated with the dissociation of a single water molecule (Fig. 3f in the main text) adsorbed on the $\lambda\text{-Ti}_3\text{O}_5$ ($1\bar{1}0$) surface. At the initial state (IS), the water molecule is chemisorbed by binding its O2 atom with the surface exposed Ti2 atom. At the transitional state (TS), the H1 atom dissociates from the chemisorbed H_2O and moves close to the surface exposed O1 atom. At the final state (FS), the dissociated H1 atom binds with the surface exposed O1 atom to form a new OH group, and in the meanwhile, the OH group formed by the H2 and O2 atom binds with the surface exposed Ti2 atom. In order to track the charge transfer process during the water dissociation, the Bader charges of relevant atoms at the IS, TS, and FS states were computed, as shown in Fig. S4.5d. As compared to the noninteracting slab and H_2O molecule (*see* values in brackets of Fig. S4.5d), when the H_2O molecule is adsorbed, the surface Ti2 atom and the two H atoms of the H_2O molecule lose their valence electrons, while the O2 atom of the H_2O molecule obtains the electrons. Since the H_2O molecule is chemisorbed by binding its O2 atom with the surface Ti2 atom, the charge transfer from the surface exposed Ti2 atom to the O2 atom is expected. For the dissociation process from IS to TS to FS, the H1 atom first obtains the electrons from the surface Ti2 atom and the O2 atom of the H_2O molecule when moving from IS to TS, and then transfers the electrons to the surface O1 atom and Ti1 atom when further moving from TS to FS.

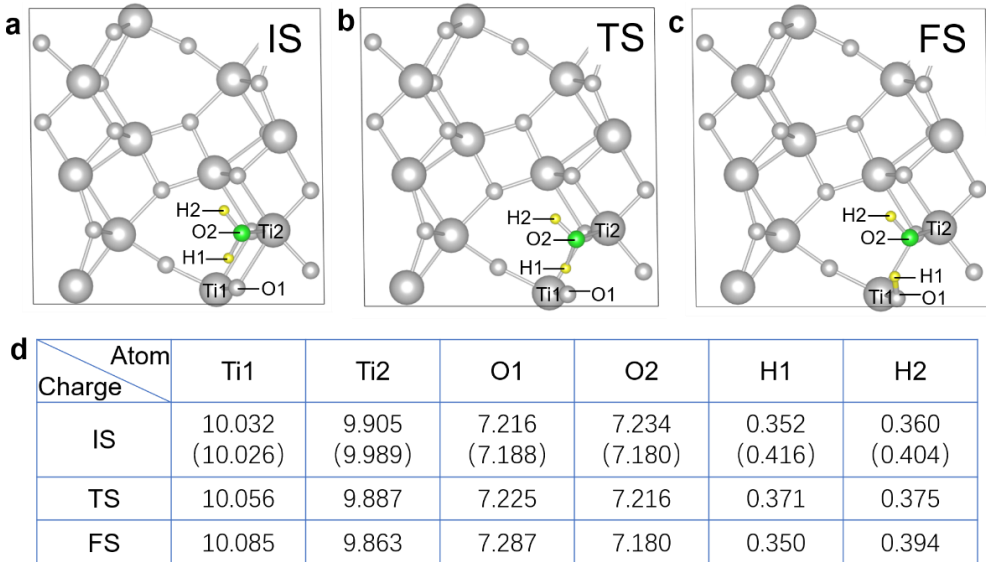


Figure S4.5. Bader charge analysis on relevant atoms for the adsorption and dissociation of one water molecule on the $\lambda\text{-Ti}_3\text{O}_5$ ($1\bar{1}0$) surface. IS, TS, and FS refer to the initial, transitional and final states, respectively. Note that the transitional path from IS to TS to FS was obtained by *ab initio* energy barrier calculations using the climbing image nudged elastic band method⁴⁷. The table in **d** shows the calculated Bader charges for the IS, TS, and FS configurations in **a**, **b** and **c**. The values in brackets denote the calculated Bader charges before the water molecule is adsorbed on the $\lambda\text{-Ti}_3\text{O}_5$ ($1\bar{1}0$) surface.

S4.3. Signals of Ti-O-H bending and stretching on $\lambda\text{-Ti}_3\text{O}_5$ surface

For a better understanding of the enhanced water evaporation by $\lambda\text{-Ti}_3\text{O}_5$, we have employed the attenuated total reflection Fourier transform infrared spectroscopy (ATR-FTIR, Thermo Scientific Nicolet iS10) to elucidate the status of water adsorption on the $\lambda\text{-Ti}_3\text{O}_5$ surface. First, the pre-dried $\lambda\text{-Ti}_3\text{O}_5$ powders were spread on a germanium crystal, and then wetted with a few drops of water, followed by an immediate irradiation under simulated solar light. The *in-situ* ATR-FTIR measurements were conducted at room temperature every two minutes, within the wavenumber range from 400 cm^{-1} to 4000 cm^{-1} .

Figure S4.6a presents the *in-situ* ATR-FTIR spectra of the as-prepared $\lambda\text{-Ti}_3\text{O}_5$ powder samples having different water contents. First, two main peaks can be observed for the wetted powders. One is located at an almost fixed wavenumber of 1643 cm^{-1} , and the other around a wavenumber of 3397 cm^{-1} . These two peaks essentially stem from the strong infrared absorbance of the $\delta(\text{H-O-H})$ bending and the O-H stretching, respectively, in accordance with the published results for the water physisorption on TiO_2 ⁴⁸. This provides a direct experimental evidence about the water physisorption on the $\lambda\text{-Ti}_3\text{O}_5$ surface, because the physisorbed water is represented by the main peaks at both 1640 cm^{-1} and 3400 cm^{-1} ^{49,50}. Second, as the water content of the wetted powders decreased with time due to the solar-driven evaporation, the main O-H stretching peak around 3397 cm^{-1} gradually shifted to the higher wavenumber of 3440 cm^{-1} , accompanying a decrease in the peak height. The decrease in the peak height is mainly because the physisorbed water molecules with weak adsorption energies were getting evaporated. The shifting of the peak position reflects an enhanced hydrogen-bond interaction with the $\lambda\text{-Ti}_3\text{O}_5$ surface as the physisorbed water was thinned due to the evaporation. In particular, a sudden change occurred at 10 min, *i.e.*, the two main peaks almost disappeared while some other peaks remained, indicating that the physisorbed water was nearly evaporated out. Third, three typical features can be easily identified from the remaining robust peaks: two peaks at 1102 cm^{-1} and 1265 cm^{-1} , three peaks

at 2858 cm^{-1} , 2930 cm^{-1} and 2960 cm^{-1} , and four peaks in the range from 3575 cm^{-1} to 3775 cm^{-1} . According to the literature, the two peaks at 1102 cm^{-1} and 1265 cm^{-1} were attributed to the Ti-O-H bending⁵¹, and the four peaks in the range from 3575 cm^{-1} to 3775 cm^{-1} were very close to the reported frequencies (3670 cm^{-1} and 3730 cm^{-1}) of the terminal OH groups from the chemically dissociated water molecules⁴⁸. This fact reveals that the chemisorbed water molecules also exist on the $\lambda\text{-Ti}_3\text{O}_5$ surface.

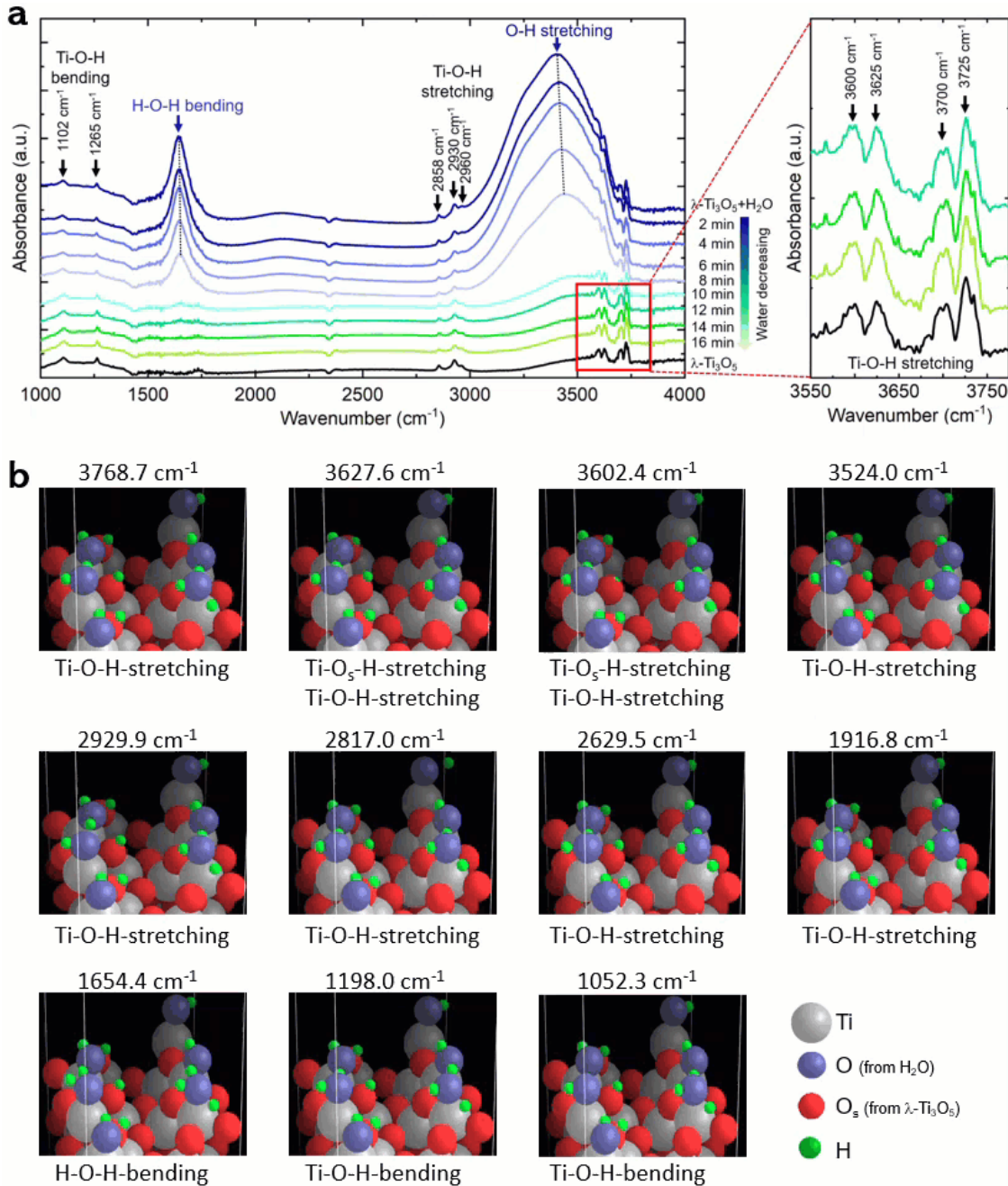


Figure S4.6. **a**, *In-situ* ATR-FTIR spectra of $\lambda\text{-Ti}_3\text{O}_5$ powder samples with addition of water drops. To prepare samples with different water contents, the wetted $\lambda\text{-Ti}_3\text{O}_5$ powders were exposed to solar irradiation. After every two minutes, the ATR-FTIR spectra were recorded at room temperature. **b**, Calculated vibrational modes and their corresponding vibrational frequencies for the Ti-O_s-H and Ti-O-H stretching as well as the Ti-O-H and H-O-H bending on the $\lambda\text{-Ti}_3\text{O}_5$ (110) surface. Note that these images are the animations, which are better visualized in Supplementary Video S1.

In order to resolve the specific signals from the measured ATR-FTIR spectra, we performed the first-principles calculations of phonon vibrational frequencies for the water chemisorption on the λ - Ti_3O_5 ($1\bar{1}0$) surface. In our calculations, we employed the energetically most stable configuration, namely, six water molecules chemisorbed on the ($1\bar{1}0$) surface to form the hydroxylated and hydrated surface, as shown in Fig. 3c of the main text. Table S4.2 summarizes the calculated phonon vibrational frequencies and vibrational modes for the considered six chemisorbed water molecules, in comparison with the experimental data.

Table S4.2. Calculated phonon vibrational frequencies for the energetically most stable configuration with three undissociated and three dissociated water molecules on the λ - Ti_3O_5 ($1\bar{1}0$) surface. Note that only vibrational frequencies over 1000 cm^{-1} are given. The typical vibrational modes are illustrated in Supplementary Video S1. The experimental data from the ATR-FTIR spectra are also provided.

No.	Group	Theory (cm^{-1})	Experiment (cm^{-1})	Vibrational mode
1	I	1038.2	1102	
2		1052.3		Ti-O-H bending
3		1103.1		(H-O-H rotation)
4		1198.0	1265	
5	II	1610.5		
6		1634.7	1682~1778	H-O-H bending
7		1654.4		
8	III	1916.8	-	Ti-O-H stretching
9		2629.5	2858	
10	IV	2817.0	2930	Ti-O-H stretching
11		2929.9	2960	
12	IV	3524.0	3600	Ti-O-H stretching
13		3587.2	3625	
14		3602.4		Ti-O-H stretching
15		3619.9		Ti-O _s -H stretching
16		3627.6	3700	
17		3746.0		
18		3765.2	3725	Ti-O-H stretching
19		3768.7		

The vibrational modes for the Ti-O_s-H and Ti-O-H stretching, as well as the Ti-O-H and H-O-H bending above 1000 cm^{-1} , are illustrated in Fig. S4.6b and Supplementary Video S1. Overall, our calculated results are in good agreement with the experimental data. The calculated vibrational frequencies can be classified into four groups (I, II, III and IV) according to their similar vibrational modes, as shown in Table S4.1. Group I contains the frequencies of 1038.2 cm^{-1} , 1052.3 cm^{-1} , 1103.1 cm^{-1} and 1198.0 cm^{-1} , which can be attributed

to the Ti-O-H bending with the H-O-H rotation, in correspondence to the experimental peaks at 1102 cm⁻¹ and 1265 cm⁻¹. Group II includes the frequencies of 1610.5 cm⁻¹, 1634.7 cm⁻¹ and 1654.4 cm⁻¹, which correspond to the H-O-H bending. Note that in the experimental ATR-FTIR spectra the H-O-H bending from the physisorbed water molecules has a strong and broad peak at ~1643 cm⁻¹, while some small peaks seem noticeable in the range of 1682 cm⁻¹~1778 cm⁻¹. We suspect that the theoretical frequencies of 1610.5 cm⁻¹, 1634.7 cm⁻¹ and 1654.4 cm⁻¹ might match these small peaks. Group III includes the frequencies of 2629.5 cm⁻¹, 2817.0 cm⁻¹ and 2929.9 cm⁻¹, which can be attributed to the Ti-O-H stretching, in resemblance to the experimental peaks at 2858 cm⁻¹, 2930 cm⁻¹ and 2960 cm⁻¹. Group IV includes the frequencies 3587.2 cm⁻¹, 3602.4 cm⁻¹, 3619.9 cm⁻¹ and 3627.6 cm⁻¹, which originate from the Ti-O-H stretching, in line with the experimental peaks at 3600 cm⁻¹, 3625 cm⁻¹, 3700 cm⁻¹ and 3725 cm⁻¹. Notably, the calculated vibrational frequencies in this group involve the photon vibrations not only from the Ti-O-H stretching, but also from the Ti-O_s-H stretching (*see* Supplementary Video S1).

It is mentioned that in our theoretical calculations, we captured a vibrational frequency at 1916.8 cm⁻¹, which comes from the O-H stretching of the chemisorbed water on the surface Ti atom (*see* Supplementary Video S1). However, no pronounced peak is observed in the experimental ATR-FTIR spectra. Instead, a broad shoulder around 2000 cm⁻¹ is evident from the experimental spectra recorded at 0 min, 2 min, 4min and 8 min (Fig. S4.6a) for the physisorbed water. This seems contradictory to our calculations for the chemisorbed water. Nevertheless, considering the complicated experimental conditions, some deviations of the predicted vibrational frequencies from the experimental values should be acceptable. To conclude, our experimental ATR-FTIR spectra combined with the calculated vibrational frequencies have confirmed the existence of Ti-O-H bonds and Ti-O_s-H bonds for the water chemisorption on the λ -Ti₃O₅ surface. Moreover, the ATR-FTIR spectra have demonstrated that the water molecules adsorbed on the λ -Ti₃O₅ surface belong to the chemisorbed ones, whereas the water molecules above the chemisorbed water molecules belong to the physisorbed ones.

S4.4. AIMD simulations of water molecule distributions on λ -Ti₃O₅ (1 $\bar{1}$ 0) surface

With the aim to uncover the dynamics of water molecule dissociation on the λ -Ti₃O₅ (1 $\bar{1}$ 0) surface, we have constructed an interfacial model (consisting of a five-layer λ -Ti₃O₅ slab and 49 water molecules with an 18 Å vacuum height) and performed long-term AIMD simulations. The thickness of 49 water molecules nearly matches that of the interfacial water layers above the surfaces of solid materials (~1 nm)⁵². The vdW interaction was treated *via* the Grimme's D3 method⁴⁵. The AIMD simulations were carried out at 300 K in a constant-volume ensemble (NVT) with a Nosé-Hoover chain thermostat. The energy cutoff for the plane waves was set to 520 eV, and only the Γ point was used. The time step was set to 1 fs and the simulations ran for 100 ps in a total of 100, 000 steps.

By inspecting the AIMD trajectories, we captured four distinct Regions I, II, III and IV above the clean (1 $\bar{1}$ 0) surface of λ -Ti₃O₅, as shown in Fig. 3h of the main text and described in more detail below.

(i) In Region I, the λ -Ti₃O₅ (1 $\bar{1}$ 0) surface is hydroxylated and hydrated by chemisorbing water molecules, in nice accordance with the above first-principles calculations. As displayed in Fig. 3c of the main text, the three undissociated water molecules chemically bond the terminations of three surface Ti atoms. The other three water molecules are dissociated into three OH groups and three H atoms, which chemically bond the surface exposed Ti atoms and O_s atoms, respectively. It needs to be emphasized that the clean (1 $\bar{1}$ 0) surface of λ -Ti₃O₅ is very active and it can be easily hydroxylated and hydrated.

(ii) In Region II, there exists an active hydrogen-bonded water layer with a typical thickness of about 3 Å (Fig. 3h of the main text) between the chemisorbed water molecules (Region I) and the bulk-like water (Region III). Within this water layer, water molecules often dissociate into OH groups and H atoms (Fig. S4.7a; *see* Supplementary Video S2), mainly due to the unsaturated surface OH or O_sH groups in Region I. Importantly, the physisorbed water molecule confined on the U-shaped groove can easily form one intermediate H₃O* unit by trapping an extra H atom from the neighborhood O_sH group (Figs. S4.8a-S4.8e). This H₃O* unit is metastable, exhibiting the fast transfer of H atom between surface O_sH group and intermediate H₃O* unit (*see* Subsection S4.5). In addition, the lengths of hydrogen bond surrounding the H₃O* unit are usually short, demonstrating strong hydrogen-bonded interaction. By statistically analyzing the continuous 40,000 AIMD trajectories, the occurrence probability of H₃O* units is as high as 22.6% above the hydroxylated and hydrated surface, revealing that this water layer is highly active.

(iii) In Region III, a bulk-like water layer with a thickness of 2~3 Å exists, in which the hydrogen-bond lengths between water molecules are usually in a range from 1.5 Å to 1.8 Å, but most of them lie in the range of 1.55~1.75 Å (Fig. 3h of the main text).

(iv) In Region IV (representing the top water layer with a thickness of about 8 Å), water molecules also frequently dissociate into OH groups and H atoms within the outermost water layer (Fig. S4.7; *see* Supplementary Video S2) within a thickness of about 3~4 Å next to the vacuum (Fig. 3h in the main text). A dissociated H atom usually forms the intermediate H₃O* unit with one of its neighboring water molecules (Figs. S4.8f-g). The occurrence probability of H₃O* units among the continuous 40,000 AIMD trajectories is 5.6% in the outermost water layer. Although this occurrence probability is lower than that in Region II, it is still very high. This fact reveals that the water molecules in Region IV are active, as well. Once the H₃O* units within the outermost water layer form, the hydrogen-bond lengths (1.2~1.7 Å) are relatively shorter around the H₃O* units, but the other hydrogen-bond lengths usually remain a wide range from 1.4 Å to 2.2 Å (Fig. 3h of the main text; Figs. S4.8f-h).

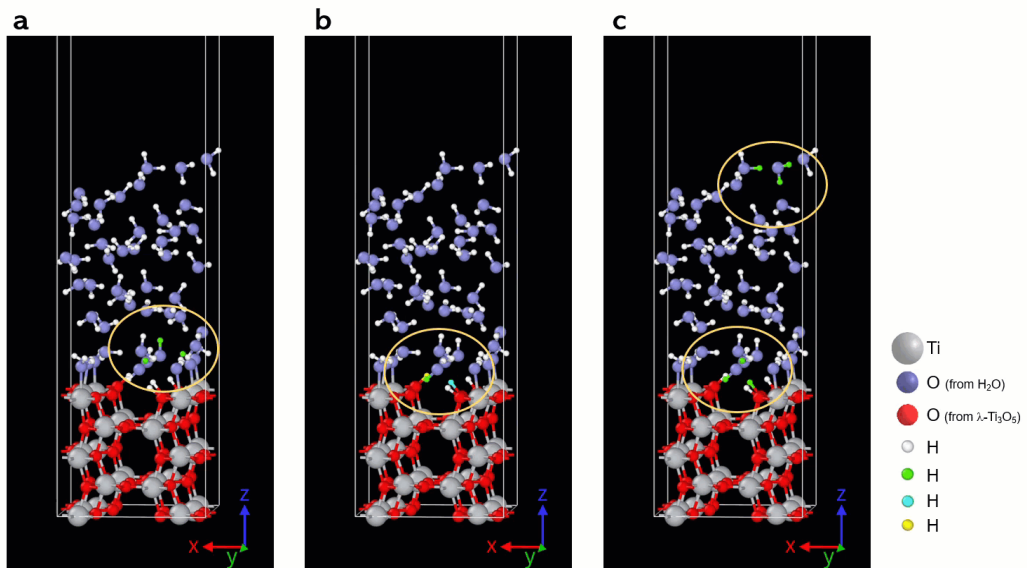


Figure S4.7. AIMD simulations of 49 water molecules adsorbed on the λ -Ti₃O₅ (1̄10) surface. **a**, Highlight for the water dissociation. **b**, Highlight for the frequent H transfer process appearing at the U-shaped groove. **c**, Highlight for the formation of H₃O* unit. Note that these images are the animations, which are better visualized in Supplementary Video S2.

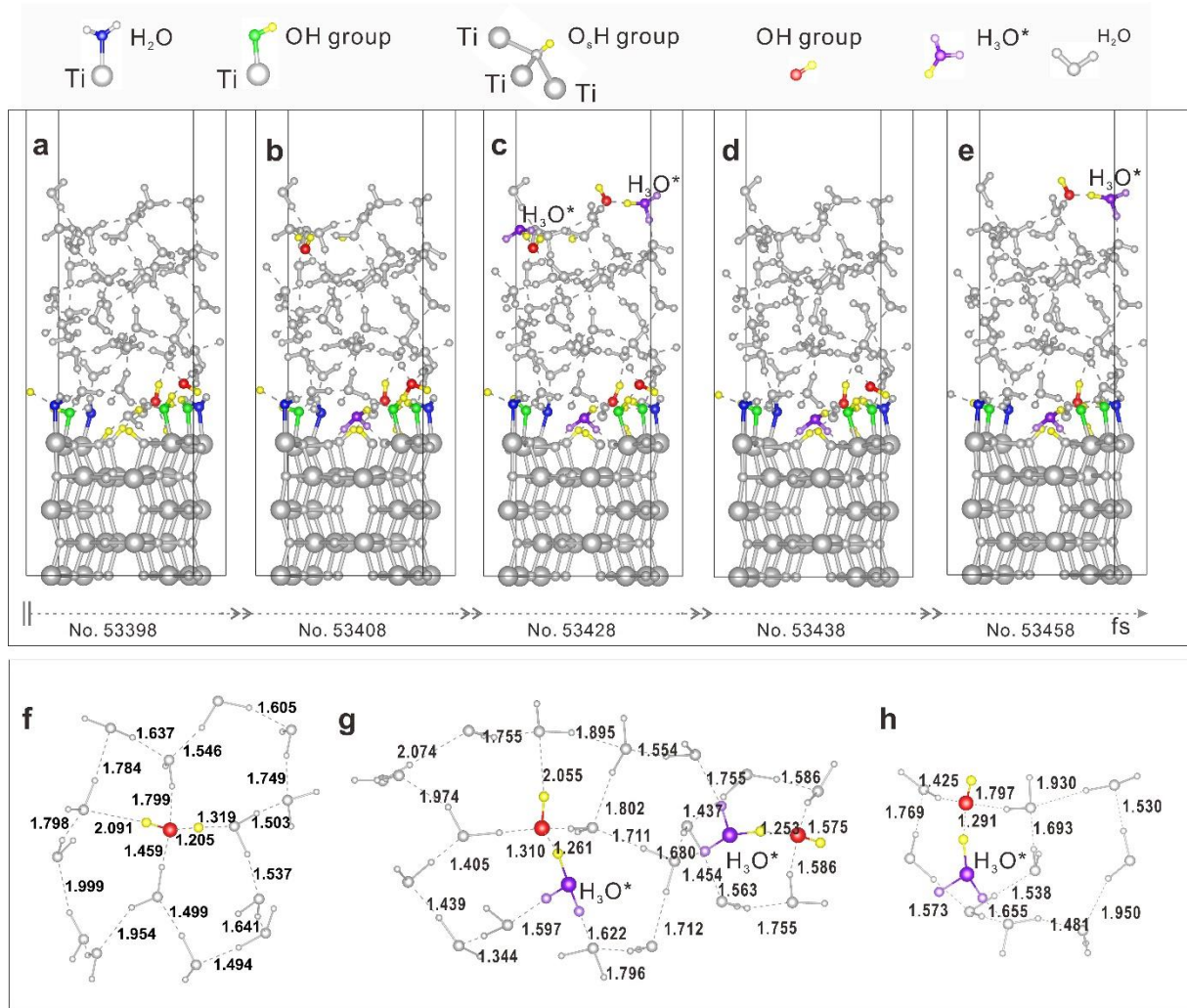


Figure S4.8. **a-e**, AIMD simulations of 49 water molecules adsorbed on the $\lambda\text{-Ti}_3\text{O}_5$ ($1\bar{1}0$) surface. Five snapshots are selected to show their time-dependent AIMD trajectories in the range from 53,398 fs to 53,498 fs. **f, g and h**, Zoom-in images of the top parts next to the vacuum of the panels **b**, **c** and **e**, respectively. The dotted lines indicate the hydrogen bonds (the number denotes to the length in the unit of Å).

S4.5. Transfer of H atom and formation of H_3O^* unit on $\lambda\text{-Ti}_3\text{O}_5$ ($1\bar{1}0$) surface

By examining the long-term (100 ps) AIMD trajectories, we have revealed that the H transfer process occurs as a recurring event. In particular, the intermediate H_3O^* unit represents the most frequent event by transferring H from the dissociated H atom of the surface hydroxyl ($\text{O}_{\text{s}}\text{H}$) on the hydroxylated and hydrated $\lambda\text{-Ti}_3\text{O}_5$ ($1\bar{1}0$) surface to the physisorbed water molecule above the U-shaped grooves. Herein, the H_3O^* unit was identified from the AIMD trajectories using a simple geometric criterion, *i.e.* all bond lengths between a centered O atom and its three nearest-neighbor H atoms are less than or equal to 1.2 Å. The same criterion was also adopted when analyzing the H atom transfer process. To determine the lifetime of the H_3O^* unit, we examined the AIMD trajectory with structure snapshots dumped every femtosecond and recorded the corresponding time steps when the H_3O^* unit emerges and vanishes. Eventually, we took the length of the time interval in which the H_3O^* unit survives as its lifetime. The histogram of the H_3O^* lifetime was plotted using a bandwidth of 10 fs. In the following, we summarize our key findings from the AIMD data.

(1) The occurrences of the intermediate H_3O^* units become the most frequent event among the 100 ps AIMD simulation. Our statistical analysis demonstrated that among the 100,000 AIMD steps the intermediate H_3O^* units occurred in 29,078 steps, implying a probability of as high as 29%. The lifetimes (LTs) of these H_3O^* units varied in a broad range from 2 fs to 426 fs, having a percentage of 40%, 42%, 7% and 6% in the time intervals of 0~10 fs, 10~20 fs, 20~30 fs and 30~50 fs, respectively (Fig. S4.9a). With and without the appearance of the H_3O^* units, the fluctuation of the total energy of the system behaves almost the same (*see* Fig. S4.9b).

(2) The physisorbed water molecule can easily dissociate above the saturated hydroxylated and hydrated $\lambda\text{-Ti}_3\text{O}_5$ ($1\bar{1}0$) surface. According to the 100 ps AIMD trajectories, the physisorbed water molecules frequently dissociate into OH groups and H atoms (Fig. S4.10c). A dissociated H atom usually binds with a surface O_s atom to form one surface O_sH group. Once this surface O_sH group forms, the two upper edges of a U-shaped groove would have four O_sH groups. Inevitably, the appearance of the four O_sH groups refers to a metastable state, because the chemisorption energy of the fourth O_sH group on the saturated hydroxylated and hydrated ($1\bar{1}0$) surface is 0.75 eV (Fig. S4.10a) and, furthermore, the energy required to dissociate an H atom is -0.28 eV by breaking one of the three surface O_sH groups (Fig. S4.10b). This fact reveals that three surface O_sH groups on the ($1\bar{1}0$) surface is the most favorable configuration.

(3) The alternating appearances of four surface O_sH groups and H_3O^* units result in the fast transfer of H atom. On the saturated hydroxylated and hydrated ($1\bar{1}0$) surface, the relaxation of intermediate H_3O^* units always returns water molecules and H atoms. More than 80% of the intermediate H_3O^* units exhibit a relatively short LT below 20 fs. The two kinds of metastable states (*i.e.*, four surface O_sH groups and intermediate H_3O^* units) alternatively occur, which drive the fast transfer of H atom between the O_sH groups and the H_3O^* units. Figure S4.11 presents the forth-and-back process for such a transfer. It typically consists of four basic steps.

(i) The first step refers to the dissociation of the hydrogen-bonding water molecules within the active physisorbed water layer in Region II. The dissociated OH group is hydrogen-bonded with its neighboring water molecules and the dissociated H atom binds with the surface O_s atom of $\lambda\text{-Ti}_3\text{O}_5$ to form the fourth O_sH group.

(ii) The second step is that one of the four O_sH groups becomes broken to deliver an H atom. The hydroxylated and hydrated ($1\bar{1}0$) surface approaches its most stable state again, while the dissociated H atom starts to look for its neighboring water molecule.

(iii) The third step is that this dissociated H atom binds with the neighboring hydrogen-bonded water molecule to form the metastable H_3O^* unit above the U-shaped groove.

(iv) The fourth step is that the metastable H_3O^* unit relaxes to a stable state with a certain LT, again dissociating a normal water molecule and an H atom. The dissociated H atom binds with the surface O_s atom to create the fourth O_sH group. With this occurrence, the state comes back to the first step.

(4) The fast transfer of an H atom between surface O_sH group and H_3O^* unit is accompanied with the charge transfer. When the H_3O^* unit appears, two features are relatively obvious. First, the charge of the O atom (O1 atom; upper panel in Fig. S4.12) in the H_3O^* unit seems to increase rapidly. Second, the transferred H atom (H2 atom; lower panel in Fig. S4.12) loses its charge apparently. It can be understandable that the transferred H2 atom contributes its electrons to the O1 atom. The only exception is in the time range from 54,419 fs to 54,427 fs, in which no H_3O^* unit appears. In this case, the O1 atom also exhibits a charge increase, but the H2 atom does not lose its electrons. The charge peak is mainly contributed by the H1 atom

(lower panel in Fig. S4.12).

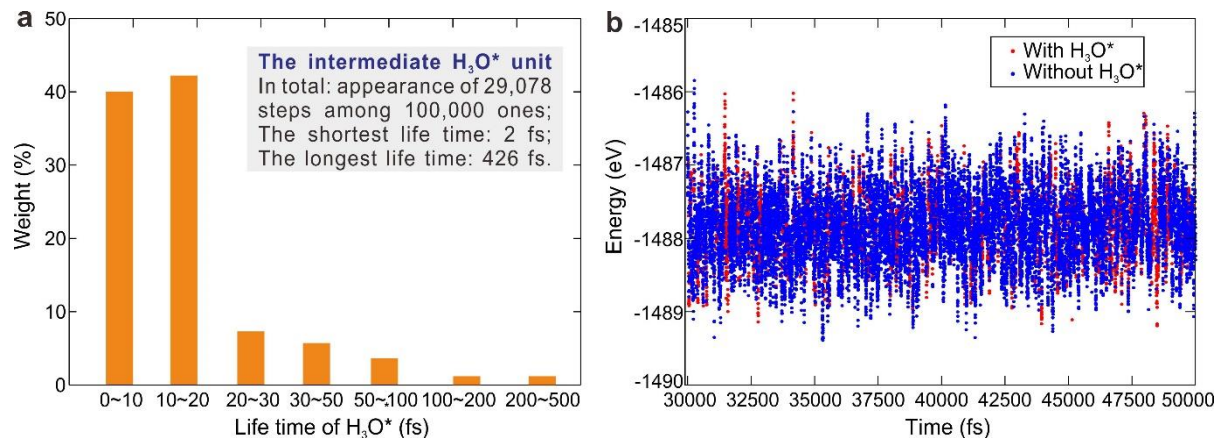


Figure S4.9. **a**, LT histogram of the H_3O^* units derived with the 100 ps AIMD simulation. **b**, Total energy variations at different time from 30,000 fs to 50,000 fs. The red and blue dots in **b** denote the appearance and disappearance of H_3O^* units, respectively.

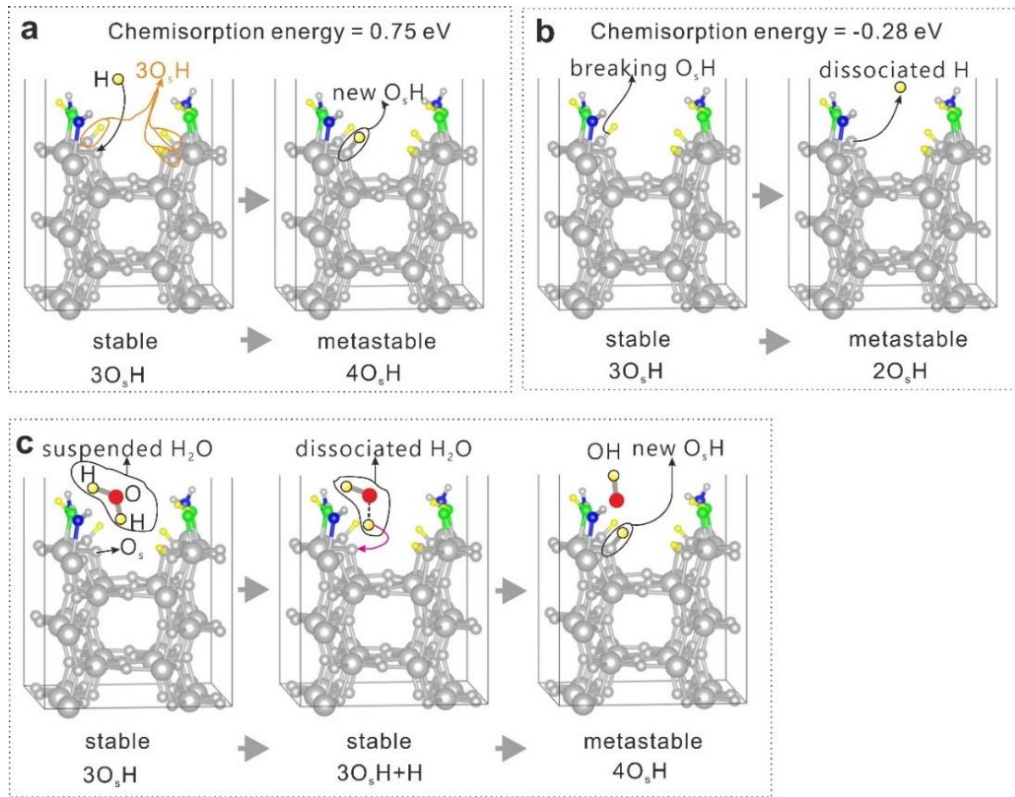


Figure S4.10. Water adsorption on the hydroxylated and hydrated $\lambda\text{-Ti}_3\text{O}_5$ ($1\bar{1}0$) surface interacting with external water molecules. **a**, Forming a new O_sH group by an external H atom. **b**, Breaking an O_sH group into a dissociated H atom. **c**, Sketch of a suspended water molecule (left), the dissociation of this suspended water molecules into an OH group and a dissociated H atom (middle), and the formation of a new surface O_sH group by the dissociated H atom (right).

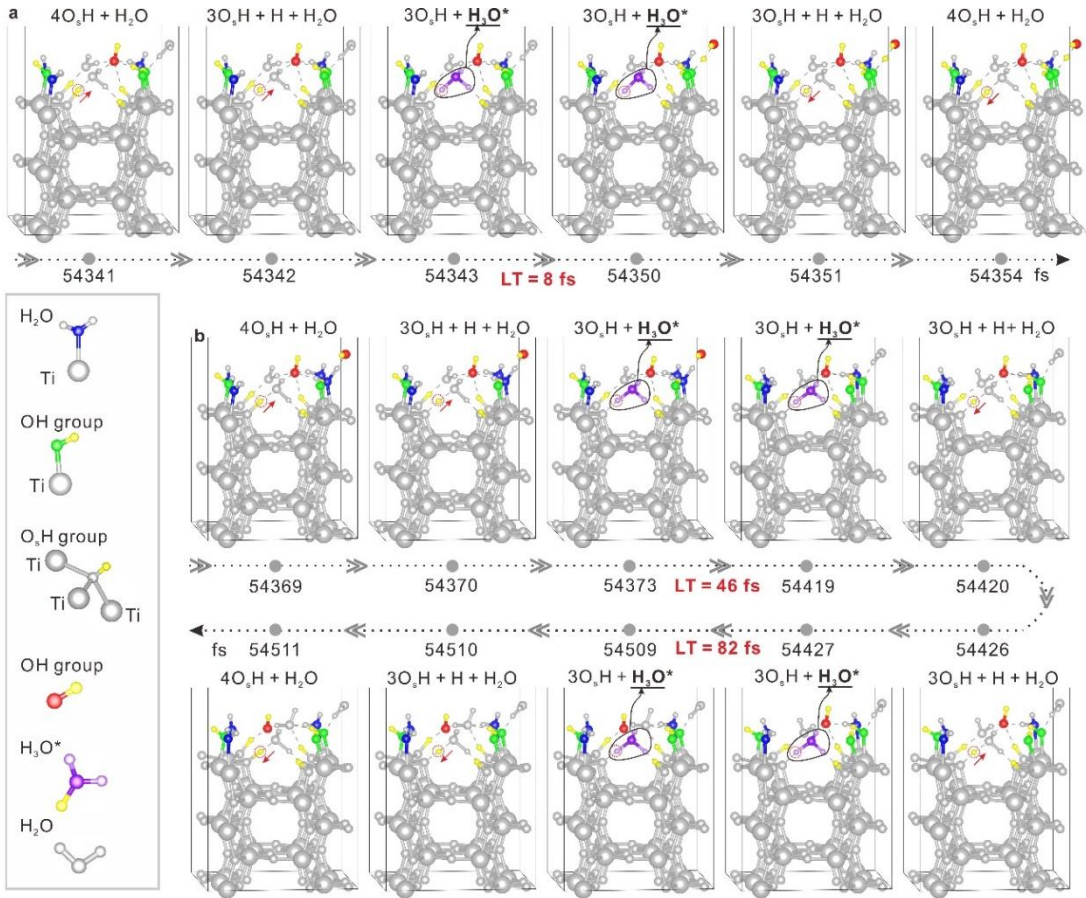


Figure S4.11. Forth-and-back transitions of the H_3O^* unit in the active water layer above the hydroxylated and hydrated $(1\bar{1}0)$ surface. The two processes of **a** (54,341~54,354 fs) and **b** (54,369 fs~54,511 fs) are selected from the AIMD trajectories to illustrate the whole forth-and-back transitions of H_3O^* when a water molecule is confined on the U-shape groove.

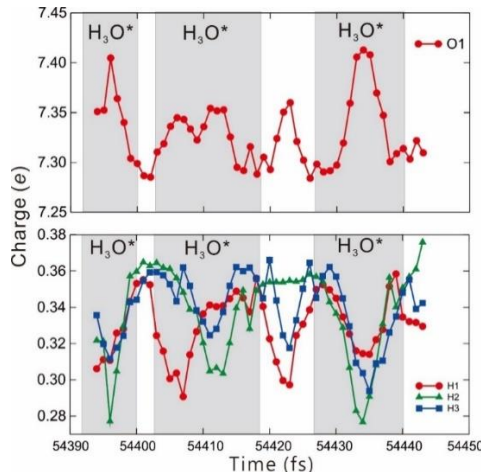


Figure S4.12. Calculated Bader charges of atoms in intermediate H_3O^* units, formed in the active water layer and confined above the U-shape groove of the hydroxylated and hydrated $(1\bar{1}0)$ surface of $\lambda\text{-Ti}_3\text{O}_5$. The gray background shows the appearance of H_3O^* units in different time ranges. The symbol O1 denotes the O atom in the H_3O^* units or the O atom of the targeted H_2O molecule before the H_3O^* formation. The symbol H2 denotes the transferring H atom between the surface O_3H group and the H_3O^* unit, and the symbols H1 and H3 denote the H atoms of the targeted H_2O molecule before the H_3O^* formation.

S4.6. Calculated hydrogen bond lengths and binding energies for different water molecules clusters

To investigate the binding interactions associated with the H transfer, we have calculated the lengths of hydrogen bonds within different kinds of water clusters (or protonated water clusters), as well as the binding energies between a water cluster and a neighborhood water molecule. Four kinds of stable clusters, including $C(H_2O)_3$, $C(H_2O)_4$, $C[(H_2O)_3+H]$ and $C[(H_2O)_4+H]$, were selected as reported in the literature⁵³⁻⁵⁵. The symbols $C(H_2O)_n$ and $C[(H_2O)_n+H]$ ($n=3, 4$) denote a cluster consisting of n water molecules without and with an H atom, respectively. The structure optimizations on these clusters were made taking into account of the vdW interaction. As shown in Fig. S4.13, the optimized $C(H_2O)_n$ and $C[(H_2O)_n+H]$ agree well with the previously reported ones⁵³⁻⁵⁵. The lengths of hydrogen bonds are 1.729 Å, 1.733 Å and 1.747 Å in $C(H_2O)_3$ (Fig. S4.13b), and 1.591 Å, 1.595 Å, 1.606 Å and 1.607 Å in $C(H_2O)_4$ (Fig. S4.13c), whereas they are 1.363 Å and 1.374 Å in $C[(H_2O)_3+H]$ (Fig. S4.13e), and 1.289 Å, 1.401 Å, 1.665 Å and 1.712 Å in the $C[(H_2O)_4+H]$ (Fig. S4.13f). Interestingly, the lengths of hydrogen bonds are significantly shortened around the H_3O^* unit. It implies that once an H atom is incorporated into one water cluster, the overall binding interactions within the cluster are strengthened. This is mainly because the extra proton can make the H_3O^* unit positively charged and trigger charge redistribution over the cluster. As a result, it enhances the hydrogen-bonding interactions between the H_3O^* unit and its neighboring water molecules, and hence shortens the lengths of hydrogen bonds around the H_3O^* unit.

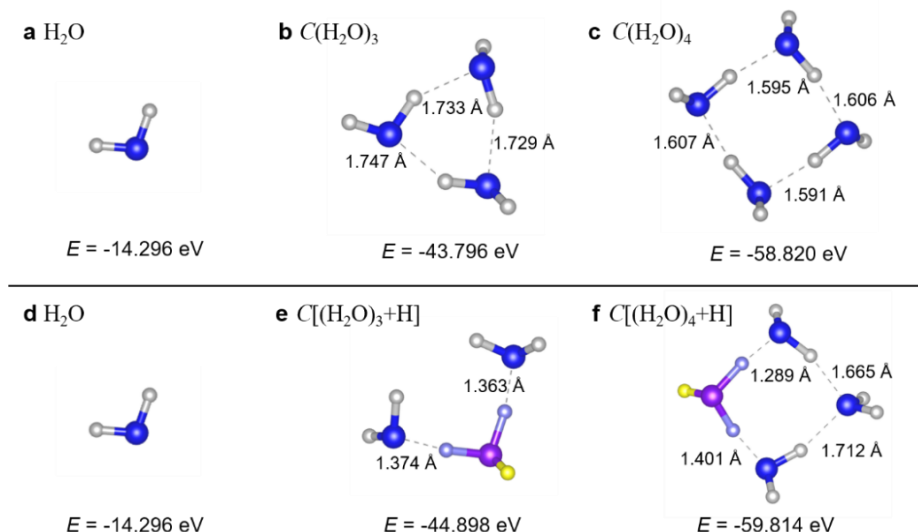


Figure S4.13, Optimized structures and calculated total energies of stable water clusters. **a** and **d**, H_2O . **b**, $C(H_2O)_3$. **c**, $C(H_2O)_4$. **e**, $C[(H_2O)_3+H]$. **f**, $C[(H_2O)_4+H]$. E denotes the total energy calculated by first-principles calculations. The introduced proton is colored in yellow.

For details, the hydrogen-bonding energy between the $C(H_2O)_3$ and a neighboring water molecule was calculated as follows,

$$E^b[C(H_2O)_3/H_2O] = E[C(H_2O)_4] - E[C(H_2O)_3] - E(H_2O) = -0.728 \text{ eV}, \quad (33)$$

where $E[C(H_2O)_4]$, $E[C(H_2O)_3]$ and $E(H_2O)$ are the calculated total energies of their equilibrium structures for $C(H_2O)_4$, $C(H_2O)_3$ and a water molecule, respectively. Similarly, the hydrogen-bonding energy between the protonated $C[(H_2O)_3+H]$ and a neighboring water molecule was calculated as follows,

$$E^b[C[(H_2O)_3+H]/H_2O] = E[C[(H_2O)_4+H]] - E[C[(H_2O)_3+H]] - E(H_2O) = -0.620 \text{ eV}, \quad (34)$$

where $E\{C[(H_2O)_4+H]\}$, $E\{C[(H_2O)_3+H]\}$ and $E(H_2O)$ are the calculated total energies of their equilibrium structures for $C[(H_2O)_4+H]$, $C[(H_2O)_3+H]$ and a water molecule, respectively. It demonstrates that once a proton is introduced, the hydrogen-bonding interaction between the protonated cluster and its surrounding water molecule is weakened.

S4.7. Evidence on the λ - Ti_3O_5 assisted water evaporation in the form of small clusters

To show the enhanced formation of water clusters on the λ - Ti_3O_5 surface, we have measured and analyzed the Raman spectrum of the interfacial water on the 2D λ - Ti_3O_5 evaporator, following the method described in Refs. 42, 44 and 56. Herein, a 2D λ - Ti_3O_5 evaporator (30 mm in diameter and $\sim 100 \mu m$ in height) was fabricated by dispersing the as-prepared λ - Ti_3O_5 powders onto a cellulose membrane through vacuum suction filtration. It was then padded with absorbent cotton (for water supply) and placed inside a glass dish containing liquid water (*see* the inset in Fig. S4.14b). In our experimental setup, the glass dish was directly put on the sample table of the Raman instrument (iHR 550, Horiba Jobin Yvon). The excitation light with a wavelength of 532 nm was focused on the top surface of the 2D λ - Ti_3O_5 evaporator, and the Raman spectrum was recorded at ambient temperature in the wavenumber range of $2850\text{--}3650 \text{ cm}^{-1}$. For comparison, the Raman spectrum of bulk water was also measured under the same conditions.

Figures S4.14a and b present the measured and fitted Raman spectra for interfacial water adsorbed on the 2D λ - Ti_3O_5 evaporator and bulk water, respectively. According to the literature^{44,56}, the collected Raman spectra cover all vibration information of O-H bonds from four hydrogen-bonded liquid H₂O (Peak 1 and Peak 2), H₂O clusters (Peak 3), and isolated H₂O molecules (Peak 4). For the case of bulk water (Fig. S4.14a), the area fraction of Peak 3 is around 16.0%, in fairly good agreement with the reported one (around 14.3%)⁴⁴. As for the case of interfacial water adsorbed on the 2D λ - Ti_3O_5 evaporator (Fig. S4.14b), the area fraction of Peak 3 is about 24.1%, which is obviously larger than that (16.0%) of bulk water. This demonstrates that λ - Ti_3O_5 can facilitate the formation of water clusters, in consistent with our AIMD simulation results.

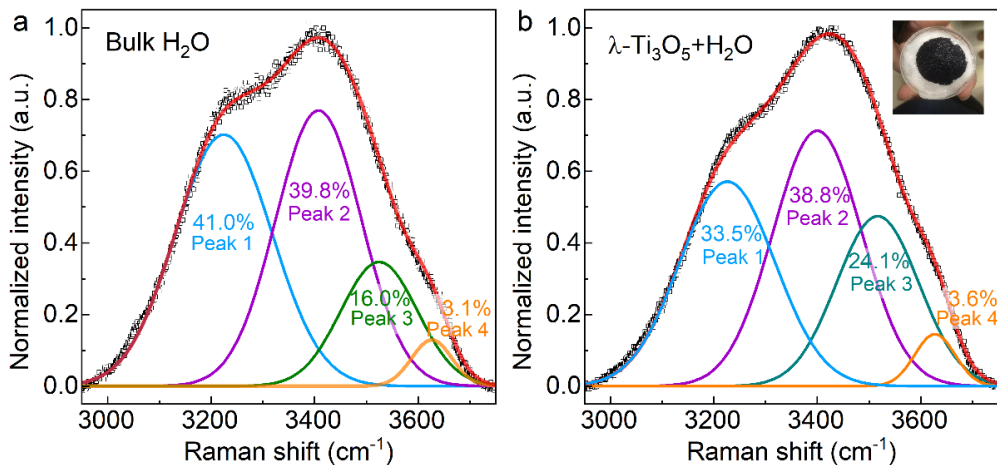


Figure S4.14, Raman spectra of bulk water and interfacial water on 2D λ - Ti_3O_5 evaporator in the energy range of O-H stretching modes. **a**, Bulk water. **b**, interfacial water on 2D λ - Ti_3O_5 evaporator. The inset in **b** shows the photograph of a 2D λ - Ti_3O_5 evaporator (placed inside a glass dish containing liquid water).

Furthermore, we have carried out a special indoor water collection experiment to evidence the enhanced water evaporation in the form of clusters by λ - Ti_3O_5 . This was done by tracing the concentrations of Li⁺ ions in the condenser, following a procedure detailed by Yu and his coworkers⁴². According to the literature⁵⁷⁻⁵⁹,

the nonvolatile electrolyte LiCl can be loaded by water clusters. During the solar vapor generation, the Li⁺ ions would be carried to the condenser if the water evaporation proceeds in the form of clusters⁴². In this connection, the concentration of Li⁺ ions in the evaporated water would reflect the degree of water evaporation in the form of clusters assisted by λ -Ti₃O₅.

In the present experimental setup, a water solution with the concentration of 100 g/L LiCl was prepared. The light-absorbing λ -Ti₃O₅ powders were directly and evenly spread in a glassware (served as a 2D λ -Ti₃O₅ evaporator), to avoid the interference of absorbent cotton and cellulose membrane (used in our routine 2D λ -Ti₃O₅ evaporator) to the Li⁺ movement. The prepared LiCl solution was slowly pumped into the glassware using an electronic constant flow pump (HL-2B, HUXI Analysis Instrument), to maintain the content of interfacial water on the surfaces of λ -Ti₃O₅ powders upon one sun irradiation. The evaporated vapor was condensed into liquid water and continually collected. For comparison, the indoor water collection was also made on the direct evaporation of the LiCl solution under one sun irradiation. For both cases, the residual Li⁺ concentrations in the condensed water were tested by inductively coupled plasma mass spectrometry (iCAP7400, ThermoFisher). Results show that the concentrations of Li⁺ ion in the condensed water are approximately 49.5 mg/L by use of the 2D λ -Ti₃O₅ evaporator, and 2.3 mg/L without use of the 2D λ -Ti₃O₅ evaporator (*i.e.*, by the direct evaporation of the LiCl solution). Notably, the λ -Ti₃O₅ assisted interfacial water evaporation has yielded a much higher Li⁺ concentration than the bulk water evaporation. This result has confirmed that the λ -Ti₃O₅ powders can facilitate interfacial water evaporation in the form of small clusters, which is also in agreement with the above Raman spectral analysis.

In summary, both the Raman results and the measured concentration of Li⁺ ion in the evaporated water evidence that λ -Ti₃O₅ facilitates water evaporation in the form of small clusters. When water evaporation proceeds in the form of clusters, it would require less energy as some hydrogen bonds do not need to be broken for evaporation. This would be the reason for the reduced water vaporization enthalpy, as detected on the interfacial water evaporation utilizing λ -Ti₃O₅.

Section 5. Performances of three-dimensional (3D) evaporator system

S5.1. Experimental setup of 3D solar steam evaporator system

The experimental setup for the 3D solar steam evaporator (3D-SSE) system is almost the same as that of the 2D-SSE system, except that 2D evaporators are replaced by 3D evaporators, as schematically shown in Fig. S5.1. Individual cylindrical 3D-SSEs with a diameter of 15 mm and different heights were fabricated with hierarchical-porous PVA hydrogels using various TSOs as light absorbers. One low-density PE foam sheet with a punched hole in the center was used as a holder to keep the cylindrical evaporator upward with no inclination. To reduce the thermal losses by convection and radiation as well as the solar energy loss by reflection, a conical cavity was further introduced at the top of 3D-SSEs for the structure optimization. Meanwhile, a little cotton was added into the PVA hydrogels to enhance the ability of water supply. The integrated 3D-SSE system was floating on bulk water within a beaker (50 mL) and then subjected to solar irradiation. It should be noted that the hierarchical structure of porous PVA hydrogel with super-hydrophilicity provides rich channels for water transportation. During the water evaporation measurements, an aperture was added to ensure that the solar light only covers the top surface of the 3D-SSEs.

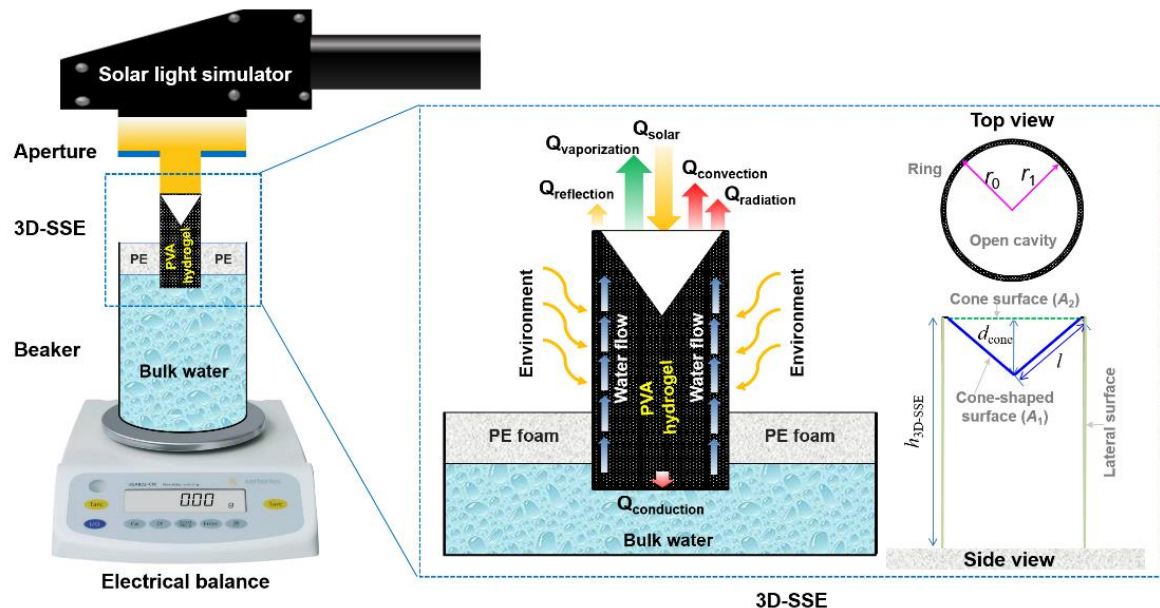


Figure S5.1. Diagrammatic sketch for measuring the solar evaporation performance of 3D-SSE in an open environment.

S5.2. Optimizations of cylinder-shaped 3D-SSEs

The microstructures of the hydrogels, prepared with PVA, λ -Ti₃O₅ particles and cotton, were examined with a field-emission scanning electron microscope (JEOL JEM7001F). They are typical of hierarchical pores from several microns to hundreds of microns, as shown in Figs. S5.2a and S5.2b. In addition, cotton fibers can be observed near the pores. According to the elemental mapping by energy dispersive spectrometer (EDS) on C and Ti elements (Figs. S5.2c and S5.2d), the λ -Ti₃O₅ particles are nearly uniformly distributed in the porous PVA-based hydrogels.

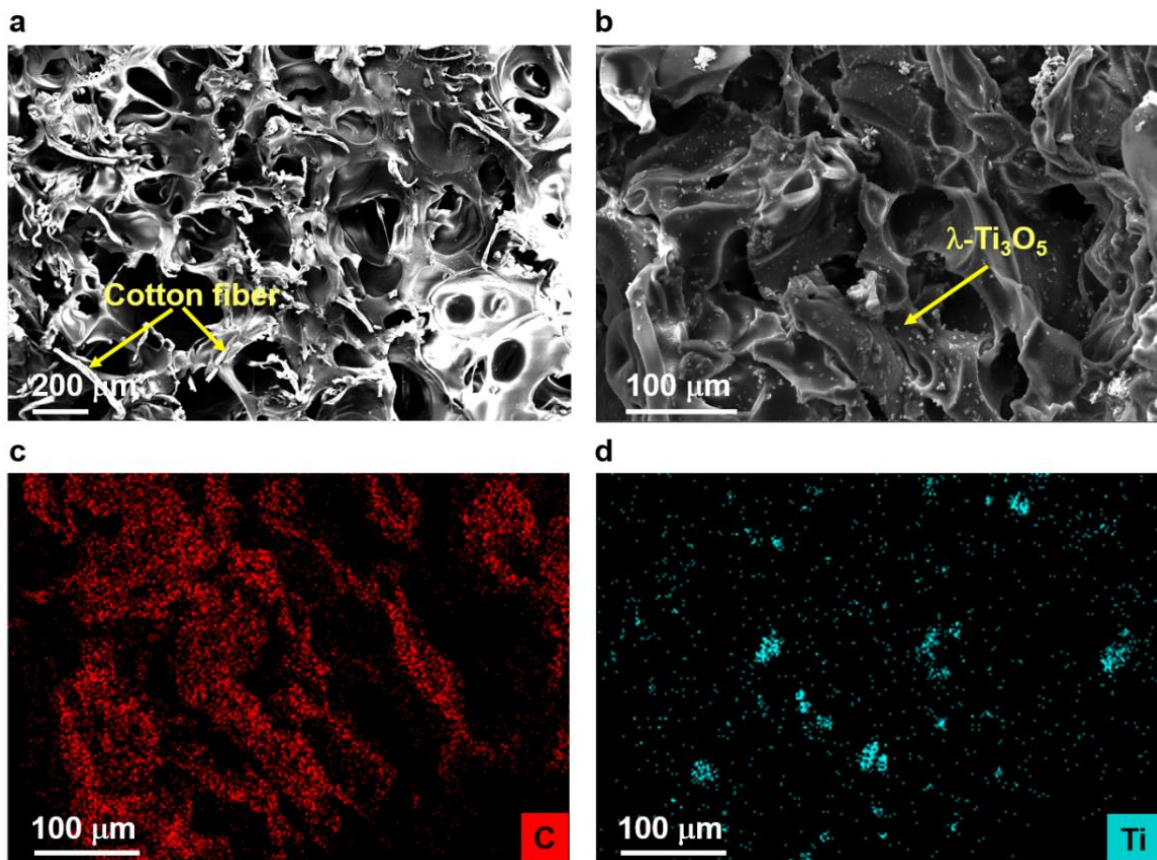


Figure S5.2. Morphologies and EDS maps of hydrogels prepared with PVA, λ -Ti₃O₅ particles and cotton. **a-b**, Secondary electron images. **c-d**, Spatial distributions of C and Ti elements.

In our first attempt, we designed a normal cylindrical 3D-SSE structure with the same diameter (15 mm) and effective height (7 mm) for water evaporation. For easy comparison, each 3D-SSE was made of hierarchical-porous PVA hydrogels with an addition of 6 wt.% TSO powders. For the light-absorbing TiO_x, C-Ti₂O₃, Ti₄O₇, β -Ti₃O₅ and λ -Ti₃O₅, the corresponding water evaporation rates were measured to be 1.14~1.26 kg m⁻² h⁻¹ under dark condition, and respectively 3.10±0.08 kg m⁻² h⁻¹, 3.35±0.04 kg m⁻² h⁻¹, 3.49±0.04 kg m⁻² h⁻¹, 3.61±0.12 kg m⁻² h⁻¹ and 4.04±0.03 kg m⁻² h⁻¹ under one sun irradiation (Fig. S5.3). Again, the 3D-SSE using λ -Ti₃O₅ powders exhibits the highest water evaporation rate. As for pure PVA hydrogels (without an addition of TSO powders), the water evaporation rates were measured to be 1.02±0.03 kg m⁻² h⁻¹ under dark condition and 2.48±0.02 kg m⁻² h⁻¹ under one sun irradiation. Note that our mean measured water evaporation rate for pure PVA hydrogels is comparable to the reported values in the literature, *e.g.* 2.3~2.56 kg m⁻² h⁻¹ under one sun irradiation for the cylindrical evaporators with thicknesses of 5~8 mm^{60,61}. In addition, our mean measured water evaporation rate of 3.35±0.04 kg m⁻² h⁻¹ for the light-absorbing C-Ti₂O₃ is in fairly good agreement with the reported value of 3.6 kg m⁻² h⁻¹⁶². The small deviation in the water evaporation rate can be attributed to the size effect of light absorber on solar absorption, since the particle size (100 mesh) of the commercial C-Ti₂O₃ powders used in the present study is larger than that (about 200 nm) refined *via* ball milling⁶². This further confirms the validity of our current measurements.

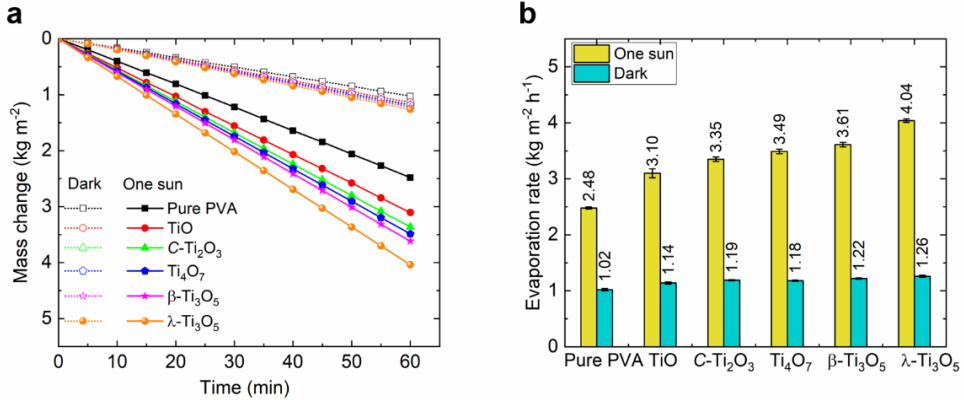


Figure S5.3. Water evaporation performances of normal cylindrical 3D-SSEs (15 mm in diameter and 7 mm in effective height) with or without an addition of 6 wt.% TSO powders to PVA hydrogels. **a**, Water mass change vs time. **b**, Mean measured water evaporation rates. The error bars are the standard deviations of the mean ($n = 3$, n is the number of evaporation rates for each sample used to derive statistics).

With the aim at elevating water evaporation rate, we have made a structural optimization on the normal cylindrical 3D-SSE with 6 wt.% λ -Ti₃O₅ powders. This was down by increasing the effective height of 3D-SSE to extend the surface area for water evaporation. Besides, a little cotton was mixed into the PVA-based hydrogels to improve the water supply. As shown in Fig. S5.4, with increasing the effective height from 7 mm to 30 mm, the water evaporation rate under one sun irradiation increased from $4.63 \pm 0.05 \text{ kg m}^{-2} \text{ h}^{-1}$ to $5.95 \pm 0.05 \text{ kg m}^{-2} \text{ h}^{-1}$. Although the highest water evaporation rate was achieved at the effective height of 30 mm, the salt precipitation occurred after one-hour solar illumination. Hence, we chose an effective height of 20 mm for the cylinder-shaped 3D-SSEs without salt precipitation during long-term water evaporation.

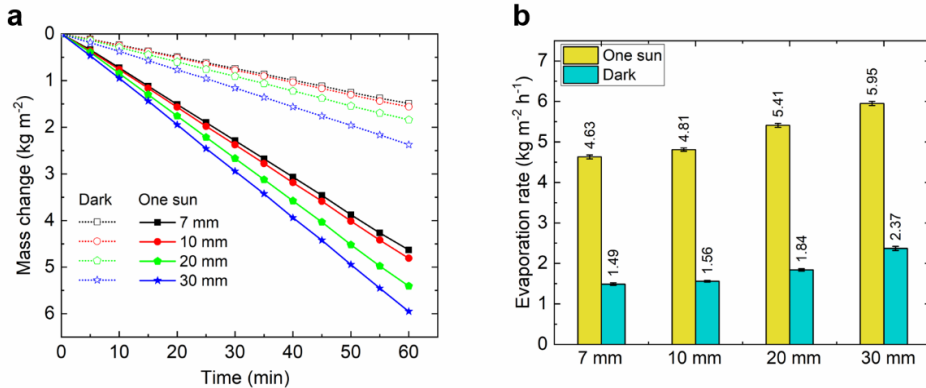


Figure S5.4. Effective height optimization of water evaporation performances for the normal cylindrical 3D-SSEs (15 mm in diameter) with an addition of 6 wt.% λ -Ti₃O₅ powders to PVA hydrogels. **a**, Water mass change vs time. **b**, Mean measured water evaporation rates. The error bars are the standard deviations of the mean ($n = 3$, n is the number of evaporation rates for each sample used to derive statistics).

By fixing the effective height (20 mm) for the cylindrical 3D-SSEs, we have further optimized the weight percentage of λ -Ti₃O₅ powders within PVA hydrogels and, in the meanwhile, added a conical cavity on the top of the 3D-SSEs. Actually, the introduction of a conical cavity can reduce the solar energy loss by reflection (through multiple reflections inside the conical cavity). More importantly, it allows the solar light to go deep into the 3D-SSEs for a better balance between solar evaporation and water supply. This leads to

a decrease in the temperature gradient and the surface temperatures of the 3D-SSEs, which are beneficial to lowering the thermal losses by conduction, convection and radiation. As shown in Fig. S5.5, with increasing the weight percentage of λ -Ti₃O₅ powders from 0 wt.% to 10 wt.%, the water evaporation rates were measured to be 1.69~1.78 kg m⁻² h⁻¹ under dark condition, and 3.30~6.09 kg m⁻² h⁻¹ under one sun irradiation. Note that our record value of 6.09 kg m⁻² h⁻¹ was achieved with the addition of 6 wt.% λ -Ti₃O₅ powders and a little cotton into PVA hydrogels, compared to 3.30 kg m⁻² h⁻¹ for pure PVA hydrogels. Thus, we used the 3D-SSEs with 6 wt.% λ -Ti₃O₅ powders and a little cotton for the indoor and outdoor water collection experiments.

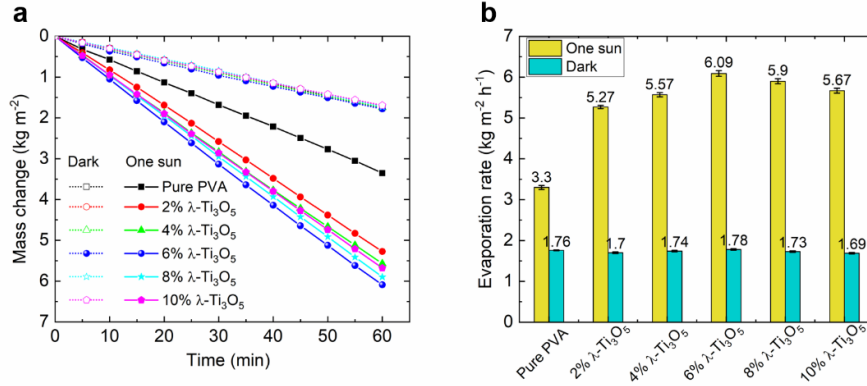


Figure S5.5. Weight percentage optimization of λ -Ti₃O₅ powders for the cylinder-shaped 3D-SSEs (15 mm in diameter and 20 mm in effective height) with a conical cavity (14 mm in diameter and 6 mm in depth). **a**, Water mass change *vs* time. **b**, Mean measured water evaporation rates. The error bars are the standard deviations of the mean ($n = 3$, n is the number of evaporation rates for each sample used to derive statistics).

S5.3. Estimation of solar-to-steam efficiency for 3D-SSE with a conical cavity

To calculate the solar-to-steam efficiency of cylinder-shaped evaporator with a conical cavity, we refer to our experimental measurements for the 3D-SSE system in an open environment, as illustrated in Fig. S5.1. The relevant parameters used in the present calculations are compiled in Table S5.1. Indeed, the computational methodology for the 3D-SSE system is similar to that for the 2D-SSE system, as detailed below.

Table S5.1. Parameters used for estimating the solar-to-steam efficiency of 3D-SSE with a conical cavity.

C_{opt}	1	d_{cone}	6 mm
p_0	1 kW m ⁻²	$A_{\text{3D-SSE}}^{\text{cross}}$	1.76715×10^{-4} m ²
t	1 h	$A_{\text{3D-SSE}}^{\text{lateral}}$	9.42478×10^{-4} m ²
$\varepsilon_{\text{3D-SSE}}$	0.97	$A_{\text{3D-SSE}}^{\text{ring}}$	2.27765×10^{-5} m ²
h	5 W m ⁻² K ⁻¹	$A_{\text{3D-SSE}}^{\text{cone}}$	1.53938×10^{-4} m ²
σ	5.68×10^{-8} W m ⁻² K ⁻⁴	$T_{\text{3D-SSE}}^{\text{lateral}}$	24.2 °C
$C_P^{\text{bulk water}}$	4.2×10^3 J kg ⁻¹ K ⁻¹	$T_{\text{3D-SSE}}^{\text{ring}}$	30.0 °C
R_0	3.59%	$T_{\text{3D-SSE}}^{\text{cone}}$	30.0 °C
r_0	7.5 mm	T_{enivr}	24.5 °C
r_1	7 mm	$T_{\text{bulk water}}^{\text{initial}}$	24.5 °C
$h_{\text{3D-SSE}}$	20 mm	$T_{\text{bulk water}}^{\text{end}}$	24.5 °C

Consider a cylindrical 3D-SSE having a conical cavity on the top. The cylindrical 3D-SSE has a radius r_0 and an effective height h_{3D-SSE} above the foamed PE, and the conical cavity has a radius r_1 and a depth d_{cone} . When solar light is incident on the surface of the 3D-SSE for a duration t , the total solar energy (Q_{solar}) and the solar energy loss by reflection ($Q_{reflection}$) read

$$Q_{solar} = C_{opt} p_0 A_{3D-SSE}^{cross} t \quad (35)$$

and

$$Q_{reflection} = \bar{R} Q_{solar}, \quad (36)$$

where A_{3D-SSE}^{cross} is the cross-sectional area at the bottom of the 3D-SSE, and \bar{R} is the overall solar reflectivity of the 3D-SSE with the conical cavity. Here, \bar{R} is calculated by

$$\bar{R} = [(\pi r_0^2 - \pi r_1^2) R_0 + \pi r_1^2 R_1]/(\pi r_0^2) = (1 - r_1^2/r_0^2) R_0 + (r_1^2/r_0^2) R_1, \quad (37)$$

where R_0 and R_1 are the mean solar reflectivities of the ring part and the conical cavity part of the 3D-SSE, respectively. For the 3D-SSE using λ -Ti₃O₅ particles as light absorbers, \bar{R} is considered to be negligibly small. This is mainly due to the fact that the mean measured solar absorptivity of the as-prepared λ -Ti₃O₅ powders is as high as 96.41%, and the overall light absorption performance of the 3D-SSE is further improved by the hierarchical-porous hydrogel structure (increasing surface area for light absorption) and the conical cavity (allowing multiple-reflection inside the cone). The mean solar reflectivity (R_0) of the ring part should be smaller than that (3.59%) of pure λ -Ti₃O₅ powders, since the 3D-SSE has a hierarchical-porous structure. As for the conical cavity part, the mean solar reflectivity (R_1) is set as zero, owing to the synergetic effect of the hierarchical-porous structure and the cavity induced multiple-reflections. This leads to a reduced \bar{R} value (~0.0046) according to Eq. (37), compared to that (3.59%) for the 2D-SSE.

In a steady state, the thermal losses by radiation, convection and conduction for the 3D-SSE within the duration t are evaluated using a general method described in the literature^{23,24}. The total radiative thermal loss to the surroundings, $Q_{radiation}$, is estimated as the sum of those from the lateral surface of the 3D-SSE ($Q_{radiation}^{lateral}$), the outer surface of the ring part ($Q_{radiation}^{ring}$) and the inner surface of the conical cavity part ($Q_{radiation}^{cone}$), *i.e.*,

$$Q_{radiation} = Q_{radiation}^{lateral} + Q_{radiation}^{ring} + Q_{radiation}^{cone} \quad (38)$$

with

$$Q_{radiation}^{lateral} = A_{3D-SSE}^{lateral} \varepsilon_{3D-SSE} \sigma (T_{3D-SSE}^{lateral 4} - T_{enivr}^{ 4}) t, \quad (39)$$

$$Q_{radiation}^{ring} = A_{3D-SSE}^{ring} \varepsilon_{3D-SSE} \sigma (T_{3D-SSE}^{ring 4} - T_{enivr}^{ 4}) t, \quad (40)$$

$$Q_{radiation}^{cone} = A_{3D-SSE}^{cone} \varepsilon_{3D-SSE} \sigma F_{12} (T_{3D-SSE}^{cone 4} - T_{enivr}^{ 4}) t. \quad (41)$$

Here, ε_{3D-SSE} is the emissivity of the 3D-SSE, $A_{3D-SSE}^{lateral}$ and A_{3D-SSE}^{ring} (A_{3D-SSE}^{cone}) are respectively the lateral surface area of the 3D-SSE and the cross-sectional area of the ring (cone) part at the top of the 3D-SSE, $T_{3D-SSE}^{lateral}$, T_{3D-SSE}^{ring} and T_{3D-SSE}^{cone} are respectively the temperatures of the lateral surface, the outer surface of the ring part and the inner surface of the cone part of the 3D-SSE, and T_{enivr} is the environment temperature.

The shape factor for the cone-shaped surface is given by⁶³, *i.e.*, $F_{12} = \frac{A_2}{A_1} = \pi r_1^2 / (\pi r_1 l) = r_1 / \sqrt{r_1^2 + d_{cone}^2}$.

The total convective heat loss to the surrounding air, $Q_{convection}$, is calculated as,

$$Q_{convection} = Q_{convection}^{lateral} + Q_{convection}^{ring} + Q_{convection}^{cone} \quad (42)$$

with

$$Q_{\text{convection}}^{\text{lateral}} = A_{\text{3D-SSE}}^{\text{lateral}} h (T_{\text{3D-SSE}}^{\text{lateral}} - T_{\text{envir}}) t, \quad (43)$$

$$Q_{\text{convection}}^{\text{ring}} = A_{\text{3D-SSE}}^{\text{ring}} h (T_{\text{3D-SSE}}^{\text{ring}} - T_{\text{envir}}) t, \quad (44)$$

$$Q_{\text{convection}}^{\text{cone}} = A_{\text{3D-SSE}}^{\text{cone}} h (T_{\text{3D-SSE}}^{\text{cone}} - T_{\text{envir}}) t. \quad (45)$$

The total conductive thermal loss to bulk water, $Q_{\text{conduction}}$, is estimated by

$$Q_{\text{conduction}} = C_p^{\text{bulk water}} m_{\text{bulk water}} (T_{\text{bulk water}}^{\text{initial}} - T_{\text{bulk water}}^{\text{end}}), \quad (46)$$

where $m_{\text{bulk water}}$ is the mass of bulk water in the beaker, and $T_{\text{bulk water}}^{\text{initial}}$ and $T_{\text{bulk water}}^{\text{end}}$ are the temperatures of bulk water in the beaker before and after solar irradiation for the duration t , respectively. Finally, the total loss (Q_{loss}) and the solar-to-steam efficiency ($\eta_{\text{solar_steam}}$) of the 3D-SSE are calculated as,

$$Q_{\text{loss}} = Q_{\text{reflection}} + Q_{\text{radiation}} + Q_{\text{convection}} + Q_{\text{conduction}}, \quad (47)$$

$$\eta_{\text{solar_steam}} = 1 - Q_{\text{loss}}/Q_{\text{solar}}. \quad (48)$$

By inserting the parameters (Table S6.1) into the above expressions, the solar-to-steam efficiency of the present 3D-SSE system was estimated to be as high as 95.92% upon one sun irradiation. This value is significantly higher than the solar-to-steam efficiency (68.3%) of the counterpart 2D-SSE system, and even larger than the photothermal conversion efficiency (92.4%) of the $\lambda\text{-Ti}_3\text{O}_5$ pill sample in a dry condition. The enhancement in the solar-to-steam efficiency can be attributed to two factors. First, by the introduction of a conical cavity and the hierarchical-porous structure into the 3D-SSE promotes solar absorption, it reduces the solar energy loss as suffered in both cases of the 2D-SSE and the $\lambda\text{-Ti}_3\text{O}_5$ pill sample. Second, the highly hydrophilic nature of the interconnected hierarchical-porous PVA mixed with cotton allows for a sufficient water supply and provides abundant surfaces and channels for water evaporation. This keeps the interfacial water evaporation at reasonable temperatures over a large volume and thus lower the thermal losses caused by conduction, convection and radiation. As shown in Fig. S5.6, the overall surface temperatures of the 3D-SSE in an open environment are rather low under dark and one sun irradiation, even lower than the ambient temperature. This indicates that such a 3D-SSE could absorb extra energy from the atmosphere.

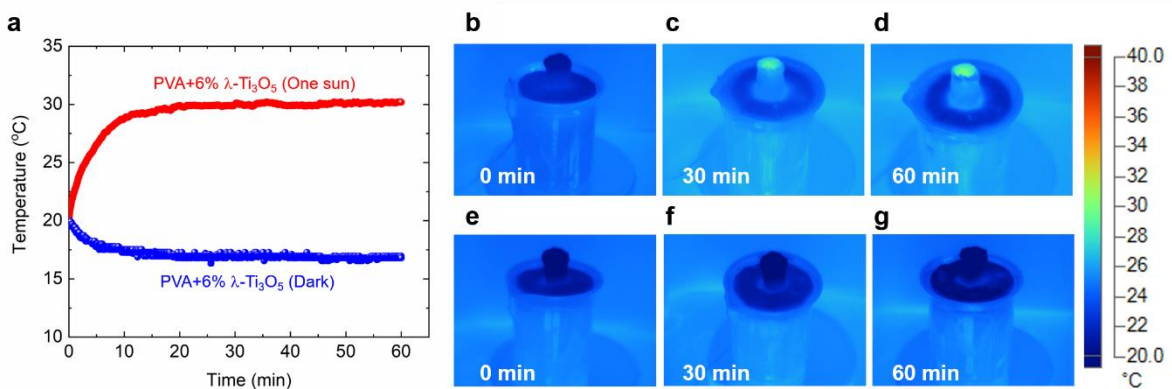


Figure S5.6. Surface temperature variations under dark and one sun irradiation for the 3D-SSE with a conical cavity. The 3D-SSE was made of hierarchical-porous PVA hydrogels with the addition of 6 wt.% $\lambda\text{-Ti}_3\text{O}_5$ powders and a little cotton. **b-d**, Infrared photographs at 0 min, 30 min, and 60 min under one sun irradiation. **e-g**, Infrared photographs at 0 min, 30 min, and 60 min under dark condition.

S5.4. Thermal stability and mechanical properties of 3D-SSEs with a conical cavity

To check the thermal stability and mechanical properties of the 3D-SSEs using 6 wt.% λ -Ti₃O₅ powders, we have performed a long-term (100 hours) solar-driven evaporation measurement on 3.5% saline water in an open environment. It can be seen from Fig. S5.7 that under one sun irradiation, the overall water evaporation performance keeps at a very high level with the average rate of about $5.96 \pm 0.08 \text{ kg m}^{-2} \text{ h}^{-1}$. This demonstrates that these 3D-SSEs can work steadily under solar irradiation for long time.

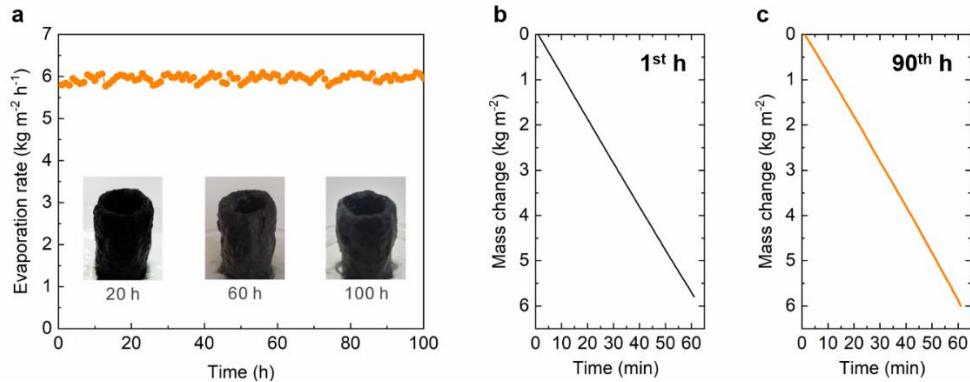


Figure S5.7. **a**, Evaporation rates of 3.5 wt.% saline water under one sun irradiation using the cylindrical 3D-SSE with a conical cavity. The insets present the photographs of the 3D-SSE tested for 20 h, 60 h and 100 h, showing no salt precipitation. **b-c**, Time-dependences of the evaporated water mass for the 1st hour and 90th hour evaporation, respectively.

Furthermore, we examined the mechanical properties of the 3D-SSEs before and after the long-term (100 hours) solar-driven evaporation measurement. Both the compression (Figs. S5.8 and S5.9) and bending (Fig. S5.10) tests demonstrated that they have excellent mechanical properties. No matter whether the compression or bending tests were performed, the 3D-SSEs recovered back to their initial states, even after the 100 h solar-driven evaporation. All these results have confirmed that the present 3D-SSEs exhibit not only promising water evaporation performances, but also good mechanical properties and thermal stability.

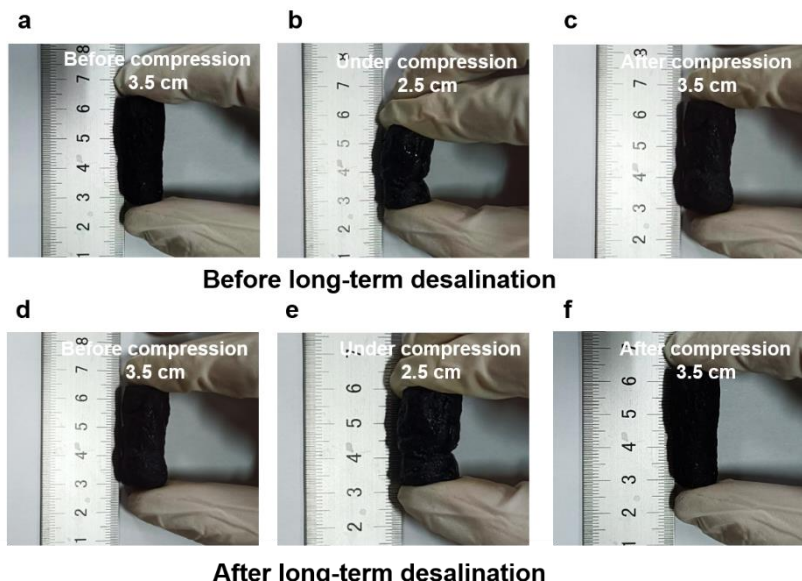


Figure S5.8, Compression tests on a cylindrical 3D-SSE along the length direction before and after 100 h solar-driven water evaporation. **a** and **d**, Initial states. **b** and **e**, Under compression. **c** and **f**, After compression.

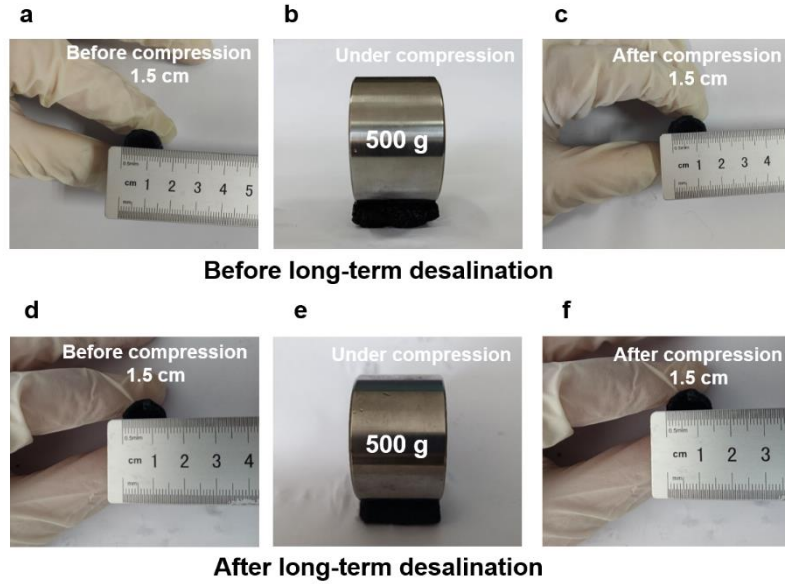


Figure S5.9, Compression tests on a cylindrical 3D-SSE along the transverse direction before and after 100 h solar-driven water evaporation. **a** and **d**, Initial states. **b** and **e**, Under compression. **c** and **f**, After compression.

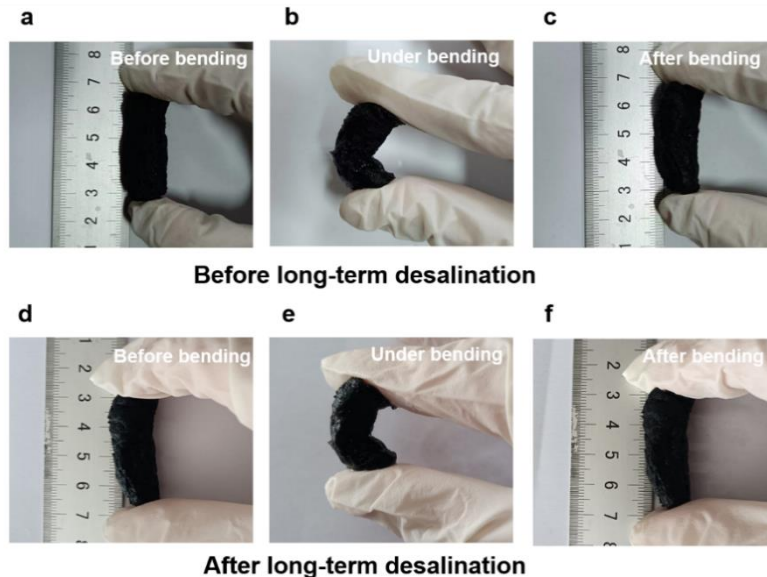


Figure S5.10, Bending tests on a cylindrical 3D-SSE before and after 100 h solar-driven water evaporation. **a** and **d**, Initial states. **b** and **e**, Under bending. **c** and **f**, After bending.

S5.5. Indoor and outdoor clean water collections with 3D-SSEs

First, we conducted the indoor water collection experiments with the present 3D-SSE system in a closed environment, as shown in Fig. S5.11. Individual 3D-SSEs with a conical cavity on the top were made of hierarchical-porous PVA-based hydrogels with 6 wt.% λ -Ti₃O₅ powders and a little cotton. Each 3D-SSE has a diameter of 15 mm and a height of 20 mm above the PE foam sheet (8 mm in thickness), and the conical cavity has a diameter of 14 mm and a depth of 6 mm. A group of sixteen 3D-SSEs were then evenly inserted into the PE foam sheet, floating on the simulated 3.5 wt.% saline water in a container (Fig. S5.11a). During the simulated solar irradiation (one sun), the evaporated vapor condensed into liquid water on the condenser

walls that were cooled by cooling water (added once without circulation). The purified water was continually collected into a 100 mL cylinder vessel *via* a transparent glass pipe. It can be seen from Fig. S5.11b that the average hourly collection rate of purified water monotonously increased from $0 \text{ kg m}^{-2} \text{ h}^{-1}$ to $3.19 \pm 0.04 \text{ kg m}^{-2} \text{ h}^{-1}$ for the first four hours, and then it remained constant during the subsequent six hours. In total, an amount of about 97 mL purified water after 10 hours was yielded (Fig. S5.11c). For comparison, we also performed the indoor water collection experiments on the direct evaporation of the 3.5 wt.% saline water by removal of the 3D-SSEs from the evaporation device. No purified water was collected upon one sun illumination in the first two hours and, after four hours, the average hourly collection rate of purified water kept almost a constant value (about $0.21 \pm 0.01 \text{ kg m}^{-2} \text{ h}^{-1}$), as shown in Fig. S5.11b. Accordingly, the hourly water collection rate of the present 3D-SSE system is about fifteen times that for bulk water (*i.e.*, without the 3D-SSEs) under the same indoor laboratory condition.

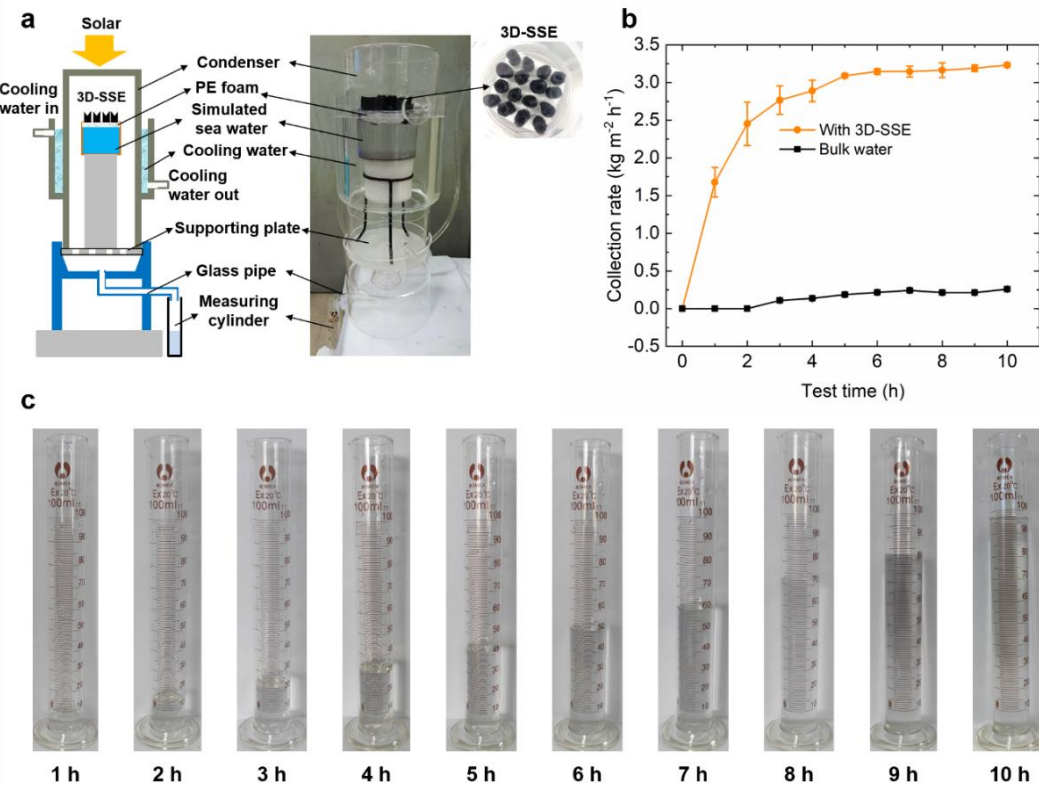


Figure S5.11. Indoor solar desalination performance of the cylindrical 3D-SSEs with a conical cavity under one sun irradiation. **a**, Schematic illustration and photograph of the solar water desalination system for salty water purification. **b**, Average hourly collection rates of purified water from 3.5 wt.% saline water under one sun irradiation with and without the 3D-SSEs. The error bars are the standard deviations of the mean ($n = 3$, n is the number of collection rates used to derive statistics). **c**, Photographs showing the collection yields of purified water in a measuring cylinder during 10 h.

To the best of our knowledge, the indoor water collection rate of the present 3D-SSEs (*i.e.*, made of hierarchical-porous PVA hydrogels plus 6 wt.% $\lambda\text{-Ti}_3\text{O}_5$ powders and a little cotton) is higher than those reported in literature. For instance, Guo and his coworkers prepared the normal cylindrical 3D-SSEs by mixing $C\text{-Ti}_2\text{O}_3$ powders into hierarchical-porous PVA hydrogels, and performed the indoor water collection experiments under the simulated sunlight irradiation in laboratory condition⁶². The hourly collection rates of purified water under one sun irradiation and water cooling condition were measured to be $\sim 1.3 \text{ kg m}^{-2} \text{ h}^{-1}$

without an assistance of air-flow, and $\sim 3.0 \text{ kg m}^{-2} \text{ h}^{-1}$ with an appropriate air flux of $\sim 40 \text{ mL min}^{-1}$, respectively. Apparently, the introduction of airflow as a carrier gas has played a vital role in reducing the relative humidity within the vapor generation chamber, thereby benefiting for the water evaporation from the 3D-SSEs. Nevertheless, our current indoor water collection experiment, conducted in a closed environment without recourse to air-flow, has achieved a record collection rate of purified water as high as $\sim 3.19 \text{ kg m}^{-2} \text{ h}^{-1}$. We believe that this record would be further upgraded, as long as the strategy of air-flow is incorporated into the structural design of 3D-SSEs for the vapor generation and condensation.

Besides, we performed the outdoor water collection experiments using the cylinder-shaped 3D-SSEs with a conical cavity under natural sun irradiation. The conceptual design for the solar water desalination system is shown in Fig. S5.12a. The solar water desalination system contains two major parts. One is the evaporation subsystem of the solar vapor generation using the 3D-SSEs, and the other is the condensation subsystem of generated vapors assisted with cooling water. Within the evaporation subsystem, a group of sixty-three 3D-SSEs were inserted into the PE foam, floating on the 3.5 wt.% saline water in a container. This container was supported by a platform with punched holes. Within the condensation subsystem, the temperature of the cooling water was controlled to be about 10°C . The outdoor water collection experiments were conducted on the campus of Northeastern University, Shenyang, China. The intensities of the natural sunlight shined on the roof (made of transparent quartz glass) of the evaporation device and the yields of the accumulated purified water were carefully traced during the day time from 07:30 to 17:30 (Fig. S5.12b). In the meanwhile, we recorded the time-dependent temperatures of the 3D-SSEs, the cooling water and the environment, as well as the humidities inside and outside the condenser (Fig. S5.12c). As shown in Fig. S5.12b, the sunlight flux (black curve) varied from $\sim 50 \text{ mW cm}^{-2}$ to $\sim 90 \text{ mW cm}^{-2}$ for a sunny summer day in Shenyang. The water collection rate (green curve) increased from $0 \text{ kg m}^{-2} \text{ h}^{-1}$ to $1.82 \text{ kg m}^{-2} \text{ h}^{-1}$ during the first one hour from 07:30 to 08:30, and reached the highest value of $2.82 \text{ kg m}^{-2} \text{ h}^{-1}$ at 12:30. In average, the hourly collection rate was $\sim 2.22 \text{ kg m}^{-2} \text{ h}^{-1}$ under natural sun irradiation with a mean solar flux of $\sim 78 \text{ mW m}^{-2}$ for the duration of 10 hours. This average hourly collection rate of purified water is much higher than the previously reported one, *e.g.*, $\sim 1.61 \text{ kg m}^{-2} \text{ h}^{-1}$ with a mean solar flux of $\sim 70 \text{ mW m}^{-2}$ for a duration of 12 hours from 08:00 to 20:00⁴². It is even higher than the known record value of $\sim 2.1 \text{ kg m}^{-2} \text{ h}^{-1}$ with a higher mean solar flux of $\sim 84 \text{ mW m}^{-2}$, achieved for a duration of 6 hours from 10:00 to 16:00, during which the solar flux was the strongest⁶⁴. If we choose the same duration of 6 hours (*e.g.*, from 09:30 to 15:30 in this work) with a comparable mean solar flux of $\sim 82 \text{ mW m}^{-2}$, our average hourly collection rate of purified water would be $\sim 2.55 \text{ kg m}^{-2} \text{ h}^{-1}$, compared to the known record of $\sim 2.1 \text{ kg m}^{-2} \text{ h}^{-1}$ ⁶⁴.

Using the same experimental setup, we collected the purified water on seven days with different weather conditions (Fig. S5.12d). Among them, three days were cloudy and four days were sunny. The average daily yields of purified water under natural solar irradiation for a duration of 10 hours are $\sim 14.3 \text{ L m}^{-2}$ for the three cloudy days with a mean solar flux of $\sim 47.0 \text{ mW m}^{-2}$, and $\sim 21.7 \text{ L m}^{-2}$ for the four sunny days with a mean solar flux of $\sim 75.7 \text{ mW m}^{-2}$, respectively. This averaged water purification rate for sunny days with a mean solar flux of $\sim 75.7 \text{ mW m}^{-2}$ is significantly higher than those reported data, *e.g.*, 12.44 L m^{-2} from 09:00 to 18:00 with a mean solar flux of $\sim 74.8 \text{ mW m}^{-2}$ ⁶⁵, 16.6 L m^{-2} from 07:30 to 17:00 with a mean solar flux of $\sim 75 \text{ mW m}^{-2}$ ⁶⁶, $\sim 15 \text{ L m}^{-2}$ from 08:00 to 20:00 with a mean solar flux of $\sim 58 \text{ mW m}^{-2}$ ⁶⁷, and 18 L m^{-2} from 08:00 to 20:00 with a mean solar flux of $\sim 70 \text{ mW m}^{-2}$ ⁴².

Furthermore, the quality of the desalinated water was measured by inductively coupled plasma spectroscopy (Hitachi Z2300 for Na^+ and K^+ ; PerkinElmer Avio500 for Mg^{2+} and Ca^{2+}). Compared to the

initial saline water, the salinity of the purified water was significantly decreased by approximately four orders of the magnitude, that is about two orders of the magnitude lower than the drinking water standards defined by the World Health Organization (WHO, 1‰) ⁶⁸. Before the desalination, the concentrations of four main ions Na^+ , K^+ , Mg^{2+} and Ca^{2+} were measured to be $10,447 \pm 851 \text{ mg L}^{-1}$, $473 \pm 21 \text{ mg L}^{-1}$, $590 \pm 60 \text{ mg L}^{-1}$ and $567 \pm 70 \text{ mg/L}$, respectively. After the desalination, they were dramatically decreased to $6.8 \pm 1.2 \text{ mg L}^{-1}$, $1.3 \pm 0.4 \text{ mg L}^{-1}$, $0.2 \pm 0.03 \text{ mg L}^{-1}$ and $4.5 \pm 0.78 \text{ mg L}^{-1}$, respectively. The concentration of Na^+ ions in the purified water is far below the drinkable water standard limit for Na^+ ($200 \sim 250 \text{ mg L}^{-1}$) defined by WHO⁶⁸. Note that there are no specific limits for K^+ , Mg^{2+} and Ca^{2+} in the WHO drinkable water standard, but they should be as low as possible.

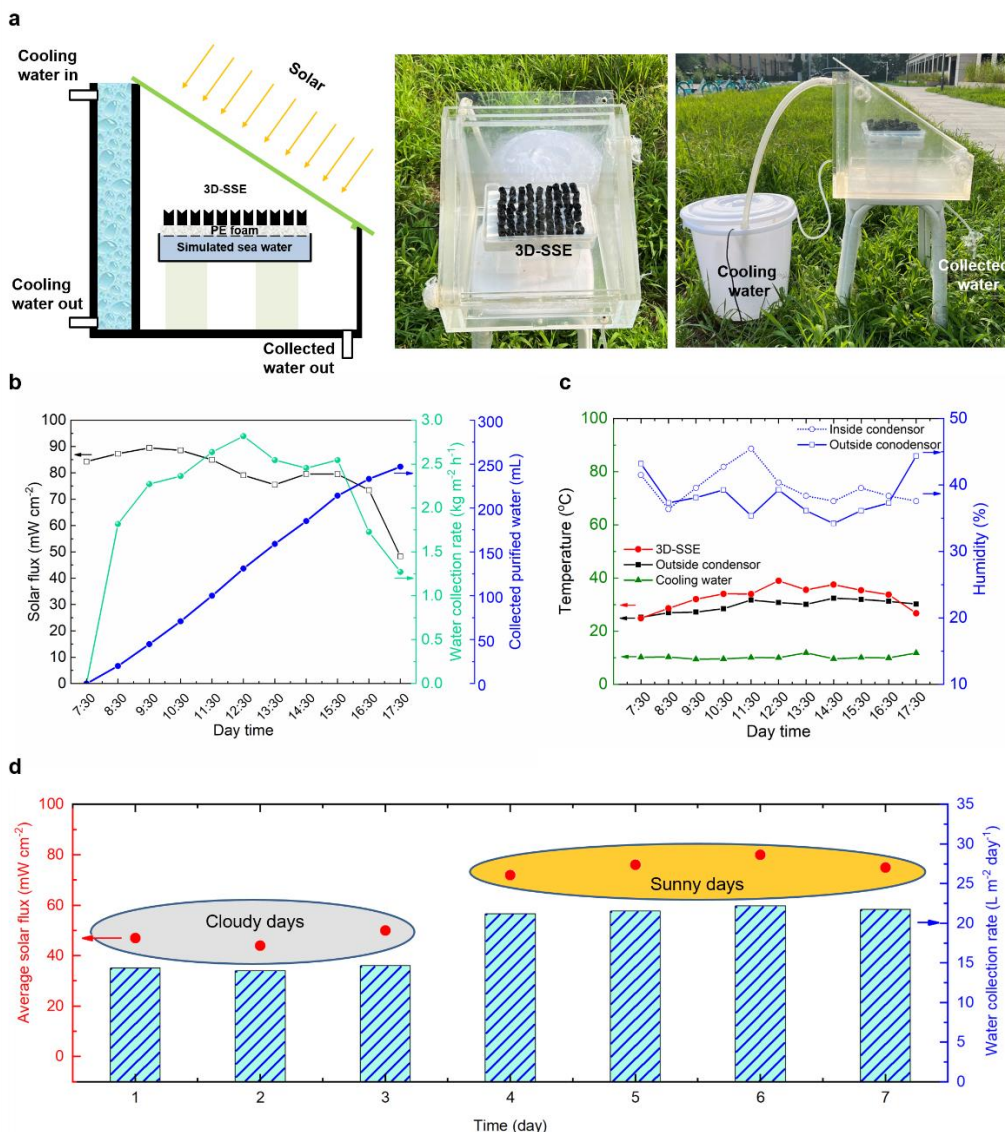


Figure S5.12. Outdoor desalination performance of cylindrical 3D-SSEs with a conical cavity under natural sunlight irradiation. **a**, Conceptual design and photographs of the solar water desalination system for salty water purification. **b**, Variations of the solar flux, water collection rate and yield of purified water with day time. **c**, Variations of the temperature and humidity (inside and outside the solar water desalination system) with day time. **d**, Average daily solar fluxes and water collection rates for a duration of 10 hours on three cloudy days and four sunny days.

Section 6. Comparisons of 2D- and 3D-SSEs with known ones

In order to evaluate the evaporation performances of the present 2D- and 3D-SSE systems, we have summarized the solar absorptivities, water evaporation rates, water vaporization enthalpies and solar-to-steam efficiencies of a series of known evaporators published in the literature in Table S6.1.

Table S6.1. A summary of dimensions, solar absorptivities, water evaporation rates, solar-to-steam efficiencies, and water vaporization enthalpies of a series of known evaporators under one sun irradiation in literature.

No.	Material	Dimension	Solar absorptivity (%)	Evaporation rate ($\text{kg m}^{-2} \text{h}^{-1}$)	Solar to steam efficiency (%)	Enthalpy (kJ kg^{-1})	Publication Year	Ref.
1	$\lambda\text{-Ti}_3\text{O}_5$	2D	96.41	1.64	68.3	1696		This work
	PVA- $\lambda\text{-Ti}_3\text{O}_5$ hydrogels with open cavity	3D	99.54	6.09	95.9			
2	Ti ₂ O ₃ nanoparticles	2D	92.5	1.32	92.1 \pm 3.2	Unknown	2017	⁶
3	Black TiO _x nanoparticles SS mesh	2D	91.3	0.8	50.3	Unknown	2017	⁶⁹
4	Al nanoparticles	2D	96	1.0	58	Unknown	2016	⁷⁰
5	Flexible thin-film black gold membranes	2D	91	0.67	42	Unknown	2015	⁷¹
6	H _{1.68} MoO ₃ with PDMS	2D	95	1.37	84.8	Unknown	2020	⁷²
7	MXene-PVDF	2D	~90	~0.8	84	Unknown	2017	⁷³
8	PVA-Ti ₂ O ₃ hydrogels	3D		4.0	93	1100	2020	⁶⁴
9	Light absorbing sponge-like hydrogel	3D		3.6	90	1553 (DSC)		
						924 (equivalent enthalpy)	2019	⁶²
10	Ti ₃ C ₂ T _x MXene/rGO hydrogel	3D	95	3.62	91	(equivalent enthalpy) 905	2021	⁷⁴

11	Biomass-derived hybrid hydrogel	3D	3.2	90	1015	2020	⁶⁰
12	PVA-PPy hierarchically nanostructured gel	3D	3.2	94	1702	2018	42
13	PVA-PPy gel micro tree	3D	3.64			2021	⁷⁵
14	Interpenetrating polymer networks	3D	3.9	92	860	2020	⁶¹
15	PVA-rGO hydrogel	3D	2.5	95	Unknown	2018	⁷⁶
16	Vertically aligned graphene sheets membrane	3D	93% UV 98% Vis 100% NIR	1.62	86	2017	⁷⁷
17	Anti-bacterial hydrogels	3D	3.4	91	952	2021	⁷⁸
18	PPy (origamis)	3D	2.12	91.5	Unknown	2019	⁷⁹
19	PVA-PVDF membrane (cone)	3D	99.2	1.70	93.8	Unknown	2018
20	ITO-MS-PPy	3D	1.12	70.3	Unknown	2020	⁸¹
21	PAN@CuS fabrics	3D	91.1	2.27	83.9	1956.32 (TG)	2021
							⁶⁶

References

- [1] Rodríguez-Carvajal, J. Recent advances in magnetic structure determination by neutron powder diffraction. *Physica B: Condensed Matter* **192**, 55-69, doi:doi.org/10.1016/0921-4526(93)90108-I (1993).
- [2] Tokoro, H. *et al.* External stimulation-controllable heat-storage ceramics. *Nat. Commun.* **6**, 7037, doi:10.1038/ncomms8037 (2015).
- [3] Hodeau, J. L. & Marezio, M. Structural aspects of the metal-insulator transitions in $(\text{Ti}_{0.9975}\text{V}_{0.0025})_4\text{O}_7$. *J. Solid State Chem.* **29**, 47-62, doi:10.1016/0022-4596(79)90208-1 (1979).
- [4] Perdew, J. P. *et al.* Restoring the density-gradient expansion for exchange in solids and surfaces. *Phys. Rev. Lett.* **100**, 136406, doi:10.1103/PhysRevLett.100.136406 (2008).
- [5] Dudarev, S. L. *et al.* Electron-energy-loss spectra and the structural stability of nickel oxide: an LSDA+U study. *Phys. Rev. B* **57**, 1505-1509, doi:10.1103/PhysRevB.57.1505 (1998).
- [6] Wang, J. *et al.* High-performance photothermal conversion of narrow-bandgap Ti_2O_3 nanoparticles. *Adv. Mater.* **29**, 201603730, doi:10.1002/adma.201603730 (2017).
- [7] Ohkoshi, S. *et al.* Synthesis of a metal oxide with a room-temperature photoreversible phase transition. *Nat. Chem.* **2**, 539-545, doi:10.1038/nchem.670 (2010).
- [8] Wooten, F. *Optical properties of solids*. Academic Press, (1972).
- [9] Liu, P. *et al.* Relativistic GW+BSE study of the optical properties of Ruddlesden-Popper iridates. *Phys. Rev. Mater.* **2**, 075003, doi:10.1103/PhysRevMaterials.2.075003 (2018).
- [10] Ambrosch-Draxl, C. & Sofo, J. O. Linear optical properties of solids within the full-potential linearized augmented planewave method. *Comput. Phys. Commun.* **175**, 1-14, doi:10.1016/j.cpc.2006.03.005 (2006).
- [11] Kim, B., Kim, B. H., Kim, K. & Min, B. I. Substrate-tuning of correlated spin-orbit oxides revealed by optical conductivity calculations. *Sci. Rep.* **6**, 27095, doi:10.1038/srep27095 (2016).
- [12] Humbert, M. & Bunge, H. J. Advances and application of quantitative texture analysis, (eds H.J. Bunge & C. Esling) DGM Informationsgesellschaft mbHs, (1991).
- [13] Hashin, Z. & Shtrikman, S. Conductivity of polycrystals. *Phys. Rev.* **130**, 129-133, doi:10.1103/PhysRev.130.129 (1963).
- [14] Petousis, I. *et al.* High-throughput screening of inorganic compounds for the discovery of novel dielectric and optical materials. *Sci. Data* **4**, 160134, doi:10.1038/sdata.2016.134 (2017).
- [15] <https://vaspkit.com/tutorials.html#optic-properties>.
- [16] Li, X. Q. *et al.* Enhancement of interfacial solar vapor generation by environmental energy. *Joule* **2**, 1331-1338, doi:10.1016/j.joule.2018.04.004 (2018).
- [17] Shi, Y. *et al.* A 3D photothermal structure toward improved energy efficiency in solar steam generation. *Joule* **2**, 1171-1186, doi:10.1016/j.joule.2018.03.013 (2018).
- [18] Gao, M. M., Zhu, L. L., Peh, C. K. & Ho, G. W. Solar absorber material and system designs for photothermal water vaporization towards clean water and energy production. *Energy Environ. Sci.* **12**, 841-864, doi:10.1039/c8ee01146j (2019).
- [19] Lu, S. S. M., Pollak, F. H. & Raccah, P. M. Polarization-dependent reflectivity and optical constants of Ti_2O_3 in the range 0.7-10 eV. *Phys. Rev. B* **17**, 1970-1975, doi:10.1103/PhysRevB.17.1970 (1978).
- [20] Li, Y. *et al.* Orthorhombic Ti_2O_3 : a polymorph-dependent narrow-bandgap ferromagnetic oxide. *Adv. Funct. Mater.* **28**, 1705657, doi:10.1002/adfm.201705657 (2018).

- [21] Mariette, C. *et al.* Strain wave pathway to semiconductor-to-metal transition revealed by time-resolved X-ray powder diffraction. *Nat. Commun.* **12**, 1239, doi:10.1038/s41467-021-21316-y (2021).
- [22] Hosseinpour, S. *et al.* Chemisorbed and physisorbed water at the TiO₂/water interface. *J Phys Chem Lett* **8**, 2195-2199, doi:10.1021/acs.jpclett.7b00564 (2017).
- [23] Liu, X. *et al.* Towards highly efficient solar-driven interfacial evaporation for desalination. *J. Mater. Chem. A* **8**, 17907-17937, doi:10.1039/c9ta12612k (2020).
- [24] Ni, G. *et al.* Steam generation under one sun enabled by a floating structure with thermal concentration. *Nat. Energy* **1**, 16126, doi:10.1038/nenergy.2016.126 (2016).
- [25] Boller, A., Jin, Y. & Wunderlich, B. Heat capacity measurement by modulated DSC at constant temperature. *Journal of thermal analysis* **42**, 307-330, doi:10.1007/BF02548519 (1994).
- [26] Rumpf, D. I. B. Thermochemical data of pure substances. *Veterinary Immunology and Immunopathology* **55**, 359-360, doi:10.1016/S0165-2427(96)05632-2 (1997).
- [27] Abazović, N. D. *et al.* Photoluminescence of anatase and rutile TiO₂ particles. *The Journal of Physical Chemistry B* **110**, 25366-25370, doi:10.1021/jp064454f (2006).
- [28] Chen, H. *et al.* Non-metallic electrical transport properties of a metastable lambda-Ti₃O₅ thin film epitaxially stabilized on a pseudobrookite seed layer. *Appl. Phys. Lett.* **116**, 201904, doi:10.1063/5.0008888 (2020).
- [29] Ashcroft, N. W. & Mermin, N. D. *Solid state physics*. Vol. 9, 1976).
- [30] Bazbouz, M. B. *et al.* Fabrication of high specific electrical conductivity and high ampacity carbon nanotube/copper composite wires. *Advanced Electronic Materials* **7**, 2001213, doi:doi.org/10.1002/aelm.202001213 (2021).
- [31] Pontius, N. *et al.* Ultrafast relaxation dynamics of optically excited electrons in Ni₃. *Phys. Rev. B* **67**, 035425, doi:10.1103/PhysRevB.67.035425 (2003).
- [32] Bauer, M., Marienfeld, A. & Aeschlimann, M. Hot electron lifetimes in metals probed by time-resolved two-photon photoemission. *Prog. Surf. Sci.* **90**, 319-376, doi:doi.org/10.1016/j.progsurf.2015.05.001 (2015).
- [33] Bauer, M. & Aeschlimann, M. Dynamics of excited electrons in metals, thin films and nanostructures. *J. Electron Spectrosc. Relat. Phenom.* **124**, 225-243, doi:doi.org/10.1016/S0368-2048(02)00056-7 (2002).
- [34] Ladstädter, F., Hohenester, U., Puschnig, P. & Ambrosch-Draxl, C. First-principles calculation of hot-electron scattering in metals. *Phys. Rev. B* **70**, 235125, doi:10.1103/PhysRevB.70.235125 (2004).
- [35] Wilson, R. B. & Coh, S. Parametric dependence of hot electron relaxation timescales on electron-electron and electron-phonon interaction strengths. *Communications Physics* **3**, 179, doi:10.1038/s42005-020-00442-x (2020).
- [36] Zhukov, V. P. & Chulkov, E. V. The femtosecond dynamics of electrons in metals. *Phys. Usp.* **52**, 105-136, doi:10.3367/UFNe.0179.200902a.0113 (2009).
- [37] Campillo, I. *et al.* Inelastic lifetimes of hot electrons in real metals. *Phys. Rev. Lett.* **83**, 2230-2233, doi:10.1103/PhysRevLett.83.2230 (1999).
- [38] Aeschlimann, M., Bauer, M. & Pawlik, S. Competing nonradiative channels for hot electron induced surface photochemistry. *Chem. Phys.* **205**, 127-141, doi:doi.org/10.1016/0301-0104(95)00372-X (1996).

- [39] Li, X. Q. *et al.* Measuring conversion efficiency of solar vapor generation. *Joule* **3**, 1798-1803, doi:10.1016/j.joule.2019.06.009 (2019).
- [40] Yin, K. *et al.* Femtosecond laser induced robust Ti foam based evaporator for efficient solar desalination. *J. Mater. Chem. A* **7**, 8361-8367, doi:10.1039/c9ta00291j (2019).
- [41] Li, T. *et al.* Ultra-robust carbon fibers for multi-media purification via solar-evaporation. *J. Mater. Chem. A* **7**, 586-593, doi:10.1039/c8ta08829b (2019).
- [42] Zhao, F. *et al.* Highly efficient solar vapour generation via hierarchically nanostructured gels. *Nat. Nanotechnol.* **13**, 489-495, doi:10.1038/s41565-018-0097-z (2018).
- [43] Lu, Q., Shi, W., Yang, H. & Wang, X. Nanoconfined water-molecule channels for high-yield solar vapor generation under weaker sunlight. *Adv Mater* **32**, 2001544, doi:10.1002/adma.202001544 (2020).
- [44] Chen, X. *et al.* Highly efficient photothermal conversion and water transport during solar evaporation enabled by amorphous hollow multishelled nanocomposites. *Adv Mater* **34**, 2107400, doi:10.1002/adma.202107400 (2022).
- [45] Grimme, S., Antony, J., Ehrlich, S. & Krieg, H. A consistent and accurate ab initio parametrization of density functional dispersion correction (DFT-D) for the 94 elements H-Pu. *J. Chem. Phys.* **132**, 154104, doi:10.1063/1.3382344 (2010).
- [46] Henkelman, G., Arnaldsson, A. & Jónsson, H. A fast and robust algorithm for Bader decomposition of charge density. *Comput. Mater. Sci.* **36**, 354-360, doi:doi.org/10.1016/j.commatsci.2005.04.010 (2006).
- [47] Henkelman, G., Uberuaga, B. P. & Jónsson, H. A climbing image nudged elastic band method for finding saddle points and minimum energy paths. *J. Chem. Phys.* **113**, 9901-9904, doi:10.1063/1.1329672 (2000).
- [48] Jackson, P. & Parfitt, G. D. Infra-red study of the surface properties of rutile. water and surface hydroxyl species. *Transactions of the Faraday Society* **67**, 2469-2483, doi:10.1039/TF9716702469 (1971).
- [49] Belhadj, H., Hakki, A., Robertson, P. K. & Bahnemann, D. W. In situ ATR-FTIR study of H₂O and D₂O adsorption on TiO₂ under UV irradiation. *Phys Chem Chem Phys* **17**, 22940-22946, doi:10.1039/c5cp03947a (2015).
- [50] Peng, Y., Wu, P. & Yang, Y. Two-dimensional infrared correlation spectroscopy as a probe of sequential events in the diffusion process of water in poly(ϵ -caprolactone). *J. Chem. Phys.* **119**, 8075-8079, doi:10.1063/1.1610441 (2003).
- [51] Bezrodna, T. *et al.* IR-analysis of H-bonded H₂O on the pure TiO₂ surface. *Journal of Molecular Structure* **700**, 175-181, doi:10.1016/j.molstruc.2003.12.057 (2004).
- [52] Yang, Q. *et al.* Capillary condensation under atomic-scale confinement. *Nature* **588**, 250-253, doi:10.1038/s41586-020-2978-1 (2020).
- [53] Zhang, B. *et al.* Infrared spectroscopy of neutral water clusters at finite temperature: Evidence for a noncyclic pentamer. *Proc. Natl. Acad. Sci. U. S. A.* **117**, 15423-15428, doi:10.1073/pnas.2000601117 (2020).
- [54] Miyazaki, M., Fujii, A., Ebata, T. & Mikami, N. Infrared spectroscopic evidence for protonated water clusters forming nanoscale cages. *Science* **304**, 1134-1137, doi:10.1126/science.1096037 (2004).
- [55] Zwier, T. S. The structure of protonated water clusters. *Science* **304**, 1119-1120, doi:doi:10.1126/science.1098129 (2004).
- [56] Monosmith, W. B. & Walrafen, G. E. Temperature dependence of the Raman OH-stretching overtone from liquid water. *J. Chem. Phys.* **81**, 669-674, doi:10.1063/1.447748 (1984).

- [57] Rodgers, M. T. & Armentrout, P. B. Collision-induced dissociation measurements on $\text{Li}^+(\text{H}_2\text{O})_n$, $n = 1\text{--}6$: the first direct measurement of the $\text{Li}^+–\text{OH}_2$ bond energy. *The Journal of Physical Chemistry A* **101**, 1238-1249, doi:10.1021/jp962170x (1997).
- [58] Bacelo, D. E. & Ishikawa, Y. Theoretical study of microscopic solvation of LiCl in water clusters: $\text{LiCl}(\text{H}_2\text{O})_n$ ($n=1\text{--}4$). *Chemical Physics Letters* **319**, 679-686, doi:doi.org/10.1016/S0009-2614(00)00169-X (2000).
- [59] Li, X. & Yang, Z. Z. Study of lithium cation in water clusters: based on atom-bond electronegativity equalization method fused into molecular mechanics. *J Phys Chem A* **109**, 4102-4111, doi:10.1021/jp0458093 (2005).
- [60] Guo, Y. *et al.* Biomass-derived hybrid hydrogel evaporators for cost-effective solar water purification. *Adv. Mater.* **32**, 1907061, doi:10.1002/adma.201907061 (2020).
- [61] Zhou, X. Y. *et al.* Topology-controlled hydration of polymer network in hydrogels for solar-driven wastewater treatment. *Adv. Mater.* **32**, 202007012, doi:10.1002/adma.202007012 (2020).
- [62] Guo, Y. H. *et al.* Synergistic energy nanoconfinement and water activation in hydrogels for efficient solar water desalination. *ACS Nano* **13**, 7913-7919, doi:10.1021/acsnano.9b02301 (2019).
- [63] Chaule, S. *et al.* Rational design of a high performance and robust solar evaporator via 3D-printing technology. *Adv. Mater.* **33**, 2102649, doi:10.1002/adma.202102649 (2021).
- [64] Guo, Y. H. *et al.* Tailoring surface wetting states for ultrafast solar-driven water evaporation. *Energy Environ. Sci.* **13**, 2087-2095, doi:10.1039/d0ee00399a (2020).
- [65] Yu, Z. *et al.* Enhanced interfacial solar evaporation through formation of micro-meniscuses and microdroplets to reduce evaporation enthalpy. *Adv. Funct. Mater.* **32**, 2108586, doi:10.1002/adfm.202108586 (2022).
- [66] Liu, Z. *et al.* Hierarchical photothermal fabrics with low evaporation enthalpy as heliotropic evaporators for efficient, continuous, salt-free desalination. *ACS Nano* **8**, 13007-13018, doi:10.1021/acsnano.1c01900 (2021).
- [67] Guo, Y. H. *et al.* Tailoring nanoscale surface topography of hydrogel for efficient solar vapor generation. *Nano Lett.* **19**, 2530-2536, doi:10.1021/acs.nanolett.9b00252 (2019).
- [68] World Health Organization, Safe drinking-water from desalination, http://apps.who.int/iris/bitstream/10665/70621/1/WHO_HSE_WSH_11.03_eng.pdf (2011).
- [69] Ye, M. *et al.* Synthesis of black TiO_x nanoparticles by Mg reduction of TiO_2 nanocrystals and their application for solar water evaporation. *Adv. Energy Mater.* **7**, 1601811, doi:10.1002/aenm.201601811 (2017).
- [70] Zhou, L. *et al.* 3D self-assembly of aluminium nanoparticles for plasmon-enhanced solar desalination. *Nat. Photonics* **10**, 393-397, doi:10.1038/nphoton.2016.75 (2016).
- [71] Bae, K. *et al.* Flexible thin-film black gold membranes with ultrabroadband plasmonic nanofocusing for efficient solar vapour generation. *Nat. Commun.* **6**, 10103, doi:10.1038/ncomms10103 (2015).
- [72] Zhu, Q. *et al.* A hydrogenated metal oxide with full solar spectrum absorption for highly efficient photothermal water evaporation. *J. Phys. Chem. Lett.* **11**, 2502-2509, doi:10.1021/acs.jpclett.0c00592 (2020).
- [73] Li, R., Zhang, L., Shi, L. & Wang, P. MXene Ti_3C_2 : an effective 2D light-to-heat conversion material. *ACS Nano* **11**, 3752-3759, doi:10.1021/acsnano.6b08415 (2017).

- [74] Lu, Y. *et al.* Surface patterning of two-dimensional nanostructure-embedded photothermal hydrogels for high-yield solar steam generation. *ACS Nano* **15**, 10366-10376, doi:10.1021/acsnano.1c02578 (2021).
- [75] Shi, Y., Ilic, O., Atwater, H. A. & Greer, J. R. All-day fresh water harvesting by microstructured hydrogel membranes. *Nat. Commun.* **12**, 2797, doi:10.1038/s41467-021-23174-0 (2021).
- [76] Zhou, X. Y. *et al.* A hydrogel-based antifouling solar evaporator for highly efficient water desalination. *Energy Environ. Sci.* **11**, 1985-1992, doi:10.1039/c8ee00567b (2018).
- [77] Zhang, P. P. *et al.* Vertically aligned graphene sheets membrane for highly efficient solar thermal generation of clean water. *ACS Nano* **11**, 5087-5093, doi:10.1021/acsnano.7b01965 (2017).
- [78] Guo, Y. *et al.* Molecular engineering of hydrogels for rapid water disinfection and sustainable solar vapor generation. *Adv Mater* **33**, 2102994, doi:10.1002/adma.202102994 (2021).
- [79] Li, W., Li, Z., Bertelsmann, K. & Fan, D. E. Portable low-pressure solar steaming-collection unisystem with polypyrrole origamis. *Adv. Mater.* **31**, 1900720, doi:10.1002/adma.201900720 (2019).
- [80] Wang, Y. *et al.* Improved light-harvesting and thermal management for efficient solar-driven water evaporation using 3D photothermal cones. *J. Mater. Chem. A* **6**, 9874-9881, doi:10.1039/c8ta01469h (2018).
- [81] Qi, D. P. *et al.* Polymeric membranes with selective solution-diffusion for intercepting volatile organic compounds during solar-driven water remediation. *Adv. Mater.*, 202004401, doi:10.1002/adma.202004401 (2020).